TFAP2C and *HNRNPK* control mTOR cell metabolism and prion propagation

Stefano Sellitto[1], Davide Caredio[1], Matteo Bimbati[1], Giovanni Mariutti[1], Martina Cerisoli[1], Lukas Frick[1], Vangelis Bouris[1], Carlos Omar Oueslati Morales[1], Dalila Laura Vena[1], Sandesh Neupane[1], Federico Baroni[1], Kathi Ging[1], Jiang-An Yin[1], Elena De Cecco[1], Andrea Armani[1,2], and Adriano Aguzzi[*,1]

[1] Institute of Neuropathology, University of Zurich, Schmelzbergstrasse 12, CH-8091 Zurich, Switzerland.

[2] Department of Biomedical Sciences, University of Padova, Via Ugo Bassi 58/B - 35131 Padova, Italy.

[*] corresponding author: adriano.aguzzi@uzh.ch

Abstract

Heterogeneous Nuclear Ribonucleoprotein K (*HNRNPK*) is a limiting factor for prion propagation. However, little is known about its function except that it is essential to cell survival. Here, we performed a synthetic-viability CRISPR ablation screen to identify epistatic interactors of *HNRNPK*. We found that deletion of Transcription Factor AP-2γ (*TFAP2C*) mitigated the survival of hnRNP_K-depleted LN-229 and U-251 MG cells, whereas its overexpression hypersensitized cells to the loss of hnRNP_K. *HNRNPK* ablation induced downregulation of genes related to lipid and glucose metabolism, decreased cellular ATP, and enhanced catabolism through inhibition of the mTOR pathway and activation of AMPK. Conversely, *TFAP2C* deletion countered the energy crisis resulting from *HNRNPK* ablation, while its overexpression promoted mTOR anabolic activity. *TFAP2C* overexpression reduced prion propagation in wild-type cells and neutralized the enhanced prion replication of *HNRNPK*-suppressed cells. Importantly, mTOR inhibition mimicked the effects of *HNRNPK* silencing, increasing prion propagation. We conclude that *TFAP2C* and *HNRNPK* are genetic interactors controlling cell metabolism and bioenergy and influencing prion propagation potentially through modulation of the mTOR pathway.

Introduction

hnRNP_K is a highly conserved multifunctional protein expressed in nearly all mammalian tissues (*1-3*). hnRNP_K has been described as a DNA/RNA binding protein involved in several stages of RNA metabolism through mechanisms that are not fully understood (*4-11*). *HNRNPK* can act as an oncogene or tumor suppressor in numerous malignancies (*1, 12, 13*) and is linked to various neuronal functions (*14-16*). Its mutations and dysregulated expression are implicated in neurodevelopmental and neurodegenerative conditions such as Au-Kline syndrome (*17, 18*), Spinocerebellar Ataxia Type 10 (*19*), Amyotrophic Lateral Sclerosis, and Frontotemporal Lobar Degeneration (*20-25*). Moreover, we recently reported a role of hnRNP_K in limiting the misfolding of the cellular prion protein (PrP^{C}) into transmissible prions (PrP^{Sc}) (*26*), a process (referred to as prion propagation or replication) central to prion-induced neurodegeneration (*27, 28*).

The involvement of hnRNP_K in disparate proteinopathies suggests a broad role in protein folding and homeostasis. A better understanding of these functions may help elucidate shared mechanisms of genetic and molecular abnormalities among different neurodegenerative disorders. However, this is hampered by the essentiality of *HNRNPK,* whose genetic ablation is lethal to cells (*29-31*). Furthermore, *HNRNPK* expression is tightly regulated by negative feedback loop mechanisms. Thus, loss/gain-of-function studies are of limited usefulness to study *HNRNPK*'s functions, whereas unbiased "forward genetics" may be more promising.

Here, we performed a synthetic-survival CRISPR screen to discover epistatic interactors that might suppress the lethality of hnRNP_K loss-of-function and provide insights into its cellular roles. We found that the ablation of Transcription Factor AP-2γ (*TFAP2C*) mitigated the death of *HNRNPK*-ablated cells, whereas its overexpression sensitized cells to the loss of hnRNP_K. Also, we found that *HNRNPK* deletion reduced the transcription of genes related to fatty acid, sterol, and glucose metabolism, lowered intracellular ATP, and increased autophagic flux through mTOR downregulation and AMPK activation; all these functions were partially restored by *TFAP2C* co-deletion. Conversely, *TFAP2C* overexpression enhanced mTOR biosynthetic activity. We previously correlated energy metabolic shifts to *HNRNPK*-modulated prion propagation (*26*). Accordingly, *TFAP2C* overexpression reduced PrP^{Sc} propagation and limited its accumulation induced by the knockdown of *HNRNPK*. Importantly, mTOR inhibition reproduced the same effect as *HNRNPK* silencing on prion propagation. Hence, *TFAP2C* and *HNRNPK* are genetic interactors involved in the regulation of cell stress and metabolic homeostasis with a role in prion propagation.

Results

A cellular model to study HNRNPK essentiality

Our objective was to identify genes whose loss alleviates or exacerbates the impaired cellular fitness caused by the depletion of hnRNP_K. As model systems, we chose the human glioblastoma-derived LN-229 and U-251 MG cell lines, which express high levels of *HNRNPK* (*2, 3*). We generated polyclonal LN-229 and U-251 MG sublines stably expressing Cas9 and employed a plasmid harboring quadruple non-overlapping single-guide RNAs (qgRNAs), driven by four distinct constitutive promoters, to target the human *HNRNPK* gene (*32*). Seven days after qgRNA lentiviral delivery, we observed a substantial reduction in hnRNP_K protein followed, as expected, by a drop in cell viability (Fig. 1A-D). A minor fraction of LN-229 cells exhibiting low or no Cas9 expression did not undergo *HNRNPK* ablation, resulting in incomplete cell death (Fig. 1A, 1D). To address this issue, we isolated by limiting dilutions single LN-229 clones expressing high Cas9 levels (Supp. Fig. 1A). We compared Cas9 activity in 7 different clones using an *eGFP* reporter and selected LN-229 clone C3 (Supp. Fig. 1B). When we tested the *HNRNPK* ablation efficiency in LN-229 C3 cells, we observed complete protein depletion and cell death (Fig. 1A-B). Interestingly, U-251 MG Cas9 cells showed delayed cell death compared to LN-229 C3 (Fig. 1A).

To confirm that the observed lethality resulted from the absence of hnRNP_K, we transduced LN-229 C3 cells with constructs encoding the *HNRNPK* coding sequence under transcriptional control of the elongation factor 1α (EF-1α) promoter. We then utilized intron-targeting singe-guide RNAs (sgRNAs) to selectively ablate the endogenous *HNRNPK* gene (Supp. Table 1). The cell death resulting from *HNRNPK* deletion was suppressed by the exogenous constructs, confirming the specificity of the lethal phenotype and the reliability of this cellular model (Supp. Fig. 1C-D).

Genome-wide CRISPR ablation screen for the identification of HNRNPK epistatic interactors

To identify functionally relevant epistatic interactors of *HNRNPK*, we conducted a whole-genome ablation screen in LN-229 C3 cells using the Human CRISPR Brunello pooled library (*33*) , which targets 19,114 genes with an average of four distinct sgRNAs per gene (total = 76,441 sgRNAs). The lentiviral transduction of the Brunello library was followed by six days of antibiotic selection and subsequent lentiviral delivery of qgRNA vectors containing either *HNRNPK*-specific or non-targeting (NT) qgRNA guides. Cells underwent antibiotic selection for six more days before harvesting and gDNA extraction (Fig. 1E, Supp. Fig. 2A). sgRNAs distribution was analyzed by next-generation Illumina sequencing (NGS) at the onset of the screen after the library transduction (Day 1) and its endpoint (Day 14; Supp. Fig. 2A).

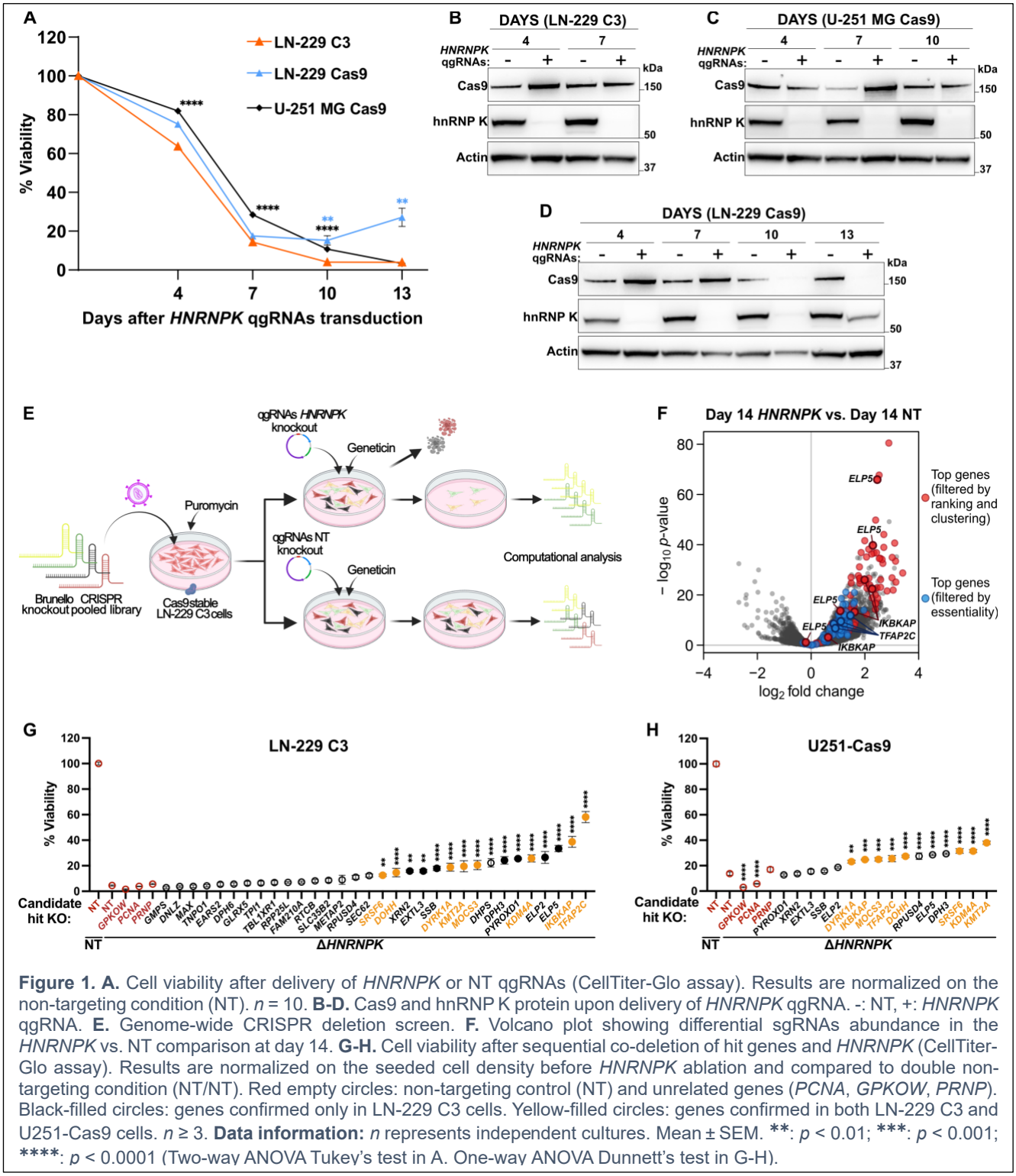

Figure 1. A. Cell viability after delivery of *HNRNPK* or NT qgRNAs (CellTiter-Glo assay). Results are normalized on the non-targeting condition (NT). *n* = 10. **B-D.** Cas9 and hnRNP K protein upon delivery of *HNRNPK* qgRNA. -: NT, +: *HNRNPK* qgRNA. **E.** Genome-wide CRISPR deletion screen. **F.** Volcano plot showing differential sgRNAs abundance in the *HNRNPK* vs. NT comparison at day 14. **G-H.** Cell viability after sequential co-deletion of hit genes and *HNRNPK* (CellTiter-Glo assay). Results are normalized on the seeded cell density before *HNRNPK* ablation and compared to double non-targeting condition (NT/NT). Red empty circles: non-targeting control (NT) and unrelated genes (*PCNA*, *GPKOW*, *PRNP*). Black-filled circles: genes confirmed only in LN-229 C3 cells. Yellow-filled circles: genes confirmed in both LN-229 C3 and U251-Cas9 cells. *n* ≥ 3. **Data information:** *n* represents independent cultures. Mean ± SEM. **: $p < 0.01$; ***: $p < 0.001$; ****: $p < 0.0001$ (Two-way ANOVA Tukey's test in A. One-way ANOVA Dunnett's test in G-H).

Two independent screens were conducted on different days and yielded a robust correlation indicative of satisfactory technical performance (Supp. Fig. 2B). When using the DepMap repository (*30, 31*) to compare the representation of essential genes in LN-229 cells at Day 14 NT vs. Day 1 (Supp. Table 2),

we found that 75% of the sgRNAs targeting known essential genes were efficiently depleted (log_2 fold change ≤ -1, FDR ≥ 0.01) with >92% of those essential genes having ≥2 sgRNAs dropped below threshold (Supp. Fig 2C-E).

We then listed genes whose sgRNAs were over- or underrepresented in the *HNRNPK* vs. NT at day 14, reasoning that their deletion would modify the lethality resulting from hnRNP_K removal. We obtained a list of 763 and 37 significantly enriched and depleted genes, respectively (log_2 fold change ≥1 or ≤ -1, FDR ≥0.01; Supp. Fig. 2F, Supp. Table 3). Pathway analysis of genes enriched with ≥2 sgRNAs yielded gene ontology (GO) terms related to ribosomal biogenesis, tRNA processing, non-coding RNA metabolism, and translation, consistent with the known roles of hnRNP_K in RNA metabolism (Supp. Fig. 2G). Accordingly, ablation of *HNRNPK* in LN-229 C3 cells showed a progressive reduction in global protein synthesis (Supp. Fig. 2H). Also, the GO analysis highlighted "tRNA wobble base modification" as the most overrepresented GO term (Supp. Fig. 2G). Genes encoding for Elongator complex proteins (ELPs), which are included in this pathway, were significantly enriched in the screen (Fig. 1F, Supp. Table 3), suggesting that their deletion counteracts the deleterious effects of *HNRNPK* ablation. Previous CRISPR screens showed that the absence of ELPs prevents apoptosis in metastatic gallbladder cancer (GBC) (*34*). Accordingly, our screen also showed enrichment of other general proapoptotic factors, including *AIFM1*, *MFN2,* and *FADD* (Supp. Table 3).

Among the most profoundly depleted genes were *PCBP1*, *PCBP2,* and *HNRNPA1*, all of which belong to the same genetic superfamily as *HNRNPK* (Supp. Table 3) *(35, 36)*. The synthetic lethality deriving from their co-deletion suggests that these genes cooperate with hnRNP_K in cell-essential processes. Conversely, the screen was enriched for sgRNA targeting *CPSF6*, *NUDT21*, and *XRN2*, which form protein complexes with hnRNP_K and regulate RNA maturation processes (Supp. Table 3) (*7, 37*). Hence, our screen identified *HNRNPK* functional partners sensitively and specifically despite the detection of additional, less specific cell death modulators.

TFAP2C ablation *suppresses HNRNPK loss-of-function*

To prioritize biologically relevant hits among the 763 enriched genes, we focused on those showing enrichment of all four sgRNAs (Supp. Table 3). We applied the STRING database (*38*) to assess protein-protein interactions and biological pathways associated with these genes. Next, we examined whether any other genes enriched in the screen scored as interactors. This allowed us to identify and select hierarchical functional clusters among our hits (Supp. Table 4). In parallel, we ranked the 763 enriched genes by multiplying their False Discovery Rate ($-log_{10}$ FDR) with their effect size (log_2 fold change; Supp. Table 4). We focused on genes with ≥2 sgRNA scoring in the top 100 rankings, with ≥1 sgRNA among the top 35. The intersection of this ordered list with the STRING clusters yielded 19 genes (Fig. 1F, Supp. Table 4). We generated a second list including those genes that, independently from the

ranking and clustering, had ≥2 sgRNAs enriched and scored as non-essential in the Day 14 NT vs. Day 1 comparison (maximally one sgRNA with $\log_2$ fold change ≤ -1, FDR ≥ 0.01; Fig. 1F, Supp. Table 4). Based on these two lists, 32 genes were selected for validation in LN-229 C3 cells. We ablated each gene individually and then deleted *HNRNPK*. Two different non-targeting qgRNAs were used as controls for *HNRNPK* and *TFAP2C* ablation.

We excluded genes whose deletion from *HNRNPK*$^{+/+}$ cells resulted in >50% enhanced or impaired cell viability (Supp. Fig. 2I-J). 16 of the initial 32 hits increased cell viability by >2-fold ($p < 0.01$) (Fig. 1G). We then tested these 16 genes also in U-251 MG Cas9 cells (henceforth abbreviated as U251-Cas9 cells) at a $\log_2$ fold threshold of ≥ 0.5. We confirmed a total of 9 hits (Fig. 1H), including the ELPs gene *IKBAKP* and the transcription factor *TFAP2C*, the two strongest hits identified in LN-229 C3 cells.

TFAP2C (Transcription Factor AP-2γ) was particularly interesting because it regulates the expression of several long non-coding RNAs (lncRNAs) (*39-41*) and has critical roles in neurodevelopmental

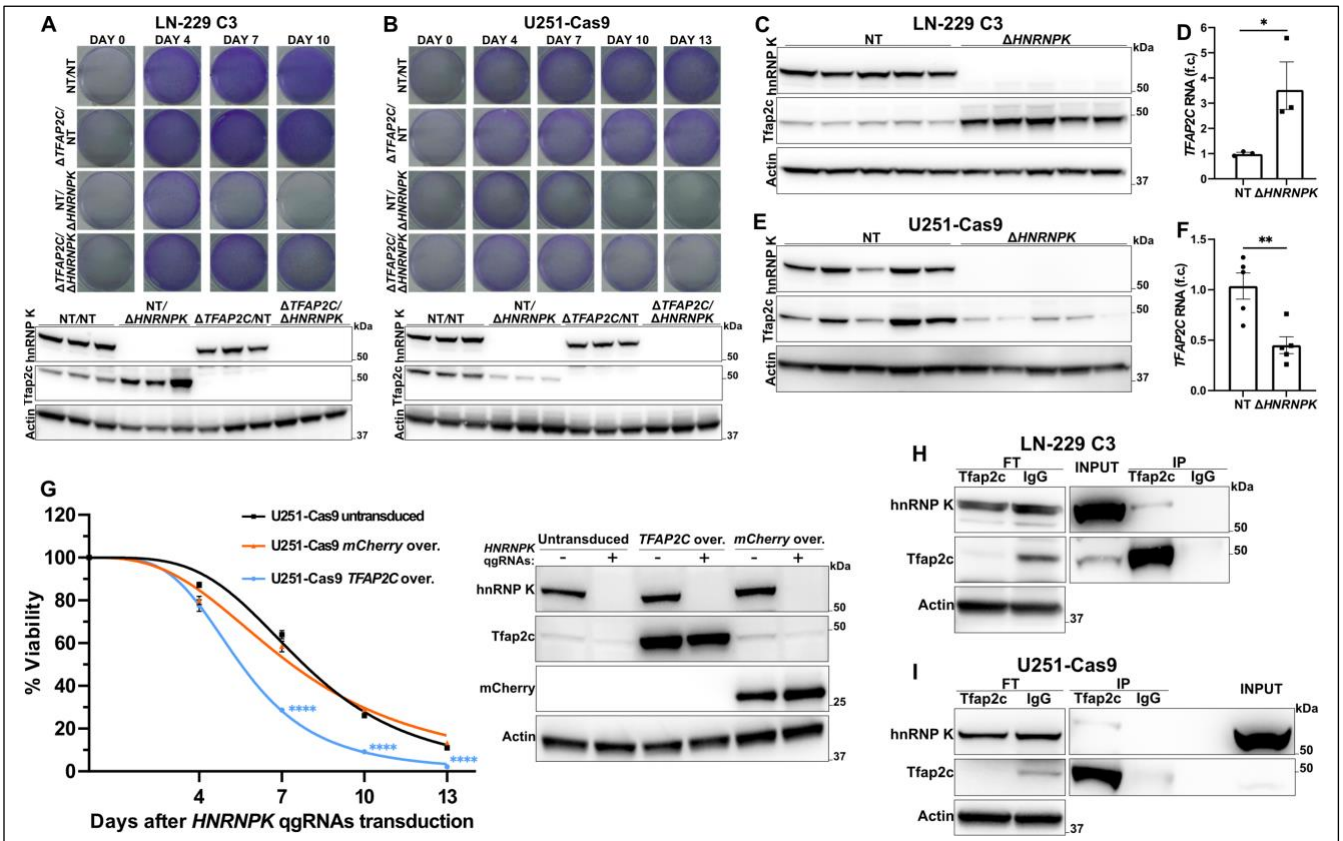

Figure 2. A-B. Clonogenic fitness of Δ*TFAP2C* and NT-transduced cells after delivery of *HNRNPK* or NT qgRNAs (Crystal violet staining). Western blot: hnRNP K and Tfap2c protein 7 (A) and 10 (B) days after qgRNAs delivery. $n = 3$. **C, E.** Tfap2c protein after *HNRNPK* ablation. $n = 5$. **D, F.** qRT-PCR showing *TFAP2C* RNA in LN-229 C3 (D) and U251-Cas9 (F) cells upon *HNRNPK* deletion. $n = 3$ and 5. **G.** Viability course of U251-Cas9 untransduced or overexpressing mCherry or *TFAP2C* after delivery of *HNRNPK* (+) or NT (-) qgRNAs (CellTiter-Glo assay). Results are normalized on the non-targeting condition (NT). $n = 10$. Western blot: hnRNP K, Tfap2c, and mCherry protein 10 days after qgRNAs delivery. **H-I.** Co-immunoprecipitation of Tfap2c and hnRNP K. IP: Immunoprecipitated Protein; FT: Flow-through after immunoprecipitation.
Data information: *n* represents independent cultures. f.c.: fold change. Mean ± SEM. *: $p < 0.05$, **: $p < 0.01$, ****: $p < 0.0001$ (Unpaired t-test in D and F. Two-way ANOVA Šídák's test in G).

processes (*42, 43*) similar to *HNRNPK* (*9, 17, 18, 37, 44, 45*). Moreover, both *HNRNPK* and *TFAP2C* have been described to modulate glucose metabolism (*46-48*). Therefore, we elected to explore the epistatic interaction between these two genes.

To consolidate the observations above, we repeated the experiments described in Fig. 2G-H by individually deleting only *TFAP2C* in 20 distinct technical replicas (Supp. Fig. 3A-B). As an orthogonal means of confirmation, we assessed the clonogenic potential of the respective ablated cells (Fig. 2A-B). Again, the deletion of *TFAP2C* suppressed the cell death induced by the removal of hnRNP_K in both LN-229 C3 and U251-Cas9 cells, whereas *TFAP2C* ablation alone only slightly reduced their growth rate. Thus, the loss of *TFAP2C* did not induce any intrinsic pro-survival effect, pointing to a specific epistatic interaction between *TFAP2C* and *HNRNPK*.

TFAP2C upregulation sensitizes cells to the loss of HNRNPK

Following *HNRNPK* ablation, we observed an increase in *TFAP2C* RNA and protein amount in LN-229 C3 cells (Fig. 2C-D). This suggested that the toxicity caused by hnRNP_K deletion may be due to *TFAP2C* upregulation. However, *TFAP2C* overexpression in LN-229-dCas9-VPR cells with unperturbed *HNRNPK* did not impair their viability (Supp. Fig. 3C). In U251-Cas9 cells, *HNRNPK* ablation had the opposite effect and decreased both the RNA and protein levels of *TFAP2C* (Fig. 2E-F), potentially explaining their relative resilience to *HNRNPK* ablation (Fig. 1A) and the smaller protective effect mediated by *TFAP2C* deletion in this cell line (Fig. 2A-B, Supp. Fig. 3A-B).

To test if *TFAP2C* overexpression sensitizes cells to the loss of *HNRNPK*, we produced stable U251-Cas9 lines overexpressing *TFAP2C* or mCherry for control and measured their viability after hnRNP_K removal. U251-Cas9 cells overexpressing *TFAP2C* experienced a significant acceleration of cell death ($p < 0.0001$; Fig. 2G), confirming the genetic relationship between *TFAP2C* and *HNRNPK* and highlighting a causative dependency between their expression levels and cell death.

Despite the changes in *TFAP2C* RNA upon ablation of *HNRNPK*, we were unable to overexpress *HNRNPK* in LN-229 and U-251 MG cells, possibly due to tight autoregulative feedback loops. However, neither the ablation nor the overexpression of *TFAP2C* modified the hnRNP_K levels in LN-229 and U-251 MG cells (Supp. Fig. 3D-I), disproving the existence of transcriptional feedback between *HNRNPK* and *TFAP2C*.

Nuclear colocalization and interaction between hnRNP_K and Tfap2c

We then asked whether hnRNP_K and Tfap2c proteins physically interact and modulate their reciprocal subcellular localization. Upon hnRNP_K and Tfap2c immunofluorescence staining in LN-229 C3 and U251-Cas9 cells, we noticed a nuclear overlap between the two proteins but no change in their

subcellular distribution after ablation of *TFAP2C* or *HNRNPK* (Supp. Fig. 3J-K). We also observed specific co-immunoprecipitation of hnRNP_K and Tfap2c in LN-229 C3 and U251-Cas9 cells (Fig. 2H-I, Supp. Fig. 3L), suggesting that the two proteins form a complex inside the nucleus.

HNRNPK and TFAP2C control the activation of caspase-dependent apoptosis but not ferroptosis

We then investigated whether the deletion of *HNRNPK* results in apoptosis. We detected increased levels of PARP and Caspase 3 cleavage in LN-229 C3 cells upon ablation of *HNRNPK* (Fig. 3A). Conversely, the prior removal of *TFAP2C* limited the cleavage of these two proteins (Fig. 3A), suggesting that *TFAP2C* ablation prevents apoptosis. PARP cleavage had the same pattern in U251-Cas9 cells; however, these cells did not show cleavage of Caspase 3 upon deletion of *HNRNPK*, *TFAP2C,* or both (Fig. 3B). We then asked whether the pan-caspase inhibitor Z-VAD-FMK reduced the lethality resulting from *HNRNPK* deletion. Z-VAD-FMK decreased cell death consistently and significantly in LN-229 C3 cells and U251-Cas9 cells transduced with *HNRNPK* ablation qgRNAs (Fig. 3C-D). These data confirm that *HNRNPK* deletion promotes cell apoptosis. We then treated LN-229 C3$^{\Delta TFAP2C}$ and U251-Cas9$^{\Delta TFAP2C}$ cells with increasing concentrations of staurosporine, a potent apoptosis inductor. Both cell lines were only mildly resistant to the apoptotic action of staurosporine (Fig. 3E-F). This suggests that *TFAP2C* ablation may exert its protective effect on *HNRNPK*-deleted cells by modulating a shared upstream process, eventually converging on apoptosis.

To investigate whether *HNRNPK* and *TFAP2C* ablation modulate additional cell death pathways, we explored their potential involvement in ferroptosis, a form of cell death marked by lipid peroxides accumulation. *TFAP2C* regulates ferroptosis by enhancing the expression of the Glutathione Peroxidase 4 (*GPX4*) upon selenium detection (*41, 49*). We inquired whether ferroptosis was activated upon ablation of *HNRNPK*. In LN-229 C3 and U251-Cas9 cells, the deletion of *HNRNPK* reduced the protein level of GPX4, whereas *TFAP2C* deletion increased it (Supp. Fig. 4A-B). Moreover, the ablation of *HNRNPK* led to higher lipid peroxidation in LN-229 C3 cells, which was increased in the absence of *TFAP2C* (Supp. Fig. 4C). To investigate this further, we challenged LN-229 C3$^{\Delta TFAP2C}$ and U251-Cas9$^{\Delta TFAP2C}$ cells with increasing doses of erastin, a commonly used ferroptosis inducer. *TFAP2C* ablation did not prevent erastin toxicity (Supp. Fig. 4D-E). Additionally, different anti-ferroptosis drugs did not suppress the lethality of hnRNP_K-depleted LN-229 C3 cells (Supp. Fig. 4F). These results suggest a role for *HNRNPK* and *TFAP2C* in balancing the protein levels of GPX4. However, ferroptosis seems only marginally connected to the essentiality of *HNRNPK* and is unlikely to be the primary toxic pathway activated by its removal.

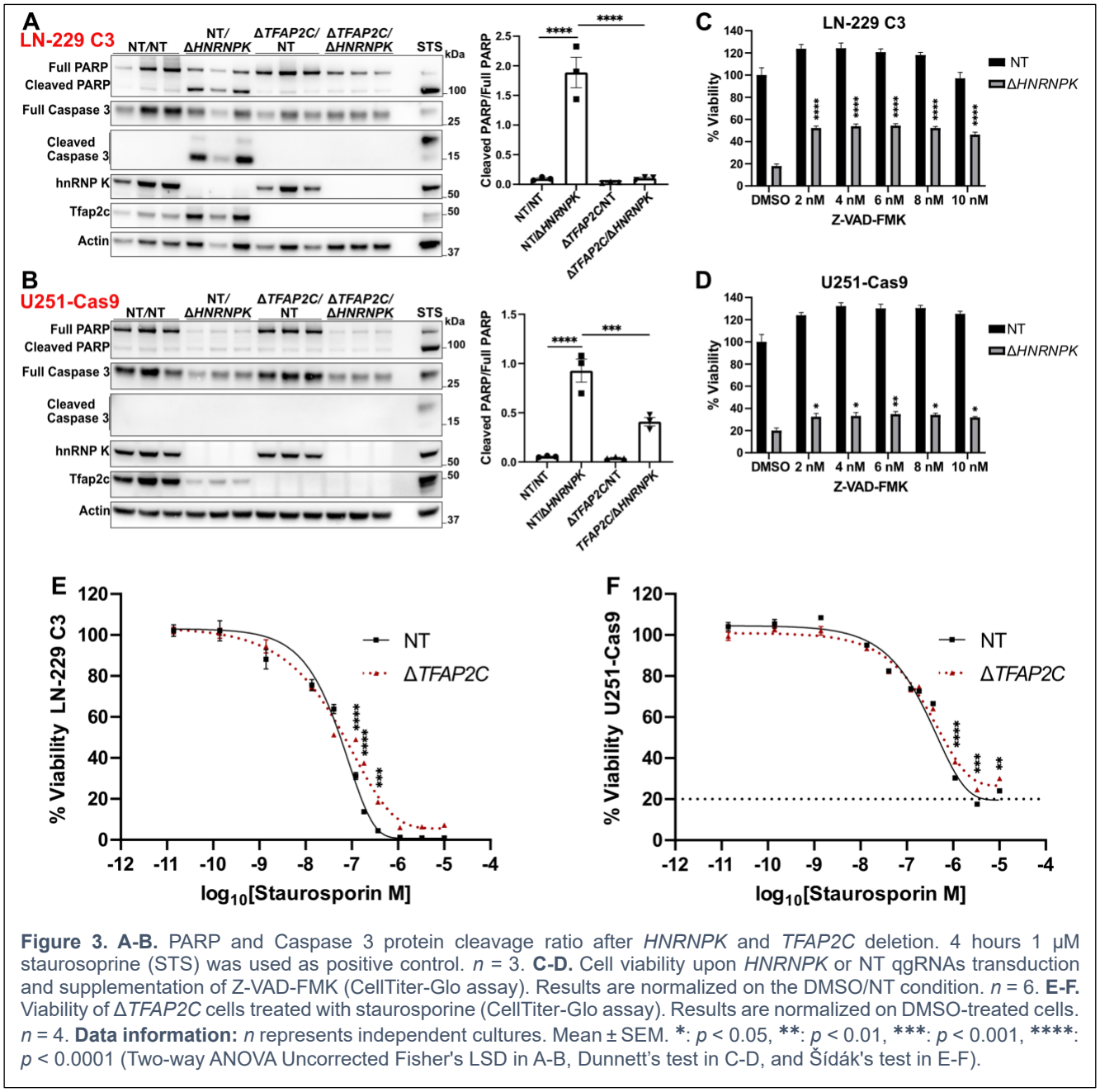

Figure 3. A-B. PARP and Caspase 3 protein cleavage ratio after *HNRNPK* and *TFAP2C* deletion. 4 hours 1 µM staurosoprine (STS) was used as positive control. *n* = 3. **C-D.** Cell viability upon *HNRNPK* or NT qgRNAs transduction and supplementation of Z-VAD-FMK (CellTiter-Glo assay). Results are normalized on the DMSO/NT condition. *n* = 6. **E-F.** Viability of Δ*TFAP2C* cells treated with staurosporine (CellTiter-Glo assay). Results are normalized on DMSO-treated cells. *n* = 4. **Data information:** *n* represents independent cultures. Mean ± SEM. *: $p < 0.05$, **: $p < 0.01$, ***: $p < 0.001$, ****: $p < 0.0001$ (Two-way ANOVA Uncorrected Fisher's LSD in A-B, Dunnett's test in C-D, and Šídák's test in E-F).

HNRNPK deletion perturbs the transcriptional regulation of genes involved in lipid and glucose metabolism

Apoptosis is often activated by upstream stress signals. To gain a mechanistic understanding of the early events shaping the observed genetic interaction, we sequenced total RNA in LN-229 C3 cells depleted of hnRNP_K, Tfap2c, or both (Supp. Table 5). We lysed cells four days after delivery of *HNRNPK* qgRNAs. At this time point, ablation was already extensive (Fig. 1B, Supp. Fig. 5A), yet cell viability was mostly preserved (Fig. 1A, 2A). Gene Set Enrichment Analysis (GSEA) showed significant

downregulation of genes involved in sterol biosynthesis, secondary alcohol metabolism, and fatty acids catabolism (FDR < 0.05) after removal of hnRNP_K (NT/Δ*HNRNPK* vs. NT/NT) (Fig. 4A). Conversely, the most upregulated genes in LN-229 C3$^{\Delta TFAP2C/\Delta HNRNPK}$ versus LN-229 C3$^{\Delta HNRNPK}$ cells (Δ*TFAP2C*/Δ*HNRNPK* vs. NT/Δ*HNRNPK*) pertained to lipid metabolism and lysosomal functions including sterol and secondary alcohol metabolic processes (Fig. 4B). The intersection of these upregulated genes (log_2 fold change ≥ 0.5) with genes downregulated upon depletion of hnRNP_K (log_2 fold change ≤ 0.5) yielded a significant enrichment of GO terms related to energy production and catabolic functions, including carbohydrate metabolism (Fig. 4C-D, Supp. Table 5). Factors involved in lipid metabolism and cholesterol biosynthesis like *FASN*, *SREBF1*, *LSS,* and *DHCR7*, and genes related to glycolysis and the pentose phosphate pathway, including *PGLS*, *G6PD*, *TPI1, H6PD,* and *GPI,* underwent consistent bidirectional regulation (Fig. 4C, Supp. Table 5). These data suggest that the transcriptional regulation of lipid and glucose metabolism is imbalanced by the removal of hnRNP_K and is partially restored by *TFAP2C* deletion.

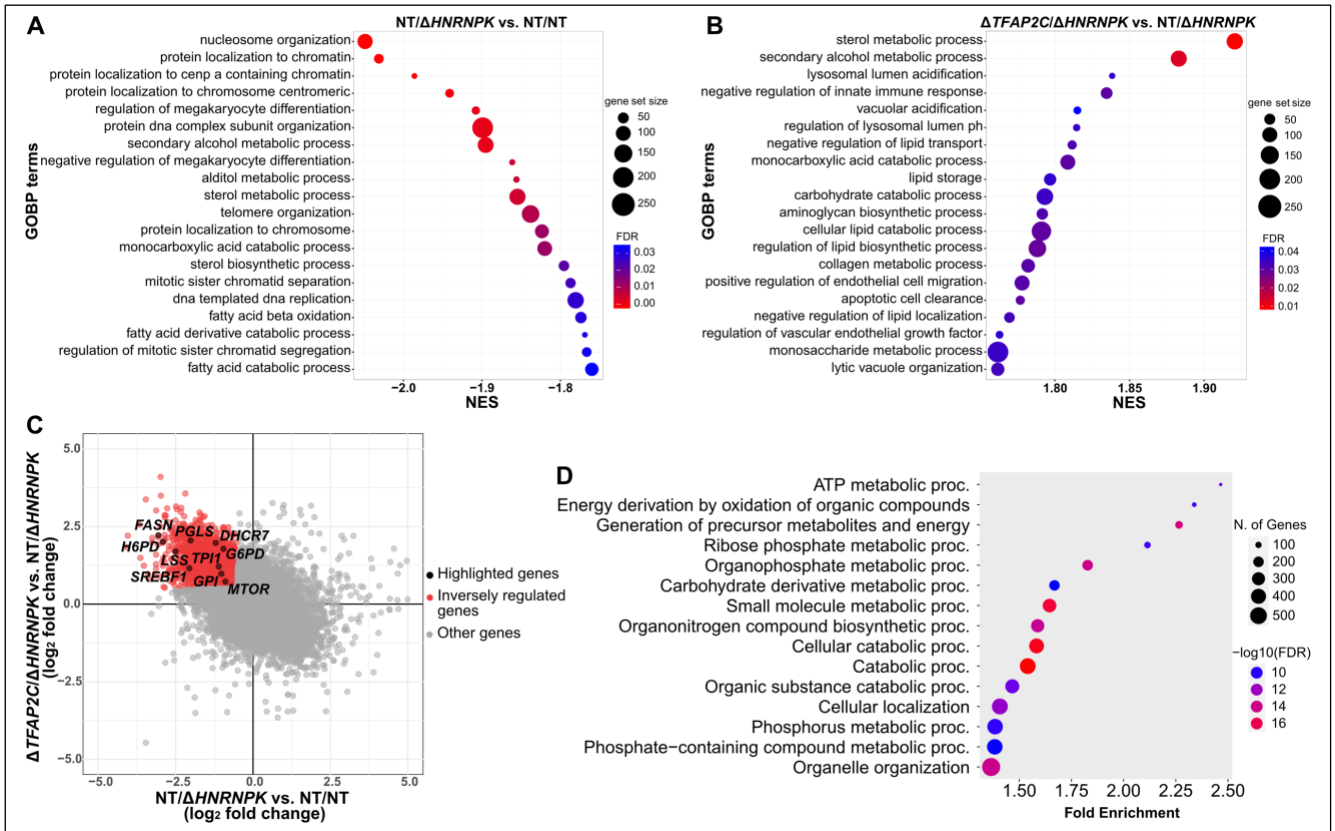

Figure 4. A-B. RNA-seq Gene Set Enrichment Analysis. Shown are the 20 most negatively (A) and positively (B) enriched GOBP terms (Gene Ontology Biological Process), respectively, in NT/Δ*HNRNPK* vs. NT/NT (A) and Δ*TFAP2C*/Δ*HNRNPK* vs. NT/Δ*HNRNPK* (B). NES: Normalized Enrichment Score. **C.** Intersection of RNA-seq data resulting from the Δ*TFAP2C*/Δ*HNRNPK* vs. NT/Δ*HNRNPK* and the NT/Δ*HNRNPK* vs. NT/NT comparisons. **D.** Gene enrichment of the biological process for the inversely regulated genes highlighted in C.

HNRNPK and TFAP2C bidirectionally regulate cell metabolism and bioenergetics via mTOR and AMPK

The deletion of *TFAP2C* and *HNRNPK* caused a broad transcriptional rewiring of cell bioenergetics and metabolism (Fig. 4A-D, Supp. Fig. 5A, Supp. Table 5). The mechanistic target of rapamycin (mTOR) and its associated protein Rptor were downregulated in LN-229 C3$^{\Delta HNRNPK}$ cells but were partially rebalanced by the Δ*TFAP2C*/Δ*HNRNPK* double deletion (Fig. 4C, Supp. Fig. 5B, Supp. Table 5). The phosphorylation of 4EBP1 and S6, two downstream targets of mTOR, followed the same trend (Fig. 5A). Deletion of *HNRNPK* diminished the highly phosphorylated forms of 4EBP1, whose pattern was conserved in both LN-229 C3$^{\Delta TFAP2C}$ and LN-229 C3$^{\Delta TFAP2C/\Delta HNRNPK}$ cells (Fig. 5A). Similarly, S6 phosphorylation ratio was reduced in LN-229 C3$^{\Delta HNRNPK}$ cells and was restored in the Δ*TFAP2C*/Δ*HNRNPK* double-ablated cells (Fig. 5A). Interestingly, total expression of 4EBP1 was reduced in both *HNRNPK* and *TFAP2C* single ablation and only partially rescued upon double deletion (Fig. 5A).

mTOR is a key regulator of cell anabolic and catabolic processes that senses and integrates upstream inputs related to cellular oxygen, nutrients, and energy levels (*50*). Accordingly, intracellular ATP was reduced four days after delivery of *HNRNPK* ablation qgRNAs. Conversely, ATP levels slightly increased after *TFAP2C* deletion and remained high when both genes were ablated (Fig. 5B). AMP-activated protein kinase (AMPK), a well-established ATP/AMP sensor, is phosphorylated and activated in the context of low cellular energy (*51*). Accordingly, we observed increased AMPK phosphorylation (pAMPK) upon ablation of *HNRNPK*, which was consistently reduced in LN-229 C3$^{\Delta TFAP2C}$ cells (Supp. Fig. 5C). LN-229 C3$^{\Delta TFAP2C/\Delta HNRNPK}$ cells also showed somewhat reduced pAMPK relative to LN-229 C3$^{\Delta HNRNPK}$ cells (Supp. Fig. 5C).

These results suggest that hnRNP_K depletion causes an energy shortfall, leading to cell death. We, therefore, measured autophagy after ablation of *HNRNPK* and *TFAP2C*. As previously reported (*52*), the LC3-II autophagy marker increased significantly ($p < 0.0001$) in LN-229 C3$^{\Delta HNRNPK}$ cells, suggestive of an energy crisis triggering autophagy, but less in LN-229 C3$^{\Delta TFAP2C/\Delta HNRNPK}$ cells (Fig. 5C, Supp. Fig. 5D). mTOR and AMPK control autophagy by regulating the phosphorylation of several downstream targets (*50, 51, 53*). Under nutrient sufficiency, mTOR phosphorylates Ulk1 at Ser758 (pUlk1), preventing its interaction with AMPK and inhibiting autophagosome formation (*53*). To test if the observed autophagy alterations are directly modulated by mTOR, we measured the phosphorylation of Ulk1. As anticipated, Ulk1 phosphorylation was reduced by *HNRNPK* ablation, homeostatically restored by concomitant Δ*TFAP2C*/Δ*HNRNPK* double ablation, and increased by single *TFAP2C* removal (Supp. Fig. 5E). We conclude that *HNRNPK* and *TFAP2C* play an essential role in co-regulating cell metabolism homeostasis influencing mTOR and AMPK activity and expression.

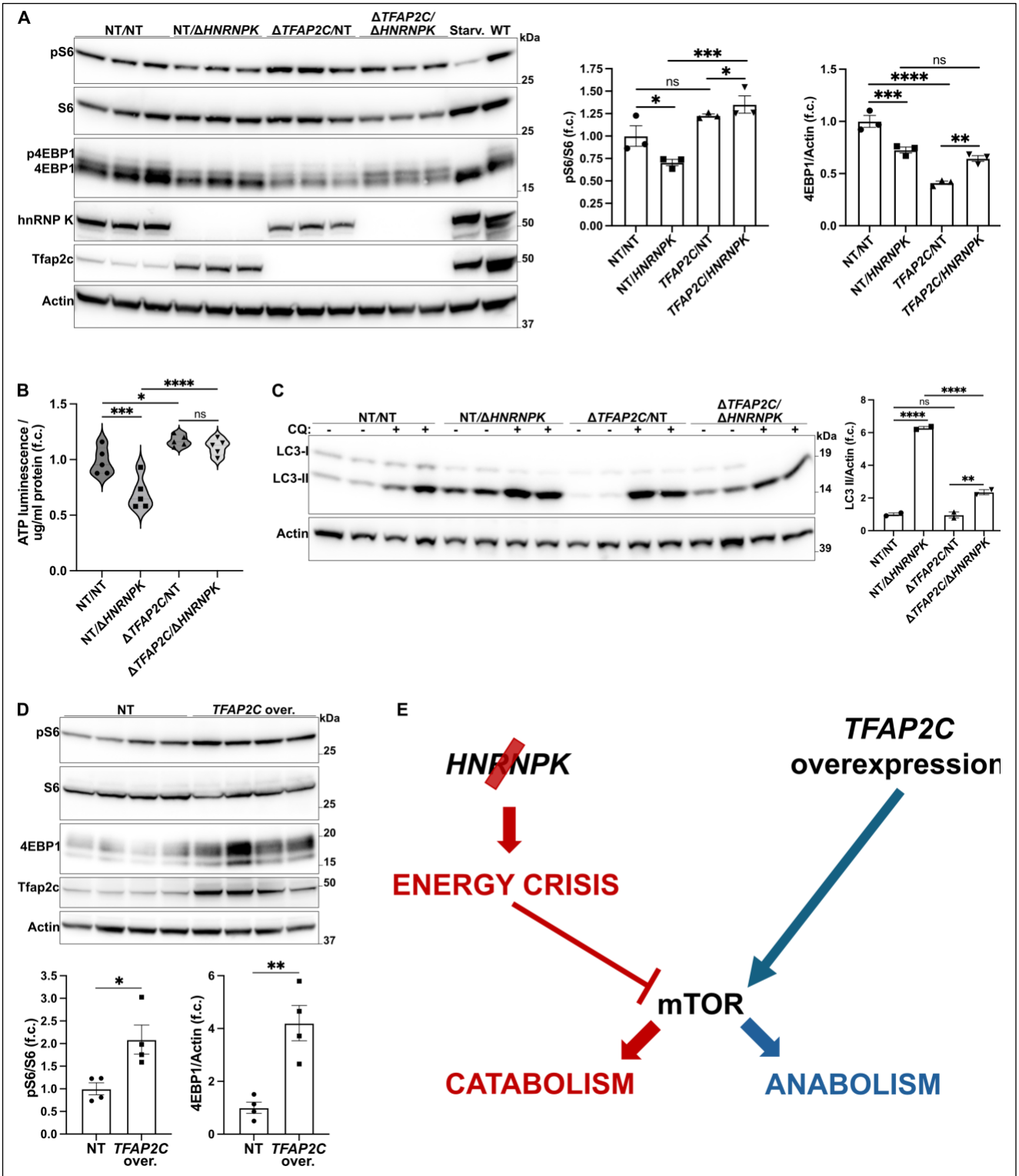

Figure 5. A. 4EBP1 and S6 protein phosphorylation after *HNRNPK* and *TFAP2C* deletion in LN-229 C3 cells. 6h HBSS-starvation (starv.) was used as positive control. *n* = 3. **B.** Intracellular ATP level in Δ*TFAP2C* and NT-transduced LN-229 C3 cells 4 days upon delivering *HNRNPK* and NT qgRNAs. *n* = 5. **C.** LC3-II protein in LN-229 C3 cells treated as in A. 4 hours 100 μM chloroquine (CQ) was used to monitor the autophagic flux. Basal autophagy (without chloroquine) is quantified. *n* = 2. Ablations are shown in Supp. Fig. 5D. **D.** 4EBP1 and S6 protein phosphorylation in LN-229 dCas9-VPR cells upon *TFAP2C* overexpression. *n* = 4. **E.** Hypothesized mechanism of *TFAP2C* and *HNRNPK* in cell metabolism regulation. **Data information:** *n* represents independent cultures. f.c.: fold change. Mean ± SEM. ns: $p > 0.05$, *: $p < 0.05$, **: $p < 0.01$, ***: $p < 0.001$, ****: $p < 0.0001$ (Two-way ANOVA Uncorrected Fisher's LSD in A-C. Unpaired t-test in D).

TFAP2C promotes mTOR anabolic cell functions

The above results suggest that *HNRNPK* ablation causes an energy crisis followed by inhibition of mTORC1 activity and a shift towards catabolism. *TFAP2C* deletion did not induce energetic impairment, yet it also affected the mTORC1 pathway by decreasing the expression of 4EBP1. To clarify these observations, we overexpressed *TFAP2C* in LN-229-dCas9-VPR cells. We found that both the phosphorylation ratio of S6 and expression levels of 4EBP1 increased upon *TFAP2C* upregulation (Fig. 5D), although we did not observe changes in mTOR protein expression (Supp. Fig. 5F). These data specify a role of *TFAP2C* in promoting mTOR-mediated cell anabolism and may explain why *HNRNPK* essentiality is mitigated by *TFAP2C* deletion and aggravated by its overexpression (Fig. 5E).

HNRNPK, TFAP2C and prion propagation

Transcriptional silencing of hnRNP_K results in increased misfolding of PrP^{C} into infectious prions (PrP^{Sc}) in a panel of cell lines (*26*), whereas psammaplysene A (PSA), a compound reported to interact with hnRNP_K (*54*), reduces prion levels. *HNRNPK* knockdown and PSA treatment induce an inversely symmetric transcriptional profile with downregulation and upregulation of genes related to glycolysis and energy metabolism (*26*). These results support the notion that cell stress and energy homeostasis may impact prion propagation and protein aggregation (*55-63*). We identified *HNRNPK* and *TFAP2C* playing interdependent roles in cell metabolism. Since *TFAP2C* upregulation activates mTOR, while *HNRNPK* ablation silence it (Fig. 5A-E, Supp. Fig. 5B-F), we wondered whether *TFAP2C* activation may affect prion propagation in a manner opposite to *HNRNPK* downregulation.

Because human prions are highly biohazardous and replicate poorly in most human cells, we used CRISPR/Cas9 to produce an LN-229$^{\Delta PRNP}$ subline devoid of human PrP^{C} (Supp. Fig. 6A-B). We then expressed a vector plasmid encoding the VRQ allele of the ovine prion protein to generate an isogenic ovinized line termed “HovL” (for “human ovinized LN-229”; Supp. Fig. 6A-B). As reported for other ovinized cell models (*64*), HovL cells were susceptible to infection by the PG127 strain of ovine prions and capable of sustaining chronic prion propagation (Supp. Fig. 6C-E).

We then overexpressed *TFAP2C* in PG127-infected and uninfected HovL cells using mCherry overexpression for control. Surprisingly, PrP^{Sc} immunostaining with the 6D11 antibody (*65*) and proteinase K (PK) digested immunoblots showed a consistent reduction of PrP^{Sc} (Fig. 6A-C) without significant changes in PrP^{C} (Supp. Fig. 7A), suggesting that *TFAP2C* modulates a post-translational step of the prion life cycle. *TFAP2C* upregulation also quenched the enhanced PrP^{Sc} accumulation caused by *HNRNPK* suppression (Fig. 6A-C). Importantly, these changes in PrP^{Sc} accumulation were associated with differences in the total prion load per cell, but not with the percentage of cells harboring

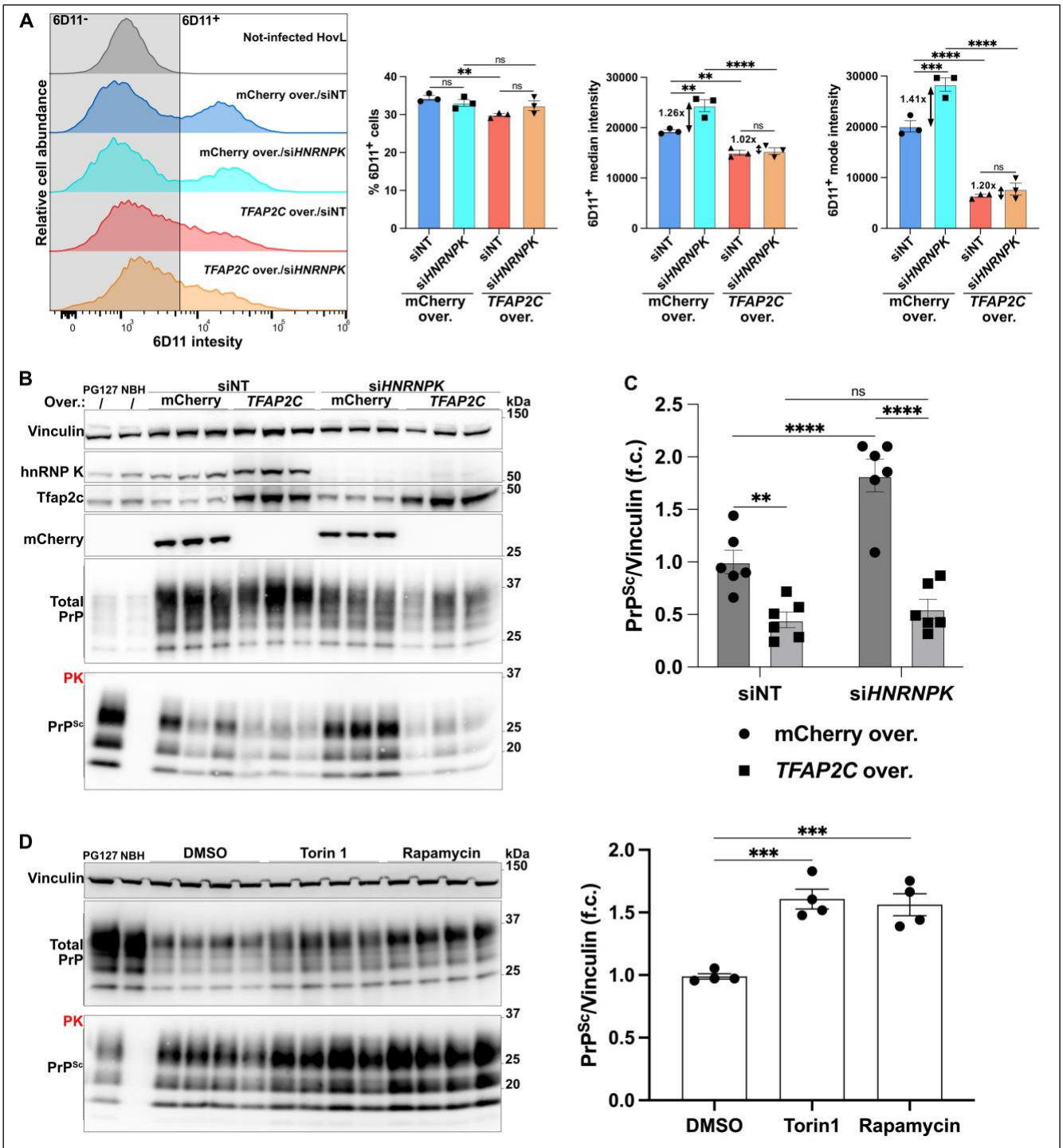

Figure 6. A. Flow cytometry quantification of anti-PrP^{Sc} 6D11 antibody signal in PG127-infected HovL cells upon *HNRNPK* knockdown and *TFP2C* or mCherry (control) overexpression. *n* = 3. **B, D.** Proteinase K (PK) digested (bottom) and undigested (top) western blots showing, respectively, PrP^{Sc} and total PrP in PG127-infected HovL cells treated as in A (B) or upon administration of 500 nM of torin1 and rapamycin (D). *n* = 3 and 4. **C.** Quantification of PrP^{Sc} protein from B and a second western blot membrane. *n* = 6. **Data information:** PG127-infected (PG127) and Not-infectious Brain Homogenate (NBH) were used for PK digestion positive and negative control, respectively. Non-targeting scrambled siRNA (siNT) was used as a control. *n* represents independent cultures. f.c.: fold change. Mean ± SEM. ns: $p > 0.05$, **: $p < 0.01$, ***: $p < 0.001$, ****: $p < 0.0001$ (Two-way ANOVA Uncorrected Fisher's LSD in A, C. One-way ANOVA Dunnett's test in D).

prions (Fig. 6A). This indicates that the observed alterations in PrP^{Sc} levels are not linked to differences in cell-to-cell prion spreading, but rather to changes in the biosynthesis of infectious prions.

To test if mTOR activity is involved in prion propagation, we treated HovL cells with torin 1 and rapamycin, two potent mTORC1/2 inhibitors. Three days of treatment resulted in a consistent increase of PrP^{Sc} levels similar to what observed upon *HNRNPK* silencing (Fig. 6D, Supp. Fig. 7B), suggesting that the effects of *HNRNPK* on prion replication may be mediated by mTOR.

Discussion

Because of its role as a prominent limiter of prion propagation (*26*), the molecular pathways in which hnRNP_K participates are of immediate interest to prion biology and, in the best case, may even point to therapeutically actionable targets against prion diseases. We reasoned that an important first step would consist of clarifying the molecular basis of the cell-essentiality of hnRNP_K. We opted to perform a CRISPR-based synthetic viability screen because this approach goes beyond the mere description of phenotypes associated with hnRNP_K deficiency, and can instead point to genes that are causally involved in mediating the function of hnRNP_K.

Large genome-wide perturbation screens assess the phenotypic outcomes of extensive collections of biological samples under various conditions. Consequently, background noise is frequently observed in these types of experiments, and our screen was no exception. We identified genes associated with mitochondrial membrane permeability and apoptosis, such as *FADD*, *MFN2*, *AIFM1*, and Elongator complex proteins (ELPs). These genes are likely to reflect non-specific outcomes since the deletion of proapoptotic factors results in enhanced survival upon cellular stress (*34, 66-71*). However, we also recovered genes directly linked to *HNRNPK*, such as *PCBP1*, *PCBP2,* and *HNRNPA1,* which are members of the *HNRNPK* gene superfamily *(35, 36)*. Furthermore, our screen enriched for *XRN2*, *NUDT21*, and *CPSF6*, which synergize with *HNRNPK* in modulating post-transcriptional RNA processes (*7, 37*). These results suggest that our experimental approach was effective in differentiating *HNRNPK* genetic interactors from background noise and genetic confounders.

The Transcription Factor AP-2γ (*TFAP2C*) emerged from our genetic screen as the strongest modulator of *HNRNPK* essentiality. Its effect was bidirectional: Tfap2c removal conspicuously reduced the cell death triggered by *HNRNPK* ablation, whereas its overexpression hypersensitized cells to the loss of *HNRNPK*. Both hnRNP_K and Tfap2c control the expression and localization of several lncRNAs (*9, 39, 45*), regulate different glucose metabolic pathways (*46-48*), and modulate neurodevelopment in mice and humans (*17, 18, 42, 43*). Because a direct functional interaction between these two genes had not been reported, we decided to investigate the molecular significance of their genetic link. We found that *HNRNPK* ablation perturbed the transcription of *TFAP2C*, although with opposite effects in different cell lines. Deletion or upregulation of *TFAP2C* did not change *HNRNPK* RNA and protein levels, disproving the presence of a regulatory feedback loop between these two genes and suggesting that hnRNP_K acts upstream of Tfap2c. In addition, we found that hnRNP_K and Tfap2c co-localize in the nucleus and co-immunoprecipitated from cellular extracts. Hence, multiple converging lines of evidence from forward genetics, immunostaining, and immunochemistry point to a functional connection between these two proteins.

The ablation of *TFAP2C* prevented the induction of caspase-dependent apoptosis triggered by the deletion of *HNRNPK*. However, this finding is not very informative because apoptosis can result from

multiple pathological processes, and its prevention does little to explain how Tfap2c mediates the action of hnRNP_K. To gain more insight into the relevant cellular events, we performed early-stage RNA sequencing analyses after ablation of *TFAP2C, HNRNPK*, or both. We found that hnRNP_K removal dysregulated cell bioenergetics, particularly impairing lipid and glucose metabolism, well before the initiation of cell death. Instead, Δ*TFAP2C*/Δ*HNRNPK* double-ablated cells retained a more balanced transcriptional profile. Accordingly, we observed that the ablation of *HNRNPK* reduced intracellular ATP levels and increased autophagy flux by decreasing mTOR expression and promoting AMPK activation. Crucially, all these perturbations were largely corrected by Δ*TFAP2C*/Δ*HNRNPK* double ablation. *TFAP2C* deletion alone also reduced the mTORC1 downstream activation by diminishing S6 phosphorylation and 4EBP1 expression, whereas *TFAP2C* overexpression increased both S6 phosphorylation and 4EBP1 levels. We conclude that *HNRNPK* deletion causes a metabolic impairment leading to a nutritional crisis and a catabolic shift, whereas *TFAP2C* activation promotes mTOR anabolic functions. Tfap2c removal may rewire the bioenergetic needs of cells, augmenting their resilience to metabolic stress like the ones induced by *HNRNPK* ablation.

These findings point to a previously unrecognized role of *HNRNPK*, i.e. its impact on cellular bioenergetics and metabolic regulation. Emerging evidence underscores the critical role of cellular energy homeostasis in protein misfolding disorders and neurodegeneration (*72-74*). Specifically, alterations in ATP levels and autophagy have been implicated in regulating the aggregation of pathogenic proteins (*58-63*). Thus, it is plausible that the metabolic imbalance resulting from *HNRNPK* ablation and linked to mTOR and AMPK dysregulation may influence prion propagation dynamics. Consistently, the anti-prion compound psammaplysene A (PSA) (*26*) is known to modulate the Foxo3a-mTOR-AMPK pathway (*75*), and PSA-treated cells upregulate genes related to glycolysis and energy metabolism, which are instead inhibited by *HNRNPK* knockdown (*26*).

Surprisingly, *TFAP2C* overexpression led to a marked reduction of aggregated pathogenic prions without altering the expression of their monomeric physiological precursor PrP^{C}. This points to a PrP^{C}-independent inhibitory effect of *TFAP2C* on prion propagation. Interestingly, *TFAP2C* upregulation prevented PrP^{Sc} accumulation even when *HNRNPK* was downregulated and despite a slight increase in PrP^{C} levels due to *HNRNPK* silencing. Hence, *TFAP2C* operates downstream or in parallel to *HNRNPK* in a pathway influencing prion propagation. Importantly, drug-mediated inhibition of mTOR also increased prion propagation.

These data suggest a role of *TFAP2C* and *HNRNPK* at the crossroads between cell metabolic control and prion propagation. One potential mechanism could involve the reciprocal regulation of autophagy and ATP production mediated by the mTOR pathway. Previous studies observed that mTOR inhibition and autophagy activation reduced, rather than increased, PrP^{Sc} aggregation (*76, 77*). However, most of these findings were based on long-term inhibition of mTOR. Acute inhibition, mimicking the time frame

of *HNRNPK* and *TFAP2C* manipulation, may produce distinct, short-lived metabolic changes that outweigh the effects of autophagy on prion propagation.

In conclusion, the identification of *TFAP2C* as a novel regulator linked to *HNRNPK* points to functions of this protein in the modulation of cell metabolism and outlines a possible explanation for its role in prion propagation. From a methodological viewpoint, the present study shows that it is possible to use synthetic-survival CRISPR screens to discover novel functional actions of genes even when their removal causes cell lethality. The fundaments laid here may be instrumental to discovering pathways regulated by *TFAP2C* and *HNRNPK* and their roles in the regulation of prion propagation and potentially additional proteinopathies.

Materials and methods

Cell culture

The LN-229 cell lines were cultured in Dulbecco's Modified Eagle Medium (DMEM) (Gibco, 11965092) supplemented with 10% fetal bovine serum (FBS) (Clontech Laboratories) and 1% penicillin/streptomycin (P/S) (Gibco, 15140122). The U-251MG cell lines were grown in OptiMEM (Gibco, 31985047) supplemented with 10% FBS, 1% GlutaMax (Gibco, 35050061), 1% MEM Non-Essential Amino acids (MEM-NEAA) (Gibco, 11140050), and 1% P/S. The HEK-293T cell line for lentivirus production was cultured in DMEM supplemented with 10% FBS. For lentiviral delivery, all cells were seeded in antibiotic-free medium and placed under antibiotic selection 24 hours after the transduction. All cells were maintained in culture at 37 °C in a 3% oxygen and 5% CO2 atmosphere.

HovL cell line generation

The generation of the human ovinized LN-229 cell line, HovL, was performed as previously described for the ovinized SHSY-5Y cell line, HovS (*64*). LN-229 wild-type cells were co-transfected with two plasmids encoding Cas9 (pSpCas9(BB)-2A-GFP, addgene #48138) and qgRNAs against human *PRNP* (*32*) to achieve *PRNP* ablation. A monoclonal line was isolated via limiting dilution, and the ablation was confirmed by PCR and sequencing. Δ*PRNP* cells were then transfected using Lipofectamine 3000 (Invitrogen) with an expression vector (EF1α promoter) (Sigma-Aldrich, OGS606-5U) containing the *Ovis aries PRNP* VRQ allele coding sequence (Genescript). The insert was cloned with the human ER localization signal and optimized for codon usage in human cells. Cells were kept under geneticin selection (400 µg/ml) (Thermo Fisher Scientific), and a stable monoclonal line was isolated via limiting dilution. Chronic PG127 prion-infected or mock-infected HovL were obtained as previously reported (*64*). HovL were incubated either with PG127 prion-contaminated Brain Homogenate (PG127) or Non-infectious Brain Homogenate (NBH) and split for at least eight passages to dilute to original prion inoculum and enhance *de novo* PrP^{Sc} formation and propagation. PG127 and NBH HovL were also transduced with lentiCas9-Blast plasmid to stably express Cas9 (*78*). Primers' sequences for PCR (Fwd: 5'-GCACTCATTCATTATGCAGGAAACA-3', Rev: 5'-AGACACCACCACTAAAAGGGC-3') and sequencing (5'-GGACTCTGACGTTCTCCTCTTC-3').

Immunoblotting

Cell extracts were prepared in lysis buffer (50 mM Tris–HCl, pH 8, 150 mM NaCl, 0.5% sodium deoxycholate, and 0.5% Triton-X 100) supplemented with protease inhibitors and PhosStop (Sigma-Aldrich). In case of Proteinase K (PK) (Roche AG) digestion, protease inhibitors and PhosStop were

avoided. The bicinchoninic acid assay (BCA) was used to measure the total protein concentrations according to the manufacturer's instructions (Pierce). Immunoblots were performed using standard procedures. The samples, boiled at 95 °C in NuPAGE LDS Sample Buffer 1x (Invitrogen) supplemented with 1 mM DTT (Sigma-Aldrich), were loaded onto precast gels (Invitrogen), and blotted onto PVDF membranes (Invitrogen). Proteinase K (PK) digestion was performed at a final concentration of 2.5 µg/ml for 30 minutes at 37°C. Following are the antibodies used and their relative dilutions: anti-Tfap2c 1:20000 (Abcam, ab76007), anti-hnRNP_K 1:2000 (Abcam, ab70492), anti-Cas9 (*S. pyogenes*) (7A9-3A3) 1:1000 (Cell Signaling Technology, 14697), anti-Puromycin 1:1000 (Kerafast, EQ0001), anti-PARP 1:1000 (Cell Signaling Technology, 9542S), anti-Cleaved Caspase 3 1:1000 (Cell Signaling Technology, 9661S), anti-Caspase 3 1:1000 (Novus Biologicals, NB100-56708), anti-GPX4 1:1000 (ab125066), anti-mCherry 1:1000 (Abcam, ab213511), anti-LC3 1:1000 (Cell Signaling Technology, #2775)**,** anti-Actin-HRP 1:10000 (Sigma-Aldrich, A3854), anti-Vinculin 1:2000 (Abcam, ab129002), anti-PrP POM1 300 ng/ml (for PrP^{Sc} detection) (*79*) or POM2 300 ng/ml (for total PrP or PrP^{C} detection) (*79*), anti-mTOR 1:1000 (Cell Signaling Technology, 29835S), anti-pAMPK 1:1000 (Cell Signaling Technology, 2535S), anti-AMPK 1:1000 (Cell Signaling Technology, 2532S), anti-pUlk1 1:1000 (Cell Signaling Technology, 6888T), anti-Ulk1 1:1000 (Cell Signaling Technology, 8054T), anti-4EBP1 1:1000 (Cell Signaling Technology, 9452S), anti-pS6 1:1000 (Cell Signaling Technology, 2215), anti-S6 1:1000 (Cell Signaling Technology, 2217), anti-Rabbit 1:5000 (Jackson ImmunoResearch, 111.035.045), anti-Mouse 1:5000 (BIO-RAD, STAR87P).

Lentivirus production

All the lentiviral vectors were produced as follows: HEK-293T cells were seeded at 40% confluency, and 24 hours later the target plasmid was co-transfected together with the pCMV-VSV-G (Addgene plasmid # 8454) (*80*) and psPAX2 plasmids (Addgene plasmid # 12260) using Lipofectamine 3000 transfection reagent (Invitrogen, ThermoFisher Scientific). After 6 hours, the medium was replaced with DMEM supplemented with 10% FBS and 1% HyClone Bovine Serum Albumin (Cytiva). 72 hours after the transfection, the supernatant was collected, centrifuged at 1500 RCF at 4°C for 5 minutes, filtered through a 0.45 µm filter (Whatman), aliquoted, and stored at -80°C. Viral titer was measured as previously reported (*81*). Cells were seeded at known numbers, infected with different volumes of lentivirus, and 24 hours later selected with the relevant antibiotics. The lentiviral Titer Unit (TU) was extrapolated by measuring the fraction of viable cells with CellTiter-Glo 2.0 and GloMax Plate reader (Promega). For plasmids bearing a fluorescent probe, the viral titer was measured by flow cytometry: briefly, cells were seeded in a 24-well plate and infected with different volumes of lentivirus after 6 hours; 72 hours after the infection, the cells were harvested, and the percentage of fluorescent positive cells

was acquired by flow cytometry (BD LSRFortessa, Cell Analyzer) and analyzed by FlowJo 10 (Tree Star).

Whole-genome CRISPR-Cas9 screen and analysis

The human Brunello CRISPR ablation pooled library (Addgene #73178) (*33*) was amplified as previously reported (*81*), packaged into a lentiviral vector, and titrated as described above. The library was transduced into 280 million LN-229 C3 cells with a multiplicity of infection (MOI) of 0.3 at an estimated coverage of around 1100 cells expressing each sgRNA. The screen was performed as follows. Day 0: 1 million cells/ml were seeded in a final volume of 31.25 ml per flask in 9 T-300 flasks. Cell density was defined based on the original titration of the lentiviral packaged Brunello Library. 6 hours later, the cells were transduced with the packaged library. Day 1: 24 hours after the delivery of the library, half of the culture (280 million cells) was transferred into new T-300 flasks in DMEM supplemented with 15 µg/ml blasticidin and 1 µg/ml puromycin (Thermo Fisher Scientific). The other half (280 million cells) was harvested, pelleted, and frozen at -80°C. Day 5: At this point, all the uninfected cells were depleted, and 80 million cells were re-seeded to maintain a library coverage >1000x. Day 7: 160 million cells were seeded at a concertation of 1 million cells/ml. 6 hours later, half of the culture was transduced either with qgRNAs against the *HNRNPK* gene or with the non-targeting control qgRNAs (NT) at an MOI of 10. Day 8: 24 hours after the delivery of the *HNRNPK* or NT qgRNAs, 160 million cells were transferred into 20 T-300 flasks and maintained under selection with 15 µg/ml blasticidin, 1 µg/ml puromycin and 1.5 mg/ml geneticin (Thermo Fisher Scientific). *HNRNPK*-targeted cells were incubated for six more days, changing the medium every three days. Day 11: To avoid over-confluency, the cells transduced with the NT qgRNAs were split according to the library coverage. Day 14: 80 million cells from both conditions were harvested, pelleted, and frozen at -80°C.

The extraction of the genomic DNA (gDNA), the preparation, and the purification of the NGS library were performed as previously reported (*81*). Briefly, the gDNA was harvested from each of the collected samples using the Zymo Research Quick-gDNA MidiPrep (Zymo Research) according to the manufacturer's protocol. To amplify the sgRNAs for NGS, a PCR reaction was set up for 23 cycles in 96 PCR plates (Sarstedt). Each gDNA sample was processed by using a mix of eight P5 primers in combination with one unique P7 primer. For the purification of the amplified product, the PCR reaction was mixed with five volumes of DNA Binding Buffer (Zymo Research), transferred in the Zymo-Spin V column with Reservoir (Zymo Research), and centrifuged at 500 RCF for 5 minutes at room temperature. The column was washed twice with 2 ml DNA Wash Buffer (Zymo Research) by a second step of centrifugation. The column was transferred to a 2 ml collection tube and spun again at maximum speed for 1 minute to remove residual wash buffer, and finally, the purified PCR reaction was eluted with

Nuclease-Free Water (Invitrogen). The PCR product was quantified from agarose gel, and the samples sequenced by Illumina Novaseq 6000 Full SP Flowcell.

The Sushi data analysis platform (*82*) (FGCZ, University of Zurich) or R (version 3.5.2) were utilized for data analysis and graphical visualizations. Reads quality was assessed using FastQC. Reads were aligned to the Human Brunello CRISPR ablation pooled library (*33*) with targeted gene symbols. Read counts were generated using the featureCounts function (*83*) from the Rsubread package in R. A generalized linear model applying Trimmed Means of M-values (TMM) normalization was implemented using the EdgeR package in R (*84*) for differential expression analysis. Clustering analysis was performed with the hclust function from the R stats package. Differential gene enrichment was performed using Edge R (version 3.5.2) by providing the $\log_2$ fold change and false discovery rate (FDR). sgRNAs have been grouped according to their targeted gene for the generation of the final gene lists.

Essential genes identification

To identify the set of essential genes in LN-229 cells, the Cancer Dependency Map's "2021-Q3" release (*49*) served as the primary resource. Genes whose "gene_effect" scored below -1 were classified as essential. The gene symbols were aligned with those referenced in the Brunello Library. The genes missing in the Brunello Library were excluded from the final list and the following analysis (Supp. Table 2).

CRISPR ablation and activation qgRNAs

Effects of CRISPR ablation were always analyzed 7 or 10 days upon transduction of ablation qgRNAs, respectively, for LN-229 and U-251MG Cas9 cells, unless differently specified. CRISPR activation was always evaluated five days after delivery of transactivating qgRNAs.

HNRNPK intron-targeting sgRNAs were designed with a customized algorithm, and the specificity and efficacy metrics were calculated using the GPP sgRNA designer (*33, 85*), GuideScan (*86*), and CRISPOR (*87*) tools. The selected guides were then cloned inside the pYJA5_G418 backbone (*88*), a modified version of the pYJA5 vector (*32*), containing the geneticin resistance marker instead of puromycin resistance. The sequence of the intron-targeting sgRNAs and their score parameters are reported in Supp. Table 1.

The *HNRNPK* ablation qgRNAs and its non-targeting control NT were provided by Jiang-An Yin (*32*) and cloned into the pYJA5_G418 backbone All the other ablation and activation qgRNAs were cloned in the pYJA5, stocked in-house and kindly provided by Jiang-An Yin (*32*) in the form of glycerol stocks. The non-targeting control NT qgRNAs used for CRISPR ablation and CRISPR activation are listed as *Control_3* and *Control_13* (for the ablation) and *Control_5* (for the activation) in Jiang-An Yin et al. (*32*).

Cell survival analysis

For the clonogenic assay, cells were seeded in six-well plates (3 x 10^5 per well U251 MG cells and 1 x 10^5 per well LN-229 cells) and treated with qgRNAs against different genes the day after. The cells were incubated for different time points, washed twice with PBS, fixed with 4% paraformaldehyde (Thermo Fisher Scientific), stained with 0.5% crystal violet (Sigma-Aldrich) for 1 hour, washed three times with PBS, and dried before imaging.

For cell viability assay, cells were seeded in 96-well plates (1 x 10^4 per well U251 MG cells and 3 x 10^3 per well LN-229 cells) and treated with drugs or qgRNAs against different genes the following day. The cells were incubated for different time points and the viability was measured using CellTiter-Glo 2.0 and GloMax Plate reader (Promega).

Translation activity measurement

Translation activity was measured by puromycin labeling as previously described (*89*). Briefly, cells were pulse-chased with 10 µg/ml puromycin (Thermo Fisher Scientific) for 10 minutes and washed three times with PBS before harvesting. Proteins were immunoblotted with anti-Puromycin 1:1000 (Kerafast, EQ0001).

RNA preparation and qRT-PCR

RNA was isolated using the RNeasy Mini kit (Qiagen). RNA quality and concentration were measured with a NanoDrop spectrophotometer (Thermo Fisher Scientific). Reverse transcription was carried out with the Quantitect Reverse Transcription kit (Qiagen) as per the manufacturer's guidelines. For each sample, 10 ng of cDNA was loaded into 384-well PCR plates (Life Systems Design) in triplicates, and the detection was conducted using SYBR green (Roche). Readout was executed with ViiA7 Real-Time PCR systems (Thermo Fisher Scientific). The ViiA7 Real-Time PCR system (Thermo Fisher Scientific) was used for the readout, and the qRT-PCR data were processed using the $2^{-\Delta\Delta CT}$ method. Following are the primers' sequences: *HNRNPK* (Fwd: 5'-TTCAGTCCCAGACAGCAGTG-3', Rev: 5'-TCCACAGCATCAGATTCGAG-3'), *TFAP2C* (Fwd: 5'-GCCGTAATGAACCCCACTGA-3', Rev: 5'-TTCTTTACACAGTTGCTGGGC-3'), *GAPDH* (Fwd: 5'-TGCACCACCAACTGCTTAGC-3', Rev: 5'-GGCATGGACTGTGGTCATCAG-3').

Immunofluorescence imaging

For immunofluorescence imaging, cells were seeded and grown in an 8-well Culture Slide (Corning) and fixed in 4% paraformaldehyde for 20 minutes at room temperature. After three washes in PBS, the cells were blocked and permeabilized for 1 hour in FBS 10% supplemented with Triton X-100 0.2%.

Cells were then incubated with primary antibodies diluted in the blocking/permeabilizing solution for 2 hours at room temperature. Cells were washed in PBS three times before incubation with the indicated secondary antibody for 1 hour at room temperature. After three more washes, cells were stained with DAPI diluted 1:10000 (Sigma-Aldrich) for 10 minutes at room temperature, washed again in PBS, and mounted. Images were captured by Confocal Laser Scanning microscopy (Leica Stellaris 5 inverse). Following are the antibodies used and their relative dilutions: anti-Tfap2c 1:500 (Abcam, ab76007), anti-hnRNP_K 1:500 (Abcam, ab39975), anti-Rabbit Alexa488 1:500 (Invitrogen, A11008), anti-Mouse Alexa647 1:500 (Invitrogen, 21236).

RNA Sequencing

RNA was isolated with the RNeasy Mini Kit (Qiagen). The Illumina Truseq Total RNA protocol (ribosomal depletion) was used for the preparation of the libraries. The quality of both the RNA and the libraries was assessed using the Agilent 4200 TapeStation System (Agilent). Libraries were pooled equimolar and sequenced on an Illumina NovaSeq 6000 sequencer (single-end 100 bp), achieving an approximate depth of 40 million reads per sample. The experiment was conducted in triplicate, however, due to low RNA quality, downstream analysis was performed only for two replicates except for the *TFAP2C*/*HNRNPK* double-knockout condition for which three replicates could be analyzed. Transcript alignment was carried out using the STAR package. After normalizing the library data (Transcripts Per Million, TPM), we conducted differential gene expression analysis using the DESeq2 package (*90*). We identified upregulated and downregulated genes considering the $\log_2$ fold change and Bonferroni-corrected *p*-value.

RNAi silencing

HovL cells were seeded at a density of 2 x 10^5 cells/well in 6-well plates. The next day, culture media was exchanged with optiMEM (Gibco) without antibiotics, and siRNAs pre-mixed with RNAiMAX (0.3% final concentration) (Thermo Fisher Scientific) were delivered in a dropwise manner at a final concentration of 10 µM. Incubation lasted 72 hours. Media containing siRNAs was aspirated, and cells washed once with PBS and then lysed. Pools of three different siRNAs were used to downregulate each RNA target. siRNA sequences: *TFAP2C* (s14009, s14010, s14011. Thermo Fisher Scientific, #4392420), *HNRNPK* (s6737, s6738, s6739. Thermo Fisher Scientific, #4392420).

Co-immunoprecipitation

Cell extracts were prepared in PBS supplemented with protease inhibitors (Sigma-Aldrich) using mechanical disruption. BCA assay was used to measure the total protein concentrations according to

the manufacturer's instructions (Pierce). The protein sample was processed in Protein LowBind Tube (Eppendorf) during each step. For each condition, 1 or 3 mg of protein was incubated for 1 hour at 4°C with 10 µl pre-washed dynabeads (Invitrogen) to clear the lysate from unspecific interactions. The cleared lysate was then incubated overnight at 4°C with 50 µl antibody-conjugated dynabeads and the sample kept mixing on a spinning wheel. The day after, the flow-through was collected and the dynabeads washed three times in PBS supplemented with protease inhibitors. The samples, boiled at 95 °C in LDS 2x (Invitrogen) supplemented with 2 mM DTT (Sigma-Aldrich), were loaded onto a 10% gel (Invitrogen) and blotted onto a PVDF membrane (Invitrogen). Following are the antibodies used and the relative dilutions: anti-Tfap2c 1:30 (Abcam, ab218107), anti-hnRNP_K 1:1000 (Abcam, ab39975), anti-Tfap2c 1:5000 (Abcam, ab76007), anti-Actin HRP 1:10000 (Sigma-Aldrich, A3854), Normal Rabbit IgG (Merck, 12-370) diluted to match the concentration of anti-Tfap2c (Abcam, ab218107), VeriBlot 1:10000 (Abcam, ab131366).

Lipid peroxidation detection

Lipid peroxidation was measured by flow cytometry using Liperfluo (Dojindo, L248-10) according to the manufacturer's instructions. Δ*TFAP2C* and NT-transduced LN-229 C3 cells were seeded in a 24-well plate, transduced with NT or *HNRNPK* ablation qgRNAs, and the following day put under antibiotic selection for three more days. On day 4 the cells were stained with Liperfluo, detached, acquired by flow cytometry (BD LSRFortessa, Cell Analyzer), and analyzed with FlowJo 10 (Tree Star).

ATP level quantification

Intracellular ATP was measured via CellTiter-Glo 2.0 and GloMax Plate reader (Promega) and normalized to total protein synthesis by BCA assay (Pierce). Δ*TFAP2C* and NT-transduced LN-229 C3 cells were seeded in a 96-well plate, transduced with NT or *HNRNPK* ablation qgRNAs, and the following day put under antibiotic selection for three more days. On day 4, the cells were lysed, and protein and ATP levels quantified as specified above.

6D11 staining for imaging and flow cytometry

The immunostaining protocol was based on a previous publication (*65*). For imaging, cells were washed with PBS and fixed with 4% paraformaldehyde for 12 minutes. After PBS washing, cells were incubated with 3.5M guanidine thiocyanate (Sigma-Aldrich) for 10 minutes. Following, cells were washed five times with PBS and incubated with mouse monoclonal (6D11) anti-PrP antibody (BioLegends, ref. 808001) diluted 1:1000 in 25% Superblock (Thermo Fisher Scientific) at room temperature for 1 hour. After washing once with PBS, cells were labeled with secondary antibody (dilution 1:1000, anti-Mouse

Alexa647, Invitrogen, 21236) along with DAPI (Sigma-Aldrich) in 25% Superblock for 1 hour at room temperature. Cells were washed once with PBS and imaged with Fluoview FV10i confocal microscope (Olympus Life Science)

For flow cytometry, HovL cells were dissociated and fixed using the Cyto-Fast™ Fix/Perm buffer set (BioLegends, ref. 426803) according to the manufacturer's instructions. Additionally, after fixation, samples were incubated in 3.5M guanidine thiocyanate (Sigma-Aldrich) for 10 minutes and then immediately washed with 1 ml 1x Cyto-Fast™ Perm wash solution to ensure PrP^{Sc}-specific binding (*65*). Staining was performed using AlexaFluor®-647 mouse monoclonal anti-PrP antibody (6D11) (BioLegends, ref. 808008) diluted 1:200 in 1x Cyto-Fast™ Perm wash solution. Data were acquired on SP6800 spectral analyzer (Sony Biotechnology Inc), and analysis was performed using FlowJo 10 (Tree Star).

Plasmids

pCMV-VSV-G was a gift from Bob Weinberg (Addgene plasmid # 8454 ; http://n2t.net/addgene:8454 ; RRID:Addgene_8454) (*80*). psPAX2 was a gift from Didier Trono (Addgene plasmid # 12260 ; http://n2t.net/addgene:12260 ; RRID:Addgene_12260). pXPR_011 was a gift from John Doench & David Root (Addgene plasmid # 59702 ; http://n2t.net/addgene:59702 ; RRID:Addgene_59702) (*91*). Human Brunello CRISPR knockout pooled library was a gift from David Root and John Doench (Addgene # 73178) (*33*). pXPR_120 was a gift from John Doench & David Root (Addgene plasmid # 96917 ; http://n2t.net/addgene:96917 ; RRID:Addgene_96917) (*92*). lentiCas9-Blast was a gift from Feng Zhang (Addgene plasmid # 52962 ; http://n2t.net/addgene:52962 ; RRID:Addgene_52962) (*78*). HA-tagged or untagged full-length *HNRNPK* plasmids were a gift from Ralf Bartenschlager (*93*). TFORF1330 was a gift from Feng Zhang (Addgene plasmid # 143950 ; http://n2t.net/addgene:143950; RRID:Addgene_143950) (*94*). TFORF3550 was a gift from Feng Zhang (Addgene plasmid # 145026 ; http://n2t.net/addgene:145026 ; RRID:Addgene_145026) (*94*). pSpCas9(BB)-2A-GFP (PX458) was a gift from Feng Zhang (Addgene plasmid # 48138 ; http://n2t.net/addgene:48138 ; RRID:Addgene_48138) (*95*). PSF-EF1-UB-NEO/G418 ASCI - EF1 ALPHA PROMOTER G418 SELECTION PLASMID (Sigma-Aldrich, OGS606-5U).

Drugs

Erastin (Merck, E7781-1MG); Baicalein (Merck, 465119-100MG); Liproxstatin-1 (MedChemExpress, HY-12726); Ferrostatin-1 (MedChemExpress, HY-100579); Staurosporin (Abcam, ab120056); Z-VAD(Ome)-FMK (Cayman Chemical, Cay14463-1); Rapamycin (Selleckchem, S1039); Torin1 (Sigma-Aldrich, 475991-10MG).

Data availability

Raw sequencing data and processed data from this manuscript are available via GEO accession number GSE279797.

References

1. Z. Wang *et al.*, The emerging roles of hnRNPK. *J Cell Physiol* **235**, 1995-2008 (2020).
2. https://www.proteinatlas.org/.
3. F. Pontén, K. Jirström, M. Uhlen, The Human Protein Atlas--a tool for pathology. *J Pathol* **216**, 387-393 (2008).
4. W. Cao, A. Razanau, D. Feng, V. G. Lobo, J. Xie, Control of alternative splicing by forskolin through hnRNP K during neuronal differentiation. *Nucleic Acids Res* **40**, 8059-8071 (2012).
5. W. M. Michael, P. S. Eder, G. Dreyfuss, The K nuclear shuttling domain: a novel signal for nuclear import and nuclear export in the hnRNP K protein. *EMBO J* **16**, 3587-3598 (1997).
6. E. F. Michelotti, G. A. Michelotti, A. I. Aronsohn, D. Levens, Heterogeneous nuclear ribonucleoprotein K is a transcription factor. *Mol Cell Biol* **16**, 2350-2360 (1996).
7. M. Mikula, K. Bomsztyk, K. Goryca, K. Chojnowski, J. Ostrowski, Heterogeneous nuclear ribonucleoprotein (HnRNP) K genome-wide binding survey reveals its role in regulating 3'-end RNA processing and transcription termination at the early growth response 1 (EGR1) gene through XRN2 exonuclease. *J Biol Chem* **288**, 24788-24798 (2013).
8. D. H. Ostareck *et al.*, mRNA silencing in erythroid differentiation: hnRNP K and hnRNP E1 regulate 15-lipoxygenase translation from the 3' end. *Cell* **89**, 597-606 (1997).
9. Y. Lubelsky, I. Ulitsky, Sequences enriched in Alu repeats drive nuclear localization of long RNAs in human cells. *Nature* **555**, 107-111 (2018).
10. Y. Xu *et al.*, New Insights into the Interplay between Non-Coding RNAs and RNA-Binding Protein HnRNPK in Regulating Cellular Functions. *Cells* **8**, (2019).
11. K. Bomsztyk, O. Denisenko, J. Ostrowski, hnRNP K: one protein multiple processes. *Bioessays* **26**, 629-638 (2004).
12. M. Gallardo *et al.*, Aberrant hnRNP K expression: All roads lead to cancer. *Cell Cycle* **15**, 1552-1557 (2016).
13. J. Lu, F. H. Gao, Role and molecular mechanism of heterogeneous nuclear ribonucleoprotein K in tumor development and progression. *Biomed Rep* **4**, 657-663 (2016).
14. L. S. Laursen, C. W. Chan, C. Ffrench-Constant, Translation of myelin basic protein mRNA in oligodendrocytes is regulated by integrin activation and hnRNP-K. *J Cell Biol* **192**, 797-811 (2011).
15. A. Folci *et al.*, Loss of hnRNP K impairs synaptic plasticity in hippocampal neurons. *J Neurosci* **34**, 9088-9095 (2014).
16. Y. Liu, B. G. Szaro, hnRNP K post-transcriptionally co-regulates multiple cytoskeletal genes needed for axonogenesis. *Development* **138**, 3079-3090 (2011).
17. P. Y. B. Au *et al.*, GeneMatcher aids in the identification of a new malformation syndrome with intellectual disability, unique facial dysmorphisms, and skeletal and connective tissue abnormalities caused by de novo variants in HNRNPK. *Hum Mutat* **36**, 1009-1014 (2015).
18. P. Y. B. Au, A. M. Innes, A. D. Kline, Au-Kline Syndrome. *GeneReviews*, (2019).
19. M. C. White *et al.*, Inactivation of hnRNP K by expanded intronic AUUCU repeat induces apoptosis via translocation of PKCdelta to mitochondria in spinocerebellar ataxia 10. *PLoS Genet* **6**, e1000984 (2010).
20. E. Braems *et al.*, HNRNPK alleviates RNA toxicity by counteracting DNA damage in C9orf72 ALS. *Acta Neuropathol* **144**, 465-488 (2022).
21. A. Bampton *et al.*, HnRNP K mislocalisation is a novel protein pathology of frontotemporal lobar degeneration and ageing and leads to cryptic splicing. *Acta Neuropathol* **142**, 609-627 (2021).
22. A. Bampton, L. M. Gittings, P. Fratta, T. Lashley, A. Gatt, The role of hnRNPs in frontotemporal dementia and amyotrophic lateral sclerosis. *Acta Neuropathol* **140**, 599-623 (2020).
23. D. Moujalled *et al.*, Kinase Inhibitor Screening Identifies Cyclin-Dependent Kinases and Glycogen Synthase Kinase 3 as Potential Modulators of TDP-43 Cytosolic Accumulation during Cell Stress. *PLoS One* **8**, e67433 (2013).

24. D. Moujalled *et al.*, Phosphorylation of hnRNP K by cyclin-dependent kinase 2 controls cytosolic accumulation of TDP-43. *Hum Mol Genet* **24**, 1655-1669 (2015).
25. D. Moujalled *et al.*, TDP-43 mutations causing amyotrophic lateral sclerosis are associated with altered expression of RNA-binding protein hnRNP K and affect the Nrf2 antioxidant pathway. *Hum Mol Genet* **26**, 1732-1746 (2017).
26. M. Avar *et al.*, An arrayed genome-wide perturbation screen identifies the ribonucleoprotein Hnrnpk as rate-limiting for prion propagation. *EMBO J* **41**, e112338 (2022).
27. A. Aguzzi, A. M. Calella, Prions: protein aggregation and infectious diseases. *Physiol Rev* **89**, 1105-1152 (2009).
28. A. Aguzzi, M. Polymenidou, Mammalian prion biology: one century of evolving concepts. *Cell* **116**, 313-327 (2004).
29. M. Gallardo *et al.*, hnRNP K Is a Haploinsufficient Tumor Suppressor that Regulates Proliferation and Differentiation Programs in Hematologic Malignancies. *Cancer Cell* **28**, 486-499 (2015).
30. https://depmap.org/portal/.
31. A. Tsherniak *et al.*, Defining a Cancer Dependency Map. *Cell* **170**, 564-576.e516 (2017).
32. J. Yin *et al.*, Robust and Versatile Arrayed Libraries for Human Genome-Wide CRISPR Activation, Deletion and Silencing. *bioRxiv*, 2022.2005.2025.493370 (2023).
33. J. G. Doench *et al.*, Optimized sgRNA design to maximize activity and minimize off-target effects of CRISPR-Cas9. *Nat Biotechnol* **34**, 184-191 (2016).
34. S. Xu *et al.*, Genome-wide CRISPR screen identifies ELP5 as a determinant of gemcitabine sensitivity in gallbladder cancer. *Nat Commun* **10**, 5492 (2019).
35. Y. Li *et al.*, The hnRNPK/A1/R/U Complex Regulates Gene Transcription and Translation and is a Favorable Prognostic Biomarker for Human Colorectal Adenocarcinoma. *Front Oncol* **12**, 845931 (2022).
36. J. R. Evans *et al.*, Members of the poly (rC) binding protein family stimulate the activity of the c-myc internal ribosome entry segment in vitro and in vivo. *Oncogene* **22**, 8012-8020 (2003).
37. T. Naganuma *et al.*, Alternative 3'-end processing of long noncoding RNA initiates construction of nuclear paraspeckles. *EMBO J* **31**, 4020-4034 (2012).
38. D. Szklarczyk *et al.*, The STRING database in 2023: protein-protein association networks and functional enrichment analyses for any sequenced genome of interest. *Nucleic Acids Res* **51**, D638-D646 (2023).
39. J. Chen *et al.*, TFAP2C-Activated MALAT1 Modulates the Chemoresistance of Docetaxel-Resistant Lung Adenocarcinoma Cells. *Mol Ther Nucleic Acids* **14**, 567-582 (2019).
40. Z. Gu *et al.*, TFAP2C-mediated LINC00922 signaling underpins doxorubicin-resistant osteosarcoma. *Biomed Pharmacother* **129**, 110363 (2020).
41. X. Jiang *et al.*, TFAP2C-Mediated lncRNA PCAT1 Inhibits Ferroptosis in Docetaxel-Resistant Prostate Cancer Through c-Myc/miR-25-3p/SLC7A11 Signaling. *Front Oncol* **12**, 862015 (2022).
42. T. L. Hoffman, A. L. Javier, S. A. Campeau, R. D. Knight, T. F. Schilling, Tfap2 transcription factors in zebrafish neural crest development and ectodermal evolution. *J Exp Zool B Mol Dev Evol* **308**, 679-691 (2007).
43. U. Werling, H. Schorle, Transcription factor gene AP-2 gamma essential for early murine development. *Mol Cell Biol* **22**, 3149-3156 (2002).
44. W. J. Lee *et al.*, hnRNPK-regulated LINC00263 promotes malignant phenotypes through miR-147a/CAPN2. *Cell Death Dis* **12**, 290 (2021).
45. T. M. Nguyen *et al.*, The SINEB1 element in the long non-coding RNA Malat1 is necessary for TDP-43 proteostasis. *Nucleic Acids Res* **48**, 2621-2642 (2020).
46. F. Chi, M. S. Sharpley, R. Nagaraj, S. S. Roy, U. Banerjee, Glycolysis-Independent Glucose Metabolism Distinguishes TE from ICM Fate during Mammalian Embryogenesis. *Dev Cell* **53**, 9-26.e24 (2020).
47. Y. Chen *et al.*, Hnrnpk maintains chondrocytes survival and function during growth plate development via regulating Hif1α-glycolysis axis. *Cell Death Dis* **13**, 803 (2022).

48. Z. Sun *et al.*, The Long Noncoding RNA Lncenc1 Maintains Naive States of Mouse ESCs by Promoting the Glycolysis Pathway. *Stem Cell Reports* **11**, 741-755 (2018).
49. I. Alim *et al.*, Selenium Drives a Transcriptional Adaptive Program to Block Ferroptosis and Treat Stroke. *Cell* **177**, 1262-1279.e1225 (2019).
50. G. Y. Liu, D. M. Sabatini, mTOR at the nexus of nutrition, growth, ageing and disease. *Nat Rev Mol Cell Biol* **21**, 183-203 (2020).
51. G. R. Steinberg, D. G. Hardie, New insights into activation and function of the AMPK. *Nat Rev Mol Cell Biol* **24**, 255-272 (2023).
52. Z. Li *et al.*, hnRNPK modulates selective quality-control autophagy by downregulating the expression of HDAC6 in 293 cells. *Int J Oncol* **53**, 2200-2212 (2018).
53. J. Kim, M. Kundu, B. Viollet, K. L. Guan, AMPK and mTOR regulate autophagy through direct phosphorylation of Ulk1. *Nat Cell Biol* **13**, 132-141 (2011).
54. M. Boccitto *et al.*, The Neuroprotective Marine Compound Psammaplysene A Binds the RNA-Binding Protein HNRNPK. *Mar Drugs* **15**, (2017).
55. T. C. Squier, Oxidative stress and protein aggregation during biological aging. *Exp Gerontol* **36**, 1539-1550 (2001).
56. N. Gregersen, P. Bross, Protein misfolding and cellular stress: an overview. *Methods Mol Biol* **648**, 3-23 (2010).
57. S. Alberti, A. A. Hyman, Biomolecular condensates at the nexus of cellular stress, protein aggregation disease and ageing. *Nat Rev Mol Cell Biol* **22**, 196-213 (2021).
58. R. A. Nixon, The role of autophagy in neurodegenerative disease. *Nat Med* **19**, 983-997 (2013).
59. F. M. Menzies *et al.*, Autophagy and Neurodegeneration: Pathogenic Mechanisms and Therapeutic Opportunities. *Neuron* **93**, 1015-1034 (2017).
60. O. Coskuner, I. V. Murray, Adenosine triphosphate (ATP) reduces amyloid-β protein misfolding in vitro. *J Alzheimers Dis* **41**, 561-574 (2014).
61. A. Patel *et al.*, ATP as a biological hydrotrope. *Science* **356**, 753-756 (2017).
62. M. Takaine, H. Imamura, S. Yoshida, High and stable ATP levels prevent aberrant intracellular protein aggregation in yeast. *Elife* **11**, (2022).
63. H. Yu *et al.*, HSP70 chaperones RNA-free TDP-43 into anisotropic intranuclear liquid spherical shells. *Science* **371**, (2021).
64. M. Avar *et al.*, Prion infection, transmission, and cytopathology modeled in a low-biohazard human cell line. *Life Sci Alliance* **3**, (2020).
65. J. M. Ribes *et al.*, Prion protein conversion at two distinct cellular sites precedes fibrillisation. *Nat Commun* **14**, 8354 (2023).
66. H. S. Chin *et al.*, VDAC2 enables BAX to mediate apoptosis and limit tumor development. *Nat Commun* **9**, 4976 (2018).
67. R. A. Panganiban *et al.*, Genome-wide CRISPR screen identifies suppressors of endoplasmic reticulum stress-induced apoptosis. *Proc Natl Acad Sci U S A* **116**, 13384-13393 (2019).
68. H. Gao *et al.*, A genome-wide CRISPR screen identifies HuR as a regulator of apoptosis induced by dsRNA and virus. *J Cell Sci* **135**, (2022).
69. M. Cai *et al.*, Genome-wide CRISPR-Cas9 viability screen reveals genes involved in TNF-α-induced apoptosis of human umbilical vein endothelial cells. *J Cell Physiol* **234**, 9184-9193 (2019).
70. E. H. Stover *et al.*, Pooled Genomic Screens Identify Anti-apoptotic Genes as Targetable Mediators of Chemotherapy Resistance in Ovarian Cancer. *Mol Cancer Res* **17**, 2281-2293 (2019).
71. M. Moder *et al.*, Parallel genome-wide screens identify synthetic viable interactions between the BLM helicase complex and Fanconi anemia. *Nat Commun* **8**, 1238 (2017).
72. D. M. Wilson *et al.*, Hallmarks of neurodegenerative diseases. *Cell* **186**, 693-714 (2023).
73. D. Pathak, A. Berthet, K. Nakamura, Energy failure: does it contribute to neurodegeneration? *Ann Neurol* **74**, 506-516 (2013).

74. S. Camandola, M. P. Mattson, Brain metabolism in health, aging, and neurodegeneration. *EMBO J* **36**, 1474-1492 (2017).
75. J. Mojsilovic-Petrovic *et al.*, FOXO3a is broadly neuroprotective in vitro and in vivo against insults implicated in motor neuron diseases. *J Neurosci* **29**, 8236-8247 (2009).
76. D. H. Abdelaziz, B. A. Abdulrahman, S. Gilch, H. M. Schatzl, Autophagy pathways in the treatment of prion diseases. *Current Opinion in Pharmacology* **44**, 46-52 (2019).
77. C. J. Cortes, K. Qin, J. Cook, A. Solanki, J. A. Mastrianni, Rapamycin delays disease onset and prevents PrP plaque deposition in a mouse model of Gerstmann-Sträussler-Scheinker disease. *J Neurosci* **32**, 12396-12405 (2012).
78. N. E. Sanjana, O. Shalem, F. Zhang, Improved vectors and genome-wide libraries for CRISPR screening. *Nat Methods* **11**, 783-784 (2014).
79. M. Polymenidou *et al.*, The POM monoclonals: a comprehensive set of antibodies to non-overlapping prion protein epitopes. *PLoS One* **3**, e3872 (2008).
80. S. A. Stewart *et al.*, Lentivirus-delivered stable gene silencing by RNAi in primary cells. *RNA* **9**, 493-501 (2003).
81. J. Joung *et al.*, Genome-scale CRISPR-Cas9 knockout and transcriptional activation screening. *Nat Protoc* **12**, 828-863 (2017).
82. M. Hatakeyama *et al.*, SUSHI: an exquisite recipe for fully documented, reproducible and reusable NGS data analysis. *BMC Bioinformatics* **17**, 228 (2016).
83. Y. Liao, G. K. Smyth, W. Shi, featureCounts: an efficient general purpose program for assigning sequence reads to genomic features. *Bioinformatics* **30**, 923-930 (2014).
84. M. D. Robinson, D. J. McCarthy, G. K. Smyth, edgeR: a Bioconductor package for differential expression analysis of digital gene expression data. *Bioinformatics* **26**, 139-140 (2010).
85. K. R. Sanson *et al.*, Optimized libraries for CRISPR-Cas9 genetic screens with multiple modalities. *Nat Commun* **9**, 5416 (2018).
86. A. R. Perez *et al.*, GuideScan software for improved single and paired CRISPR guide RNA design. *Nat Biotechnol* **35**, 347-349 (2017).
87. J. P. Concordet, M. Haeussler, CRISPOR: intuitive guide selection for CRISPR/Cas9 genome editing experiments and screens. *Nucleic Acids Res* **46**, W242-W245 (2018).
88. E. Lemes, University of Zurich, (2022).
89. E. K. Schmidt, G. Clavarino, M. Ceppi, P. Pierre, SUnSET, a nonradioactive method to monitor protein synthesis. *Nat Methods* **6**, 275-277 (2009).
90. M. I. Love, W. Huber, S. Anders, Moderated estimation of fold change and dispersion for RNA-seq data with DESeq2. *Genome Biol* **15**, 550 (2014).
91. J. G. Doench *et al.*, Rational design of highly active sgRNAs for CRISPR-Cas9-mediated gene inactivation. *Nat Biotechnol* **32**, 1262-1267 (2014).
92. F. J. Najm *et al.*, Orthologous CRISPR-Cas9 enzymes for combinatorial genetic screens. *Nat Biotechnol* **36**, 179-189 (2018).
93. M. Poenisch *et al.*, Identification of HNRNPK as regulator of hepatitis C virus particle production. *PLoS Pathog* **11**, e1004573 (2015).
94. J. Joung *et al.*, A transcription factor atlas of directed differentiation. *Cell* **186**, 209-229.e226 (2023).
95. F. A. Ran *et al.*, Genome engineering using the CRISPR-Cas9 system. *Nat Protoc* **8**, 2281-2308 (2013).
96. A. Subramanian *et al.*, Gene set enrichment analysis: a knowledge-based approach for interpreting genome-wide expression profiles. *Proc Natl Acad Sci U S A* **102**, 15545-15550 (2005).
97. V. K. Mootha *et al.*, PGC-1alpha-responsive genes involved in oxidative phosphorylation are coordinately downregulated in human diabetes. *Nat Genet* **34**, 267-273 (2003).
98. S. X. Ge, D. Jung, R. Yao, ShinyGO: a graphical gene-set enrichment tool for animals and plants. *Bioinformatics* **36**, 2628-2629 (2020).

Authors' contributions

S.S.: designed, performed, contributed, supervised, and coordinated all the experiments and analysis; generation of the LN-229 C3 cell model; data curation and visualization; writing of the manuscript. D.C.: performed bioinformatic analysis, data curation and visualization of the CRISPR screen and RNA-seq results (Fig. 1F, Fig. 4A-B, Supp. Fig. 2B-F, Supp. Table 2 to 5); assisted in cell culture for the generation of LN-229 C3 cell model; experimental design and writing of the manuscript. M.B.: performed or contributed to all the experiments illustrated from Fig. 3 to 6, and in Supp. Fig. 3, 5 and 7; performed co-immunoprecipitation assay (Fig. 2H-I, Supp. Fig. 3L); data curation and visualization; writing of the manuscript. G.M.: contributed to developing the 6D11 staining protocol; performed the 6D11 staining and flow cytometry analysis, data curation, and visualization (Fig. 6A, Supp. Fig. 6E); contributed to the experiments regarding prion propagation (Fig. 6, Supp. Fig. 6-7); contributed to the generation of the HovL cell model (Supp. Fig. 6); writing of the manuscript. M.C.: assisted with confocal image acquisition (Supp. Fig. 3J-K); performed flow cytometry analysis for isolation of the LN-229 C3 cell line (Supp. Fig. 1B); data curation and visualization; writing of the manuscript. L.F.: design of *HNRNPK* intron-targeting sgRNAs (Supp. Fig. 1C-D, Supp. Table 1); CRISPR screen data analysis, curation, and visualization (Fig. 1F, Supp. Fig. 2C); writing of the manuscript. V.B.: contributed to developing the 6D11 staining protocol; writing of the manuscript. C.O.M.: generation of the HovL cell model (Supp. Fig. 6); assisted in cell culture; data curation and visualization. D.L.V.: experimental design; assisted in cell culture; contributed to genomic DNA purification and sgRNA PCR amplification. S.N.: experimental design; assisted in cell culture; contributed to genomic DNA purification and sgRNA PCR amplification. F.B.: performed flow cytometry analysis, data curation and visualization (Supp. Fig. 4C). K.G.: generation of the LN-229 dCas9-VPR model; experimental design; assisted in cell culture; writing of the manuscript. J-A.Y.: designed and produced CRISPR qgRNAs. E.D.C.: contributed to developing the 6D11 staining protocol and flow cytometry data collection; experimental design and writing of the manuscript. A. A (Andrea Armani).: supervision, design, and technical support for the experiment related to mTOR, AMPK, ULK1, and autophagy (Fig. 5; Supp. Fig. 5); RNA-seq data curation and visualization (Fig. 4A-B); experimental design and writing of the manuscript. A.A. (Adriano Aguzzi): proposed the project, supervised its execution, secured funding, helped to write and correct the manuscript.

Funding and acknowledgments

A.A. is supported by institutional core funding by the University of Zurich, a Distinguished Scientist Award of the NOMIS Foundation, and grants from the Michael J. Fox Foundation (grant ID MJFF-022156 and grant ID MJFF-024255), the Swiss National Science Foundation (SNSF grant ID 179040 and grant ID 207872, Sinergia grant ID 183563), the GELU Foundation, swissuniversities (CRISPR4ALL), the Human Frontiers Science Program (grant ID RGP0001/2022), and Parkinson Schweiz. S.S. was

supported by UZH Candoc Grant 2022 (No. FK-22036) for the development of this project. D.C. and V.B. were supported by the UZH Candoc Grant 2022 and 2023, respectively. K.G. was the recipient of a grant from the Michael J. Fox Foundation (MJFF-022156). J-A.Y. was the recipient of the UZH postdoc grant 2021 and the Career Development Awards grant of the Synapsis Foundation - Alzheimer Research Switzerland ARS. E.D.C. is the recipient of the Synapsis Career Development Award (2022-CDA01) and the Parkinson Schweiz grant. Andrea A. is the recipient of a Marie Curie postdoctoral fellowship (MSCA GF, 101033310). We thank Dr. Merve Avar and Dr. Daniel Heinzer for their supervision in the Aguzzi's lab and their initial identification of the role of *HNRNPK* in prion propagation, which was the starting point for this project (*26*). We also thank Dr. Emina Lemes for the help setting up the screening strategy and protocol, Dr. Tingting Liu for support during the amplification of the Brunello library, Dr. Marian Hruska-Plochan, Lorenzo Maraio, Ana Marques, and Marigona Imeri for laboratory assistance, critical discussions, and technical help. Dr. Susanne Kreutzer, Dr. Maria Domenica Moccia, and the Functional Genomics Center Zurich (FGCZ) for preparing sequencing libraries, CRISPR screen NGS sequencing, RNA sequencing, quality control, and technical support, Dr. Aria Maya Minder Pfyl, Silvia Kobel and the Genomic Diversity Centre (GDC) of the ETH Zurich for RNA quality control and technical advice. The funders of the study had no role in study design, data collection, data analysis, data interpretation, or writing of the report. The corresponding author had full access to all the data in the study and had final responsibility for the decision to submit for publication. GSEA was run with GSEA 4.3.2 Broad Institute software (*96, 97*). Gene enrichment analysis was performed using ShinyGO 0.77 and 0.8 (*98*) online tools. Statistical analysis and graphs were generated with R (version 3.5.2) and GraphPad Prism version 10.2.0 for Windows, GraphPad Software, Boston, Massachusetts USA, www.graphpad.com. Fig.1E was created with BioRender.com.

Disclosure and competing interests statement

The authors declare that they have no conflict of interest.

Supplementary figures

Supplementary Figure 1.

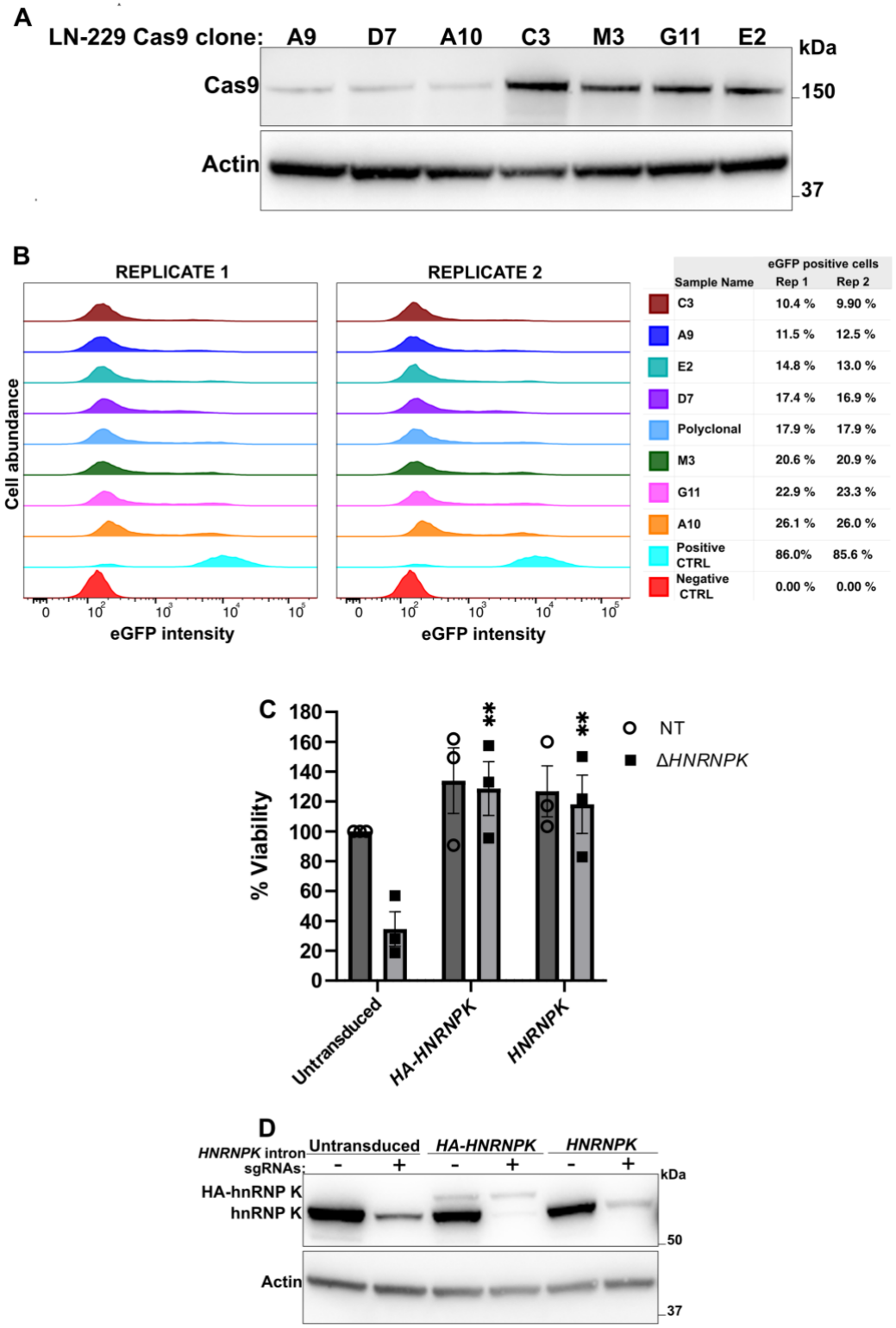

Supplementary Figure 2.

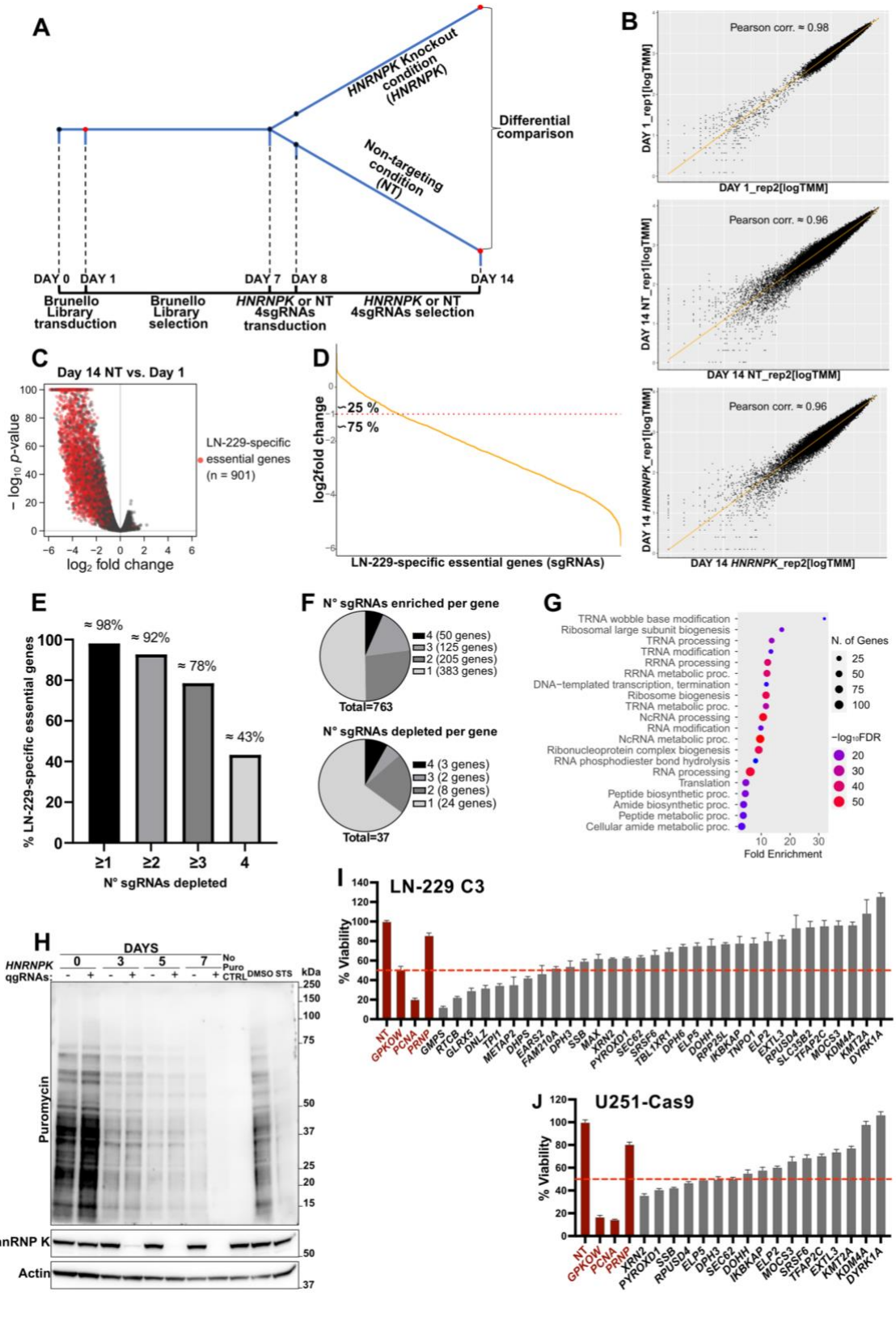

Supplementary Figure 3.

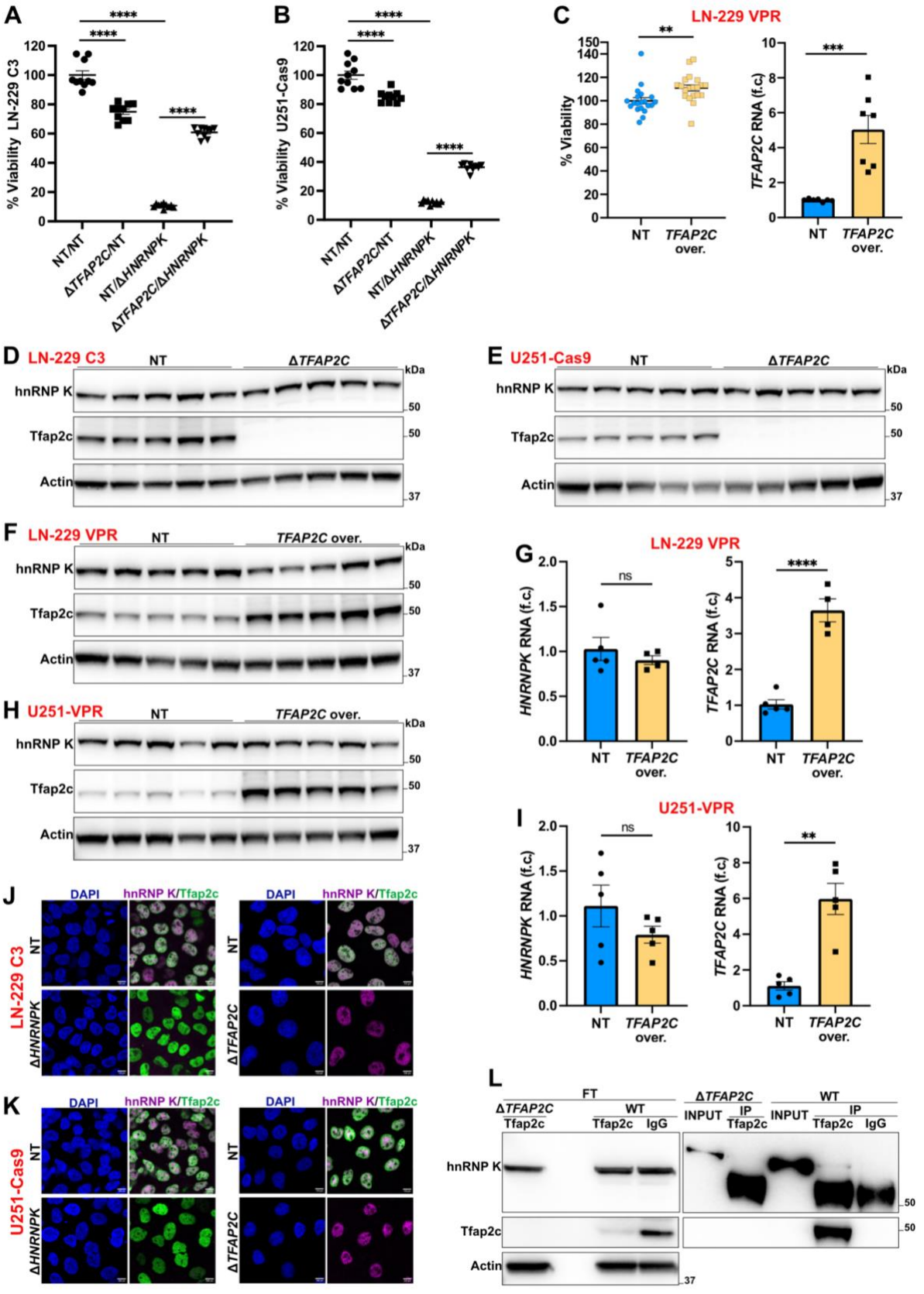

Supplementary Figure 4.

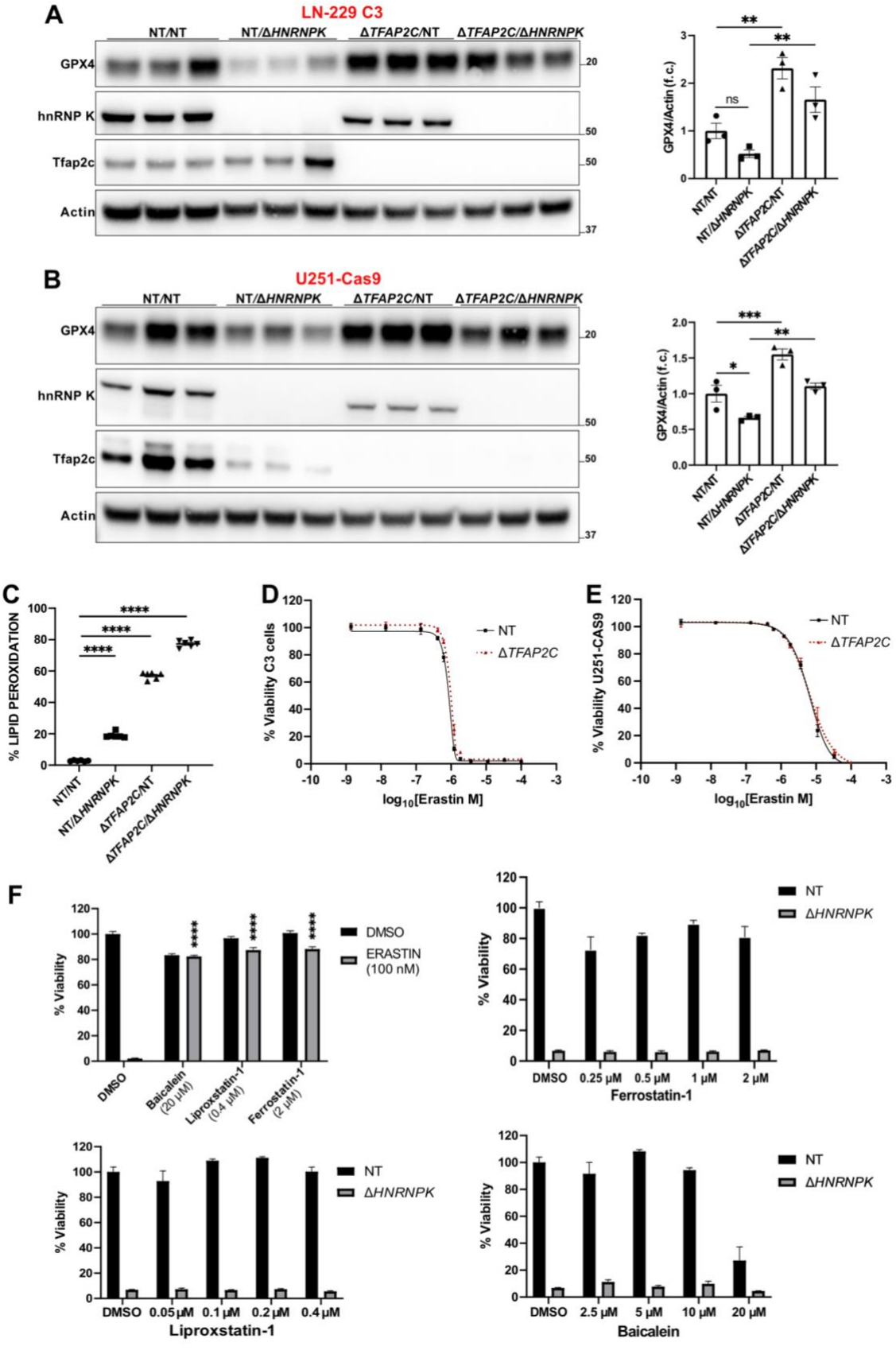

Supplementary Figure 5.

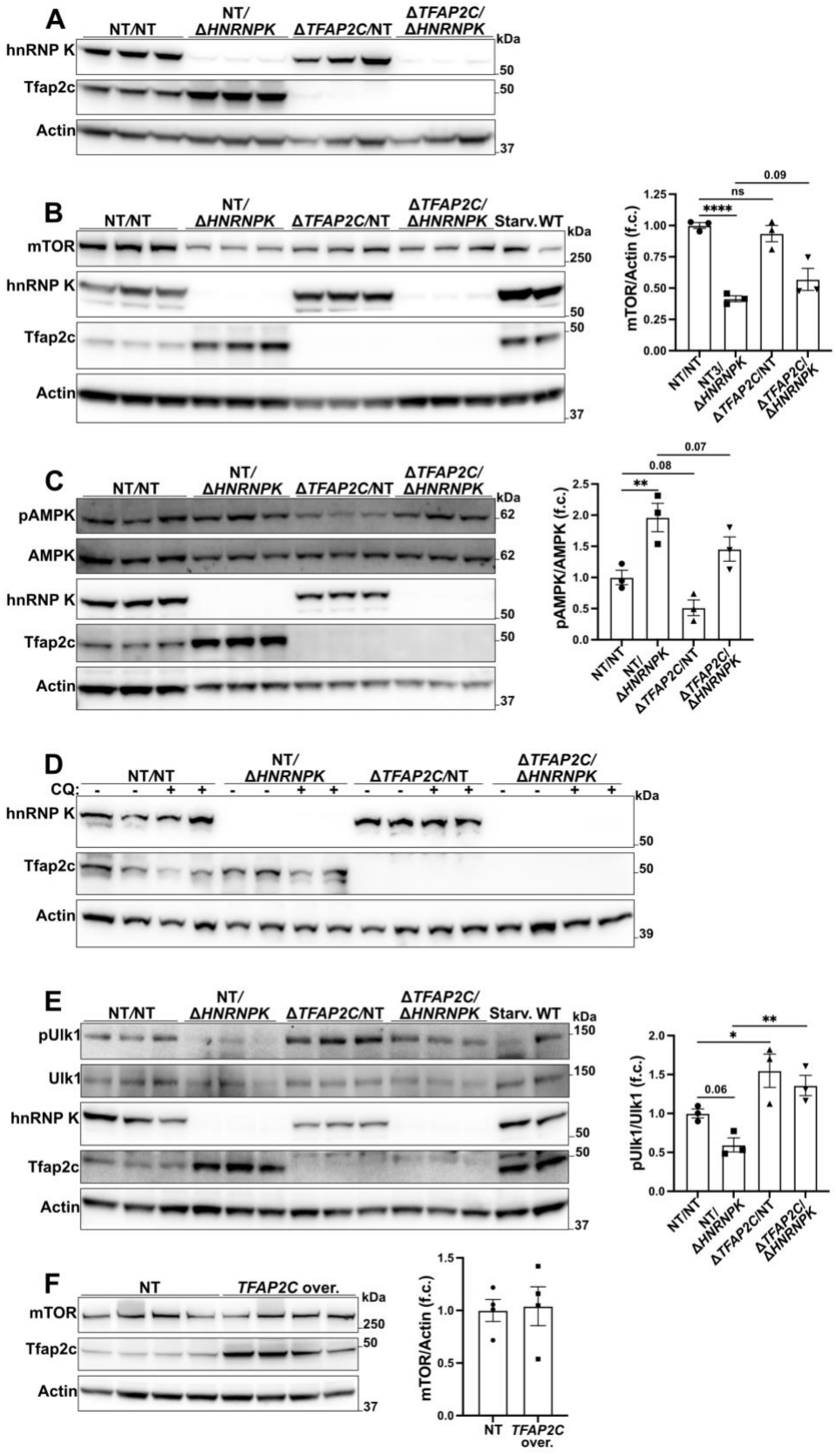

Supplementary Figure 6.

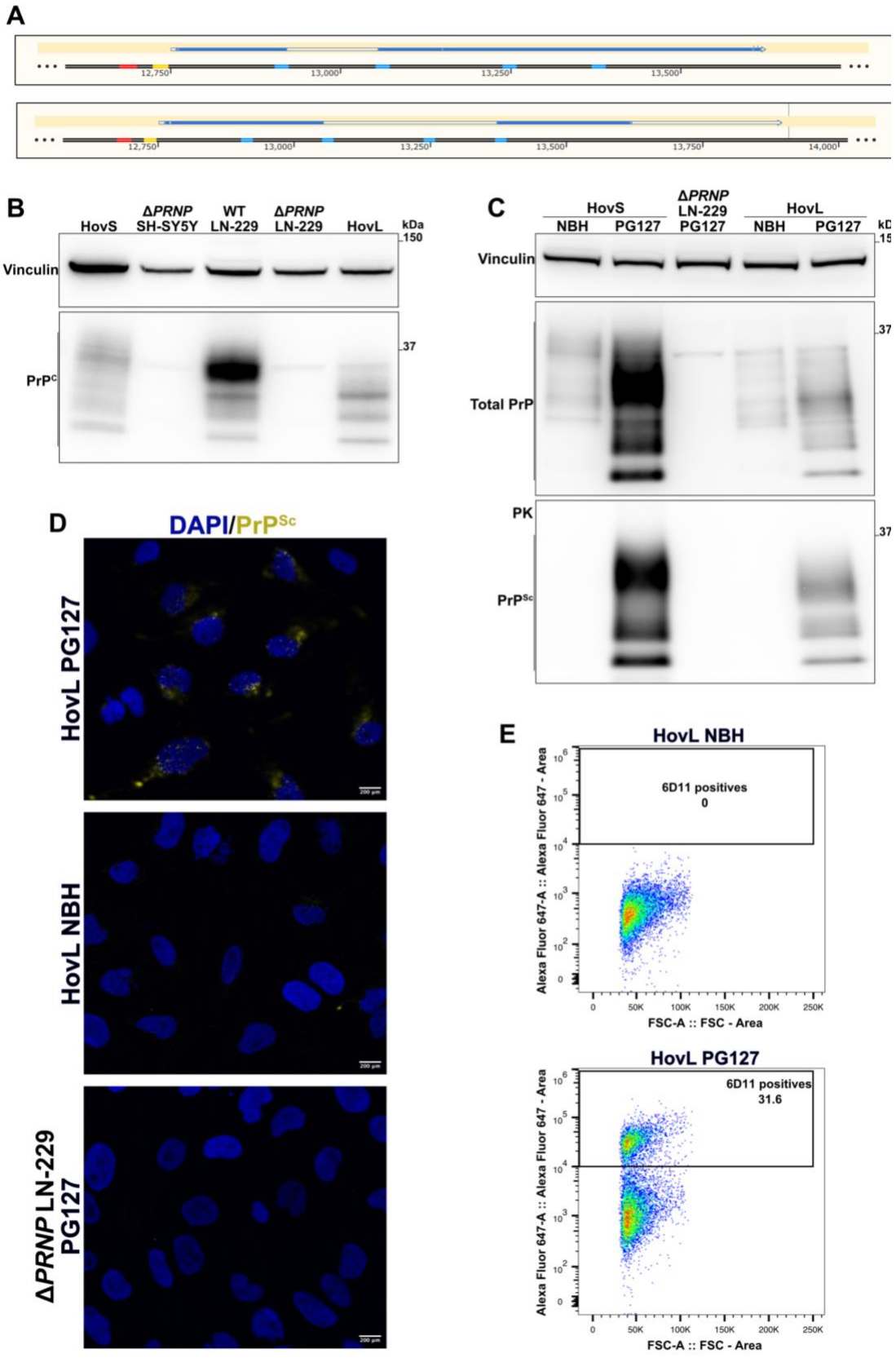

Supplementary Figure 7.

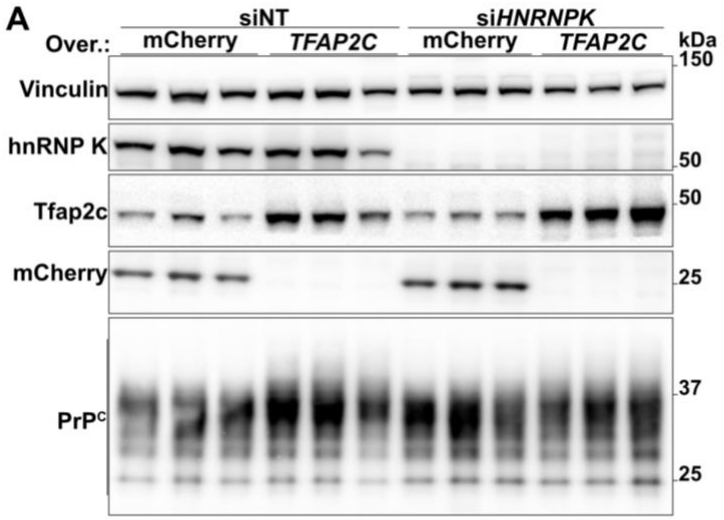

Supplementary figure captions

Supplementary Figure 1. A. Cas9 protein in isolated LN-229 Cas9 clones. **B.** Flow cytometry-based determination of Cas9 activity in the LN-229 Cas9 clones by an *eGFP* reporter assay. Cas9 activity was estimated from the percentage of the eGFP-negative cells. LN-229 not expressing Cas9 or the *eGFP* reporter were used as positive and negative controls, respectively. **C.** Viability of LN-229 C3 cells upon ablation of the *HNRNPK* endogenous gene (CellTiter-Glo assay). LN-229 C3 cells expressed a vector carrying either the *HA-HNRNPK* or the *HNRNPK* coding sequence. Untransduced cells were used for control. Results are normalized on the untransduced non-targeting condition (NT). $n = 3$. **D.** The western blot refers to the data shown in Supp. Fig. 1C. -: NT, +: *HNRNPK* sgRNAs. **Data information:** *n* represents independent cultures. Mean ± SEM. **: $p < 0.01$ (Two-way ANOVA Dunnett's test).

Supplementary Figure 2. A. Workflow of the genome-wide CRISPR deletion screen. The red dots highlight the three time points subjected to next-generation sequencing (NGS) and analysis (Day 1, Day 14 NT, Day 14 *HNRNPK*). **B.** Correlation between the two experimental replicates of the screen for the three analyzed conditions: Day 1, Day 14 NT, and Day 14 *HNRNPK* **C.** Volcano plot showing the differential sgRNAs abundance in Day 14 NT vs. Day 1. Red-filled circles indicate the sgRNAs targeting LN-229 essential genes. **D.** Distribution of sgRNAs targeting LN-229 essential genes in the Day 14 NT vs. Day 1 comparison. **E.** Percentage of LN-229 essential genes with at least one, two, three, or four sgRNAs depleted in the Day 14 NT vs. Day 1 comparison. **F.** Distribution of the number of sgRNAs per gene significantly enriched or depleted. **G.** Gene enrichment biological process analysis of the genes with ≥2 sgRNAs enriched in *HNRNPK* vs. NT at day 14. **H.** Puromycin labeling and detection of global protein synthesis in LN-229 C3 cells. -: NT, +: *HNRNPK* qgRNAs. 4 hours, 1 μM staurosoprine (STS) was used for control. **I, J.** Cell viability upon individual deletion of each of the candidate genes obtained from the screen (CellTiter-Glo assay). Results are normalized on the seeded cell density and compared to the non-targeting condition (NT). Red columns indicate the control groups: non-targeting control (NT), three unrelated genes (*PCNA*, *GPKOW*, *PRNP*). The red dashed line highlights the viability threshold set at 50% of the NT condition. Mean ± SEM, $n \geq 3$ independent cultures.

Supplementary Figure 3. A-B. Viability of Δ*TFAP2C* and NT-transduced cells 7 (A) and 10 days (B) upon delivering *HNRNPK* or NT qgRNAs (CellTiter-Glo assay). Results are normalized on the seeded cell density before *HNRNPK* ablation and on the double non-targeting condition (NT/NT). *n* = 10. **C.** Viability of LN-229 dCas9-VPR cells upon *TFAP2C* overexpression (CellTiter-Glo assay). Results are normalized on the non-targeting condition (NT). *n* = 20. qRT-PCR: *n* = 7. **D-E.** hnRNP K protein upon *TFAP2C* ablation. *n* = 5. **F-I.** hnRNP K protein (F, H) and RNA (G, I) after *TFAP2C* overexpression in dCas9-VPR cells. WB: *n* = 5. qRT-PCR**:** *n* ≥ 4. **J-K.** Confocal images showing hnRNP K and Tfap2c proteins in Δ*TFAP2C* and NT-transduced cells. hnRNP K and Tfap2c proteins were also imaged in cells transduced with *HNRNPK* or NT qgRNAs for 4 (J) or 6 (K) days. **L.** Co-immunoprecipitation of Tfap2c and hnRNP K in Δ*TFAP2C* and WT LN-229 C3 cells. IP: Immunoprecipitated Protein; FT: Flow Through after immunoprecipitation. **Data information:** *n* represents independent cultures. f.c.: fold change. Mean ± SEM. ns: $p > 0.05$, **: $p < 0.01$, ***: $p < 0.001$, ****: $p < 0.0001$ (Unpaired t-test in C, G, I. Two-way ANOVA Uncorrected Fisher's LSD in A-B).

Supplementary Figure 4. A-B. GPX4 protein after *HNRNPK* and *TFAP2C* ablation. *n* = 3. **C.** Percentage of Δ*TFAP2C* and NT-transduced LN-229 C3 cells showing lipid peroxidation 4 days after delivering *HNRNPK* and NT qgRNAs (Liperfluo staining). *n* = 6. **D-E.** Viability of Δ*TFAP2C* and NT-transduced cells, supplemented with erastin (CellTiter-Glo assay). Results are normalized on the DMSO-treated cells. *n* = 4. **F.** Viability of LN-229 C3 cells treated with erastin as a control (top left) or transduced with *HNRNPK* or NT qgRNAs and supplemented with anti-ferroptosis drugs: Ferrostatin-1 (top right), Liproxstatin-1 (bottom left), Baicalein (bottom right) (CellTiter-Glo assay). Results are normalized on the DMSO/NT condition. *n* ≥ 3. **Data information:** *n* represents independent cultures. f.c.: fold change. Mean ± SEM. *: $p < 0.05$, **: $p < 0.01$, ***: $p < 0.001$, ****: $p < 0.001$ (Two-way ANOVA Uncorrected Fisher's LSD in A-C and Dunnett's test in F).

Supplementary Figure 5. A, D. Ablations of *HNRNPK* and *TFAP2C* for RNA-seq samples (A) and from western blots shown in Fig. 5C (D), respectively. **B-C, E.** mTOR protein (B) and AMPK (C) and Ulk1 (E) phosphorylation ratio upon deletion of *HNRNPK* and *TFAP2C* in LN-229 C3 cells. 6h HBSS-starvation (starv.) was used as positive control *n* = 3. **F.** mTOR protein upon *TFAP2C* overexpression in LN-229 dCas9-VPR cells. **Data information:** *n* represents independent cultures. f.c.: fold change. Mean ± SEM. *: $p < 0.05$, **: $p < 0.01$ (Two-way ANOVA Uncorrected Fisher's LSD).

Supplementary Figure 6. A. qgRNAs (blue segments in reference sequence) in LN-229 cells promoted two major *PRNP* deletions from position 12922 to 13055 and from 13055 to 13372. **B.** Western blot showing the lack of the human PrP^C protein in the LN-229$^{\Delta PRNP}$ from Fig. 6A and the expression of the ovine PrP^C in the resulting HovL cells. HovS and SH-SY5Y$^{\Delta PRNP}$ cells were used as controls for the "ovinization" and the ablation, respectively. **C.** Proteinase K (PK) digested (bottom) and undigested (top) western blots showing respectively PrP^{Sc} and the total PrP in LN-229$^{\Delta PRNP}$ and HovL cells inoculated either with PG127 prion-infected Brain Homogenate (PG127) or with Not-infectious Brain Homogenate (NBH). PG127-infected and NBH mock-infected HovS cells were used as positive and negative controls, respectively. **D-E.** Imaging (D) and flow cytometry (E) analysis of anti-PrP^{Sc} 6D11 antibody signal in HovL cells treated as in C.

Supplementary Figure 7. A. PrP^C protein in uninfected HovL cells upon *HNRNPK* knockdown and *TFP2C* or mCherry (control) overexpression. *n* = 3. **B.** S6 protein phosphorylation ratio of HovL cells treated with 500nM of Torin1 and Rapamycin and used in Fig. 6D. **Data information:** Non-targeting scrambled siRNA (siNT) was used as a control. *n* represents independent cultures. f.c.: fold change. Mean ± SEM. ns: $p > 0.05$, **: $p < 0.01$(Two-way ANOVA Uncorrected Fisher's LSD).

Uncropped western blots

Fig. 1B:

The membrane was cut at 75kDa (1 and 2). Due to a techincal issue, the ladder was cut out from membrane 1. Membrane 1 was incubated with anti-Cas9. Membrane 2 was incubated in succession with anti-hnRNP_K (2), anti-actin (3) without stripping.

Fig. 1C:

The membrane was cut at 75kDa (1 and 2). For techincal problem membrane ladder was cut from membrane 1. Membrane 1 was incubated with anti-Cas9. Membrane 2 was incubated in succession with anti-hnRNP K (2), anti-actin (3) without stripping.

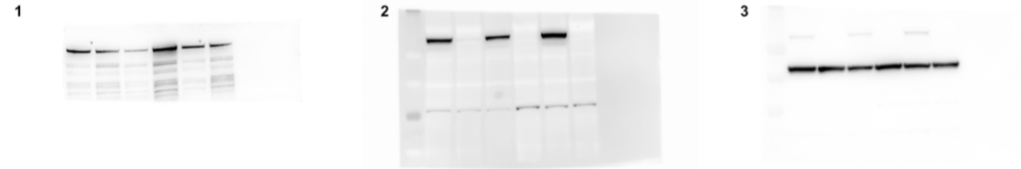

Fig. 1D:

The membrane was cut at 75kDa (1 and 2). For techincal problem membrane ladder was cut from membrane 1. Membrane 1 was incubated with anti-Cas9. Membrane 2 was incubated in succession with anti-hnRNP K (2), anti-actin (3) without stripping.

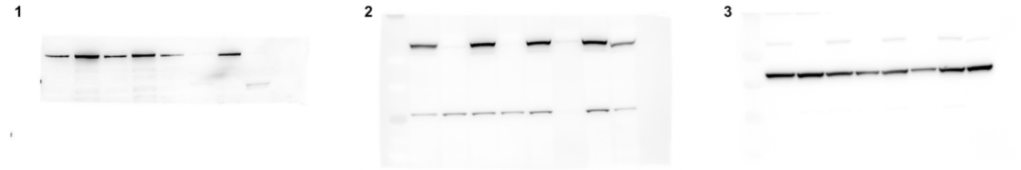

Fig. 2A:

The membrane was incubated in succession with anti-hnRNP K (1), anti-Tfap2c (2), anti-actin (3) without stripping.

Fig. 2B:

The membrane was incubated in succession with anti-hnRNP K (1), anti-Tfap2c (2), anti-Actin (3) without stripping

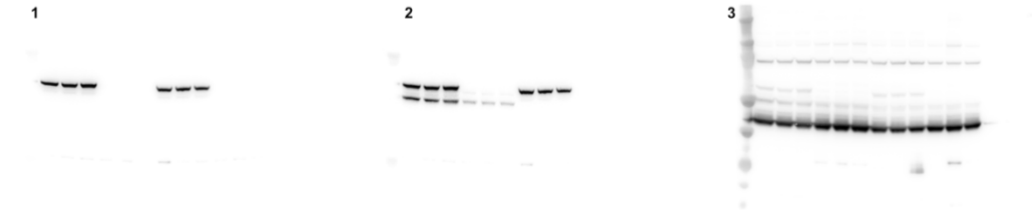

Fig. 2C:

The membrane was incubated in succession with anti-Tfap2c (1), anti-hnRNP K (2). After stripping, anti-Actin (3) was used.

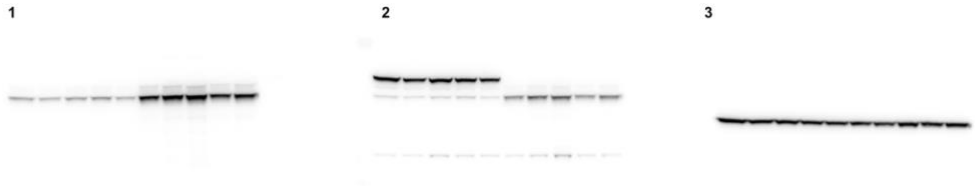

Fig. 2E:

The membrane was incubated in succession with anti-Tfap2c (1). After stripping we used anti-Actin (2), followed by anti-hnRNP K (3).

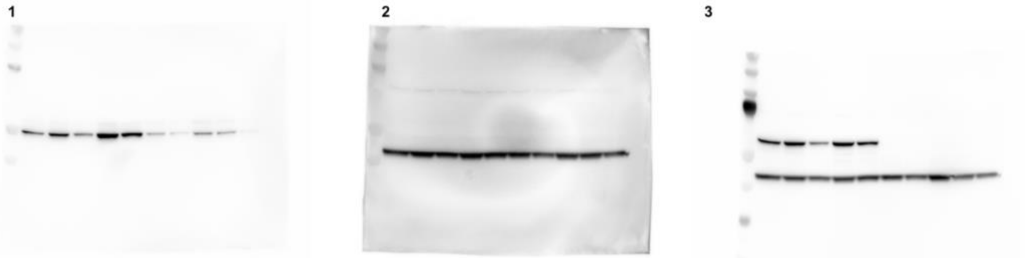

Fig. 2G:

The membrane was incubated in succession with anti-Tfap2c (1), anti-hnRNP K (2), anti-mCheey (3), anti-Actin (4) without stripping.

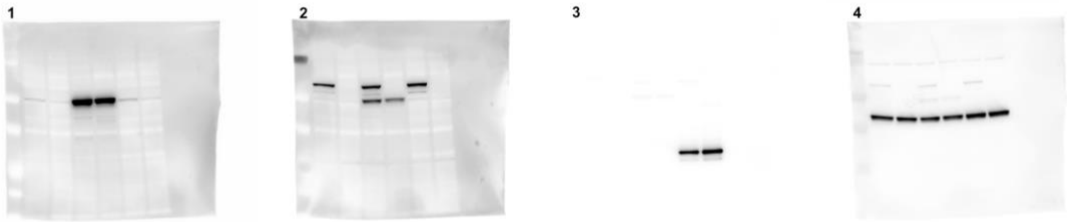

Fig. 2H:

The Co-IP membrane was incubated in succession with anti-hnRNP K (1), anti-tfap2c (2) without stripping. The FT membrane was incubated in succession with anti-hnRNP K (3), anti-Actin (4), anti-Tfap2c (5) without stripping.

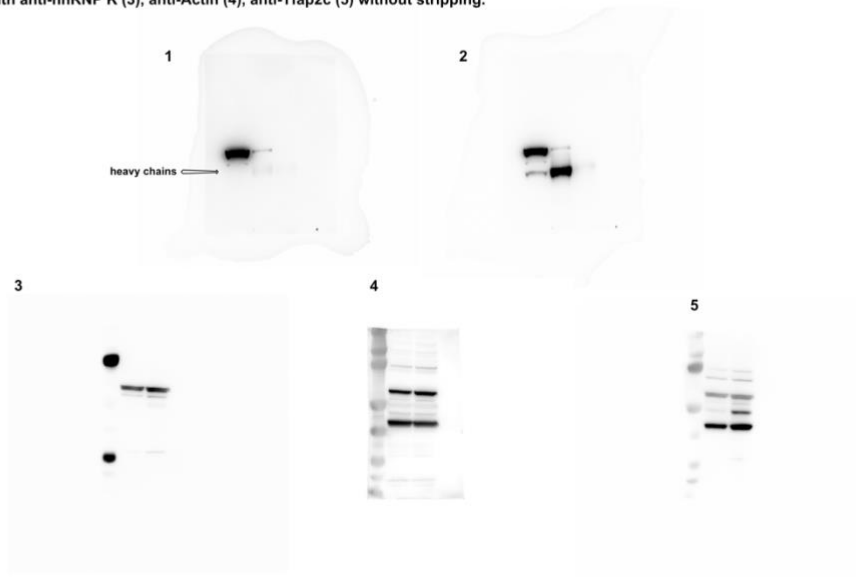

Fig. 2I:

The Co-IP membrane was incubated in succession with anti-hnRNP K (1), anti-Tfap2c (2) without stripping. The FT membarne was incubated in succession with anti-hnRNP K (3), anti-Tfap2c (4), anti-Actin (4) without stripping.

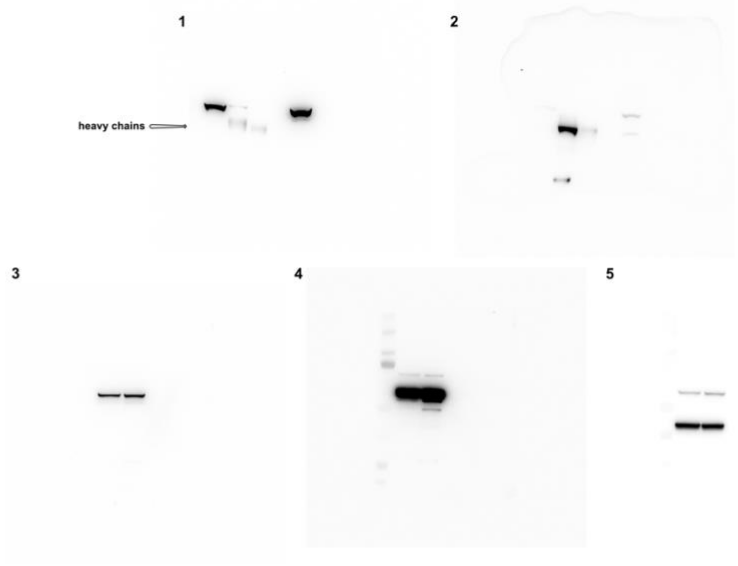

Fig. 3A:

The membrane was cut at 75kDa (1 and 6). The membrane 1 (10-75 kDa) was incubated in succession with anti-cleaved Caspase3 (1), anti-Tfap2c (2), anti-hnRNP K (3), anti-Actin (4), anti-full Caspase3 (5) without stripping. Membrane 6 (75-250 kDa) was incubated with anti-PARP.

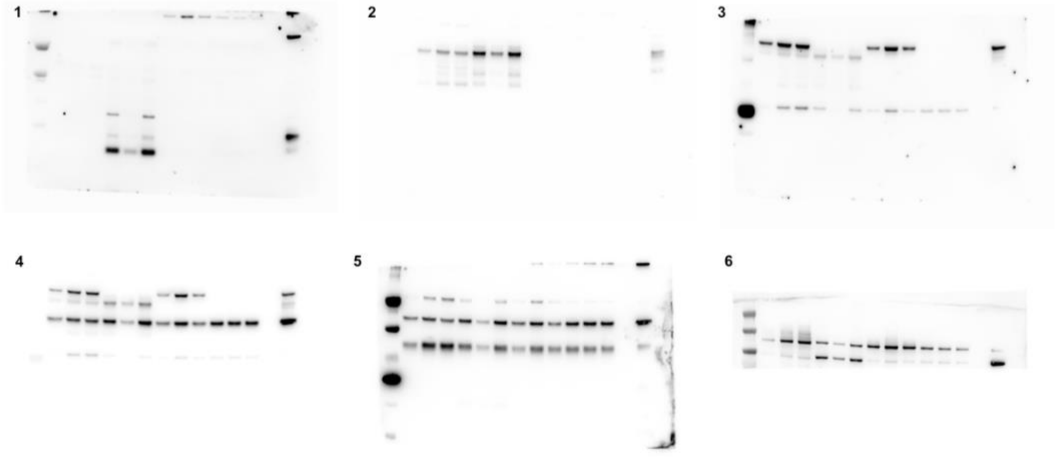

Fig. 3B:

The membrane was cut at 22kDa (1), 37kDa (2) and 70kDa (3 and 6). Membrane 1 (10-22 kDa) was incubated with anti-cleaved Caspase3. Membrane 2 (22-37 kDa) was incubated with anti-full Caspase3. Membrane 3 (37-70 kDa) was incubated in succession with anti-hnRNP K (3), anti-Tap2c (4), anti-Actin (5) witout stripping. Membrane 6 (70-250 kDa) was incubated with anti-PARP.

Fig. 5A

The membrane was cut just below 25 kDa, at 37 kDa and just below 75 kDa. Membrane 1 (10-23 kDa) was incubated with anti-4EBP1 (1). Membrane 2 (23-37 kDa) was incubated with anti-pS6 (2). After stripping, membrane 2 was incubated with anti-S6 (3). Membrane 4 (37-73 kDa) was incubated in succession with anti-Tfap2c (4), anti-hnRNP K (5). After stripping, membrane 4/5 was incubated with anti-Actin (6).

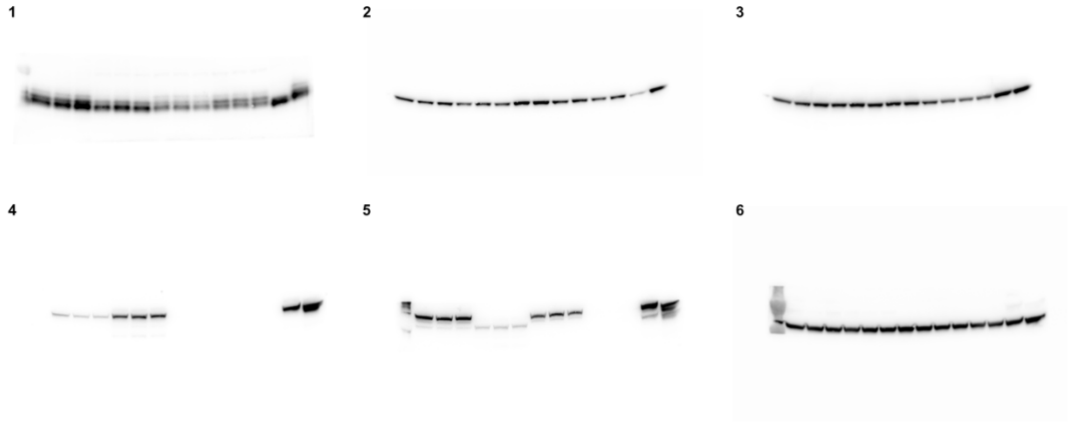

Fig. 5C and Supp. Fig. 5D:

The membrane was cut between 22-28 kDa (SeeBlue Ladder in MOPS) (1 and 4). Membrane 1 was incubated in succession with anti-hnRNP K (1), anti-Tfap2c (2) and after stripping with anti-Actin (3). Membrane 4 was incubated with anti-LC3B (4).

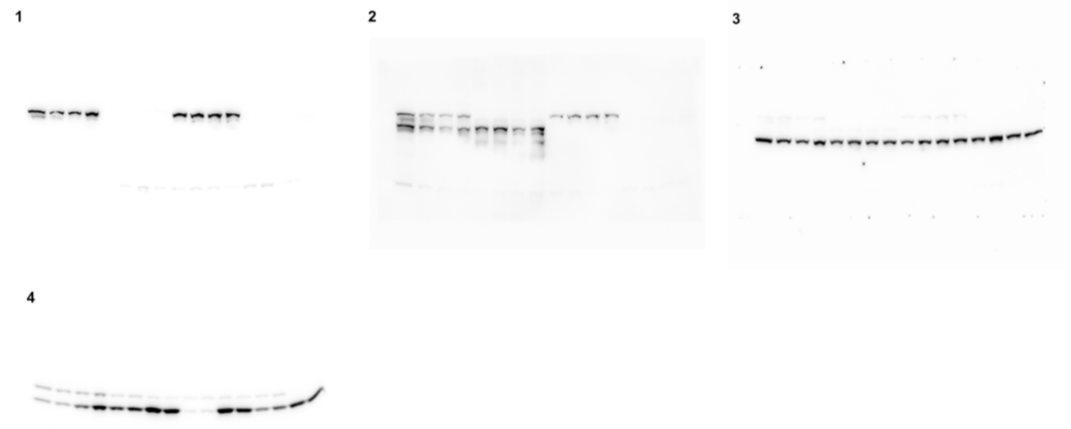

Fig. 5D and Supp. Fig. 5F:

The membrane was cut at 100 kDa (1 and 3). Membrane 1 (10-100 kDa) was incubated in succession with anti-4EBP1 (1), anti-pS6 (2) without stripping. Membrane 3 (100-300 kDa) was incubated with anti-mTOR (3). Membrane 1 (10-100 kDa) was then cut at 25 kDa. Membrane 4 (25-100kDa) was incubated with anti-Tfap2c (4). Membrane 4 was cut at 37 kDa and 50 kDa (5 and 6). Membrane 5 (25-37 kDa) was stripped and incubated with anti-S6 (5). Membrane 6 (37-50 kDa) was stripped and incubated with anti-Actin (6).

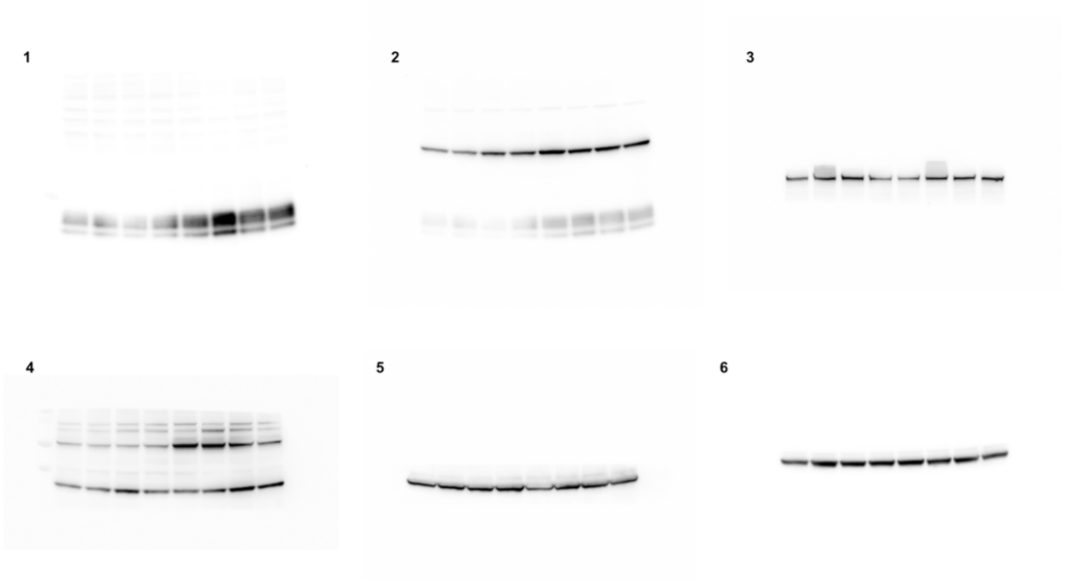

Fig. 6B:

The membrane was cut at 75 kDa (1 and 2). Membrane 1 (75-250 kDa) was incubated with anti-Vinculin (1). Membrane 2 (10-75 kDa) was incubated anti-PrP (POM2) (2). Membrane 2 was following cut at 45 kDa (3 and 4). Membrane 3 (45-75 kDa) was incubated with both anti-hnRNP K and anti-Tfap2c (3). Membrane 4 was stripped and then incubated with anti-Actin first (not shown in the main figures) and then with anti-mCherry (4). Membrane 5 was transferred with the same samples of membrane 1-5 pre-treated with PK digestion. Membarne 5 was incubated with anti-PrP (POM1) (5).

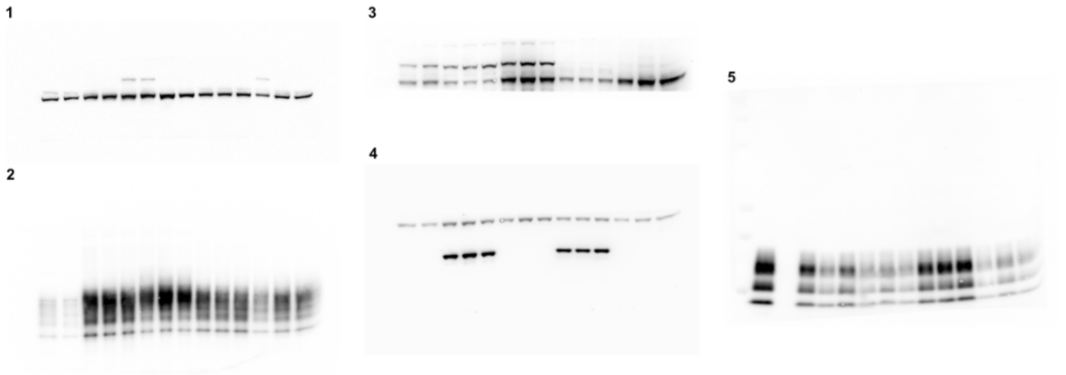

Fig. 5C and Supp. Fig. 5D:

The membrane was cut between 22-28 kDa (SeeBlue Ladder in MOPS) (1 and 4). Membrane 1 was incubated in succession with anti-hnRNP K (1), anti-Tfap2c (2) and after stripping with anti-Actin (3). Membrane 4 was incubated with anti-LC3B (4).

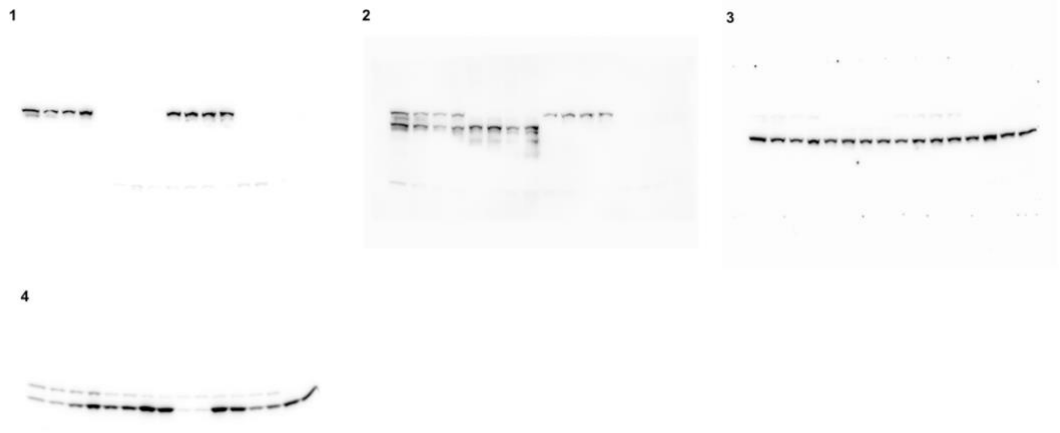

Fig. 5D and Supp. Fig. 5F:

The membrane was cut at 100 kDa (1 and 3). Membrane 1 (10-100 kDa) was incubated in succession with anti-4EBP1 (1), anti-pS6 (2) without stripping. Membrane 3 (100-300 kDa) was incubated with anti-mTOR (3). Membrane 1 (10-100 kDa) was then cut at 25 kDa. Membrane 4 (25-100kDa) was incubated with anti-Tfap2c (4). Membrane 4 was cut at 37 kDa and 50 kDa (5 and 6). Membrane 5 (25-37 kDa) was stripped and incubated with anti-S6 (5). Membrane 6 (37-50 kDa) was stripped and incubated with anti-Actin (6).

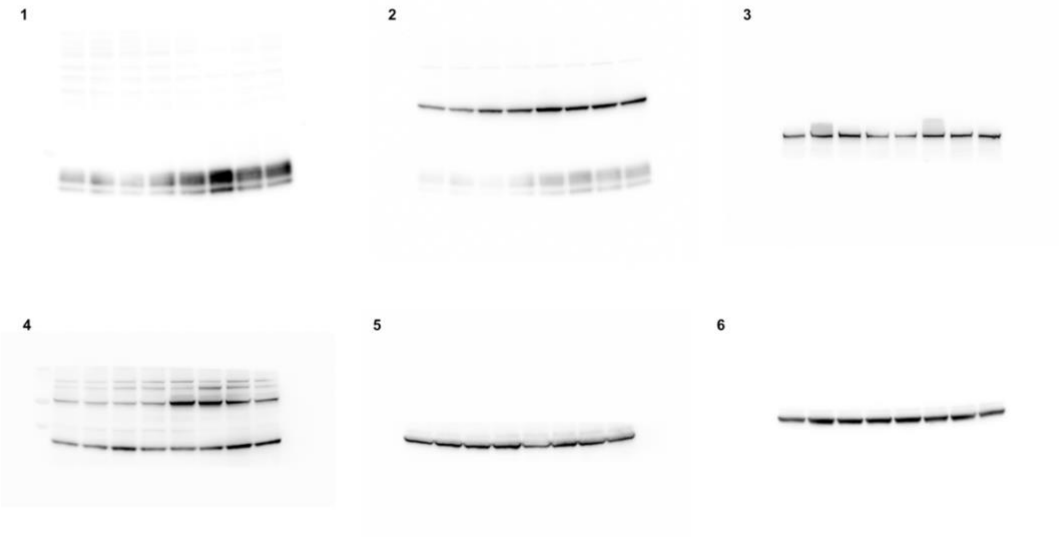

Fig. 6B:

The membrane was cut at 75 kDa (1 and 2). Membrane 1 (75-250 kDa) was incubated with anti-Vinculin (1). Membrane 2 (10-75 kDa) was incubated anti-PrP (POM2) (2). Membrane 2 was following cut at 45 kDa (3 and 4). Membrane 3 (45-75 kDa) was incubated with both anti-hnRNP K and anti-Tfap2c (3). Membrane 4 was stripped and then incubated with anti-Actin first (not shown in the main figures) and then with anti-mCherry (4). Membrane 5 was transferred with the same samples of membrane 1-5 pre-treated with PK digestion. Membarne 5 was incubated with anti-PrP (POM1) (5).

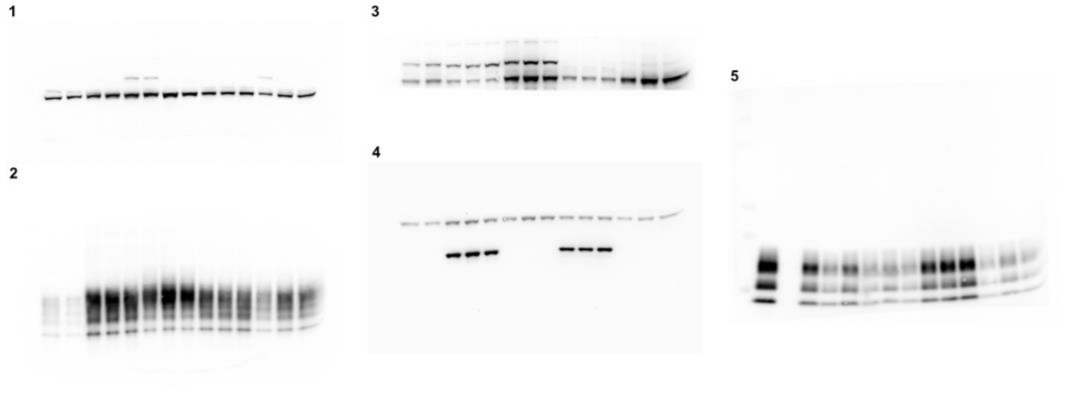

Fig. 6D:

The membrane was cut at 75 kDa (1 and 2). Membrane 1 (75-250 kDa) was incubated with anti-Vinculin (1). Membrane 2 (10-75 kDa) was incubated anti-PrP (POM2) (2). Membrane 3 was transferred with the same samples of membrane 1-2 pre-treated with PK digestion. Membarne 3 was incubated with anti-PrP (POM1) (3).

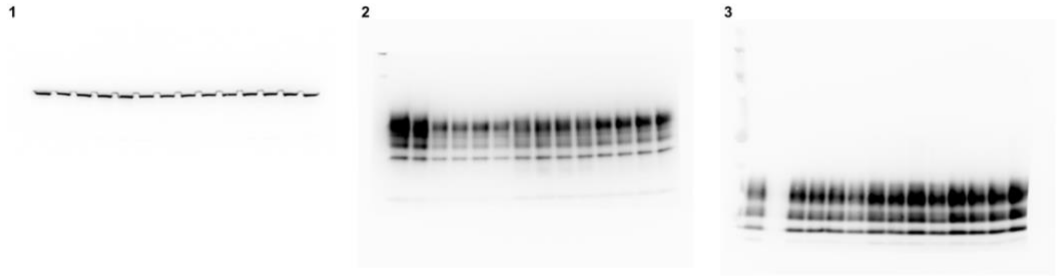

Supp. Fig. 1A:

The membrane was incubated with anti-Cas9 (1). After stripping, the membrane was incubated with anti-Actin (2).

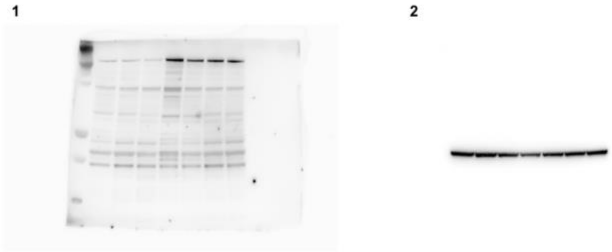

Supp. Fig. 1D:

The membrane was incubated in succession with anti-hnRNP_K (1), anti-Actin (2) without stripping. The last 4 lanes were loaded with lysates coming from C3 cells transduced with differented truncated variants of hnRNP K. They do not appear in the cropped figure because they are irrelevat to the aim of the described experiment. They were originally loaded on the same gel as controls for another unrelated experiment.

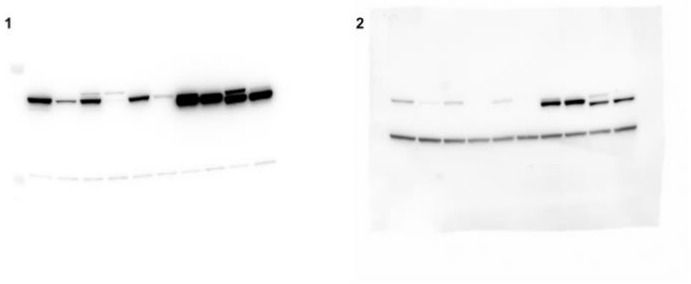

Supp. Fig. 2H:

The membrane was incubated with anti-Puromycin (1). After stripping it was incubated with anti-hNRNPK (2). After following stripping it was incubated with anti-Actin (3).

Supp. Fig. 3D:

The membrane was incubated in succession with anti-hnRNP K (1), anti-Tfap2c (2), anti-Actin (3) without stripping.

Supp. Fig. 3E

The membrane was incubated in succession with anti-hnRNP K (1), anti-Tfap2c (2), anti-Actin (3) without stripping.

Supp. Fig. 3F:

The membrane was incubated in succession with anti-hnRNP K (1), anti-Tfap2c (2), anti-Actin (3) without stripping.

Supp. Fig. 3H:

The membrane was incubated in succession with anti-hnRNP K (1), anti-Tfap2c (2), anti-Actin (3) without stripping.

Supp. Fig. 3L:

The Co-IP membrane was incubated with anti-hnRNP K (1). After stripping the membrane was incubated with anti-Tfap2c (2). The FT membrane was incubated in succession with anti-hnRNP K (3), anti-Actin (4) and anti-Tfap2c (5) without stripping.

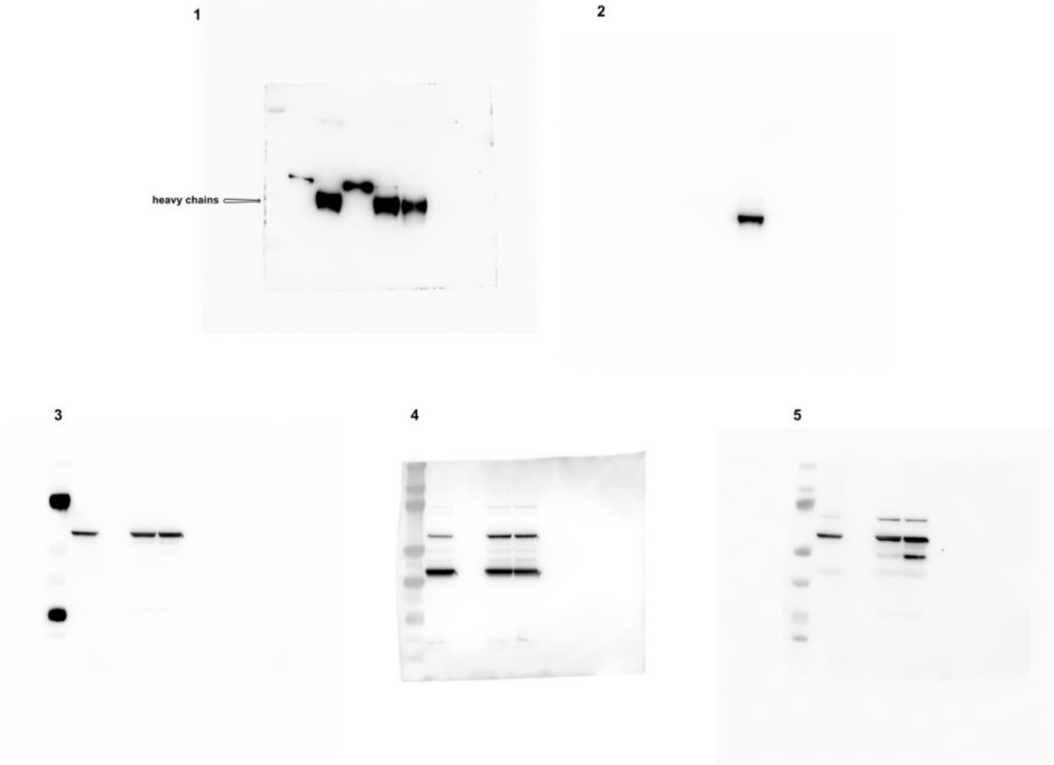

Supp. Fig. 4A:

The membrane was incubated in succession with anti-GPX4 (1), anti-Actin (2), anti-Tfap2c (3), anti-hnRNP K (4) without stripping.

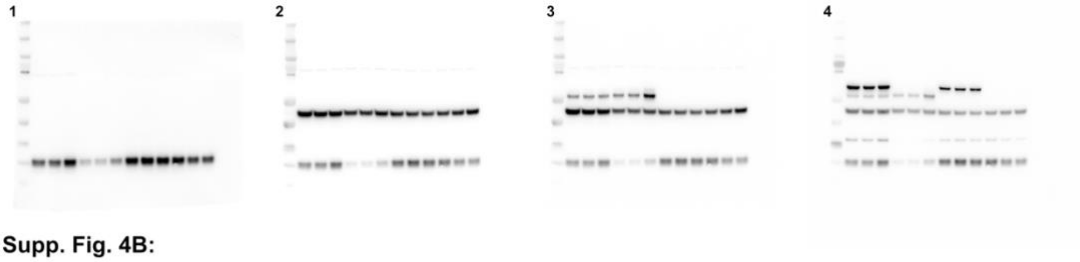

Supp. Fig. 4B:

The membrane was incubated in succession with anti-GPX4 (1), anti-Tfap2c (2), anti-hnRNP K (3), anti-Actin (4) without stripping.

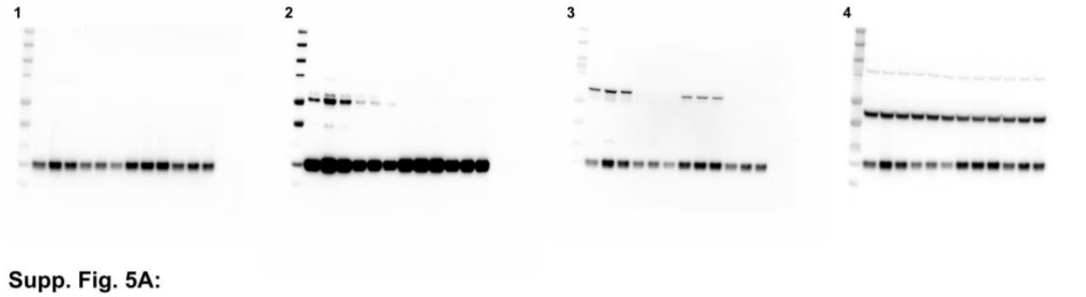

Supp. Fig. 5A:

The membrane was incubated in succession with anti-hnRNP K (1), anti-Tfap2c (2) without stripping. After stripping the membrane was incubated with anti-Actin (3).

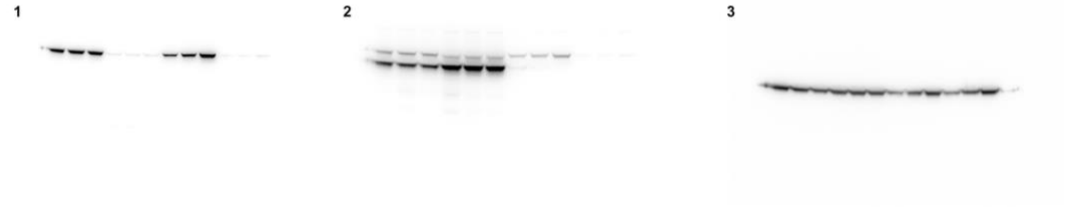

Supp. Fig. 5B:

The membrane was cut just below 37 kDa (2), at 75 kDa (4) and just below 150 kDa (1). The membrane 75-150 kDa was used for a different unrelated experiment and for this reason in not shown. Membrane 1 (140-300 kDa) was incubated with anti-mTOR. Membrane 2 (10-35 kDa) was initially incubated with anti-4EBP1 (not shown). Membrane 4 (75-140 kDa) was incubated in succession with anti-Tfap2c (4), anti-hnRNP K (5), and after stripping, with anti-Actin (6).

Supp. Fig. 5C:

The membrane was incubated in succession with anti-pAMPK (1), anti-Tfap2c (2), anti-hnRNP K (3), anti-Actin (4) without stripping. After stripping the membrane was incubated with anti-AMPK (5). The last two lane of the gel were loaded with unrelated samples.

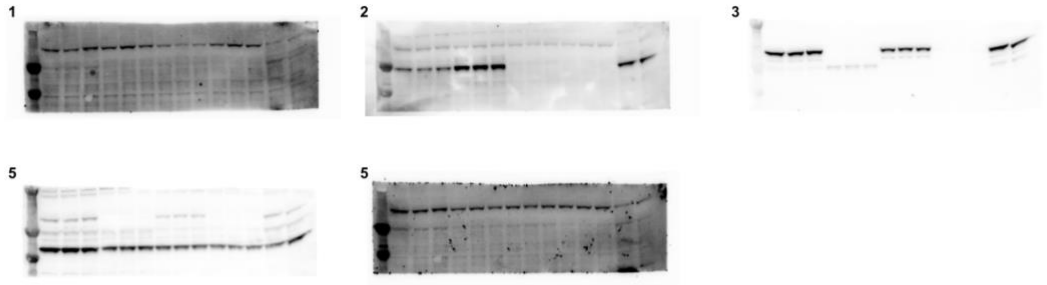

Supp. Fig. 5E:

The membrane was cut just above 75 kDa and below 37 kDa (1, 2 and 5). Membrane 1 (10-37 kDa) was incubated with anti-4EBP1 (not shown). Membrane 2 (37-75 kDa) was incubated in succession with anti-hnRNP K (2), anti-Tfap2c (3) without stripping (for Tfap2c acquisition the membrane was covered with alluminium foil to mask the too intense signal coming from hnRNP K). After stripping membrane 2 was incubated with anti-Actin (4). Membrane 5 was incubated with anti-pUlk1 (5) and, after stripping, with anti-Ulk1 (6).

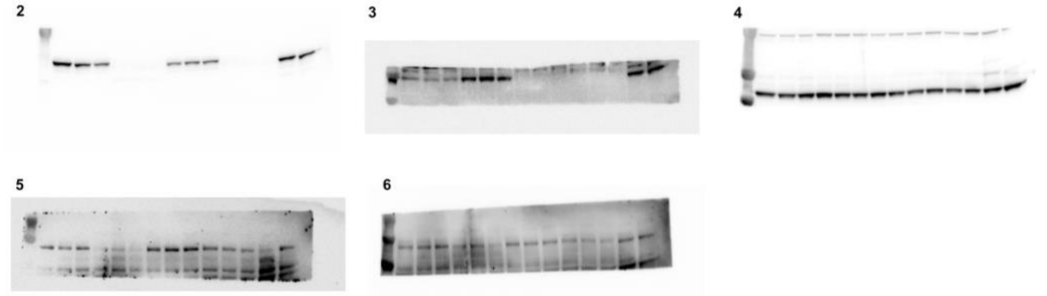

Supp. Fig. 6B:

The membrane was cut at 75 kDa and membrane 1 (75-250 kDa) was incubated with anti-Vinculin (1), while membrane 2 (10-75 kDa) was incubated with anti-PrP (POM2) (2).

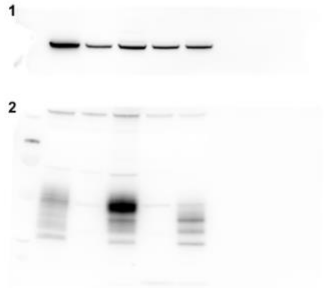

Supp. Fig. 6C:

The membrane 1-2 was cut at 75 kDa. Membrane 1 (75-250 kDa) was incubated with anti-Vinculin (1), while membrane 2 (10-75 kDa) was incubated with anti-PrP (POM2) (2). The membrane 3 was transferred with the same samples pre-treated with PK digestion. Membrane 3 was incubated with anti-PrP (POM1) (3).

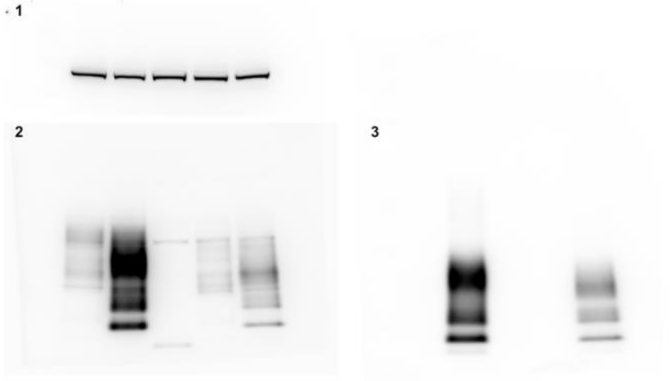

Supp. Fig. 7A:

The membrane was cut at 75 kDa (1 and 2). Membrane 1 (75-250 kDa) was incubated with anti-Vinculin (1). Membrane 2 (10-75 kDa) was incubated anti-PrP (POM2) (2). Membrane 2 was following cut at 45 kDa (3 and 5). Membrane 3 (45-75 kDa) was incubated in succession with both anti-Tfap2c (3), anti-hnRNP K (4) without stripping. Membrane 5 was stripped and then incubated with anti-Actin first (not shown in the main figures) and then with anti-mCherry (5).

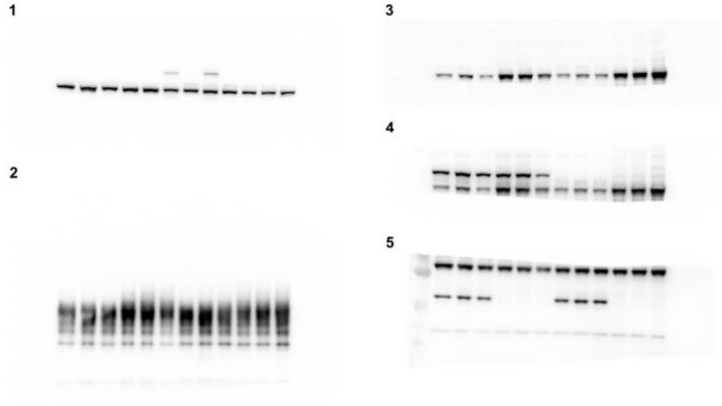

Supp. Fig. 7B:

The membrane was incubated with anti-pS6 (1). After stripping the membrane was incubated with anti-S6 (2).

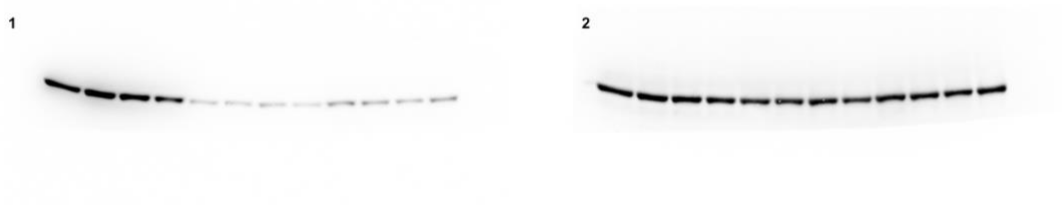

Gating strategy

Fig. 6A

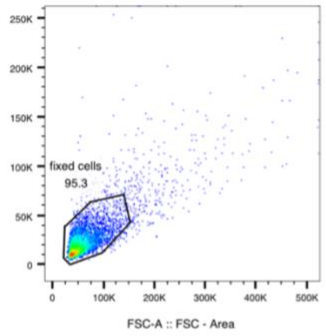

001 Unstained WLSM.fcs
Ungated
10137

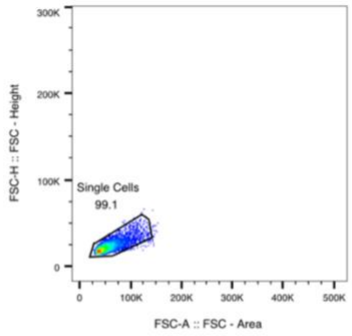

001 Unstained WLSM.fcs
fixed cells
9665

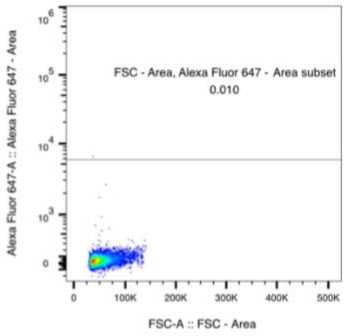

001 Unstained WLSM.fcs
Single Cells
9582

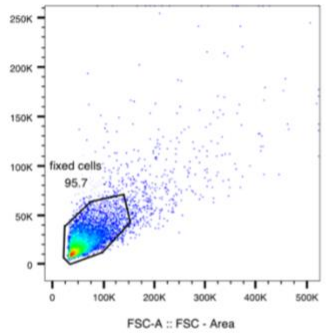

002 NBH WLSM.fcs
Ungated
15175

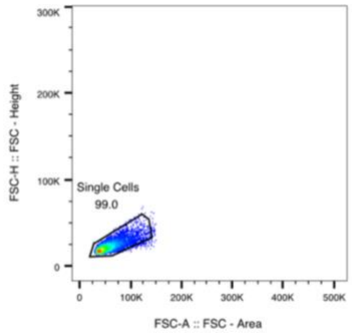

002 NBH WLSM.fcs
fixed cells
14521

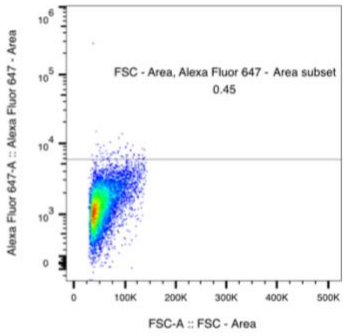

002 NBH WLSM.fcs
Single Cells
14373

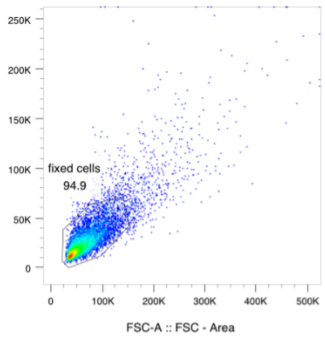

003 NTsi/TFAP2C_1 WLSM.fcs
Ungated
15207

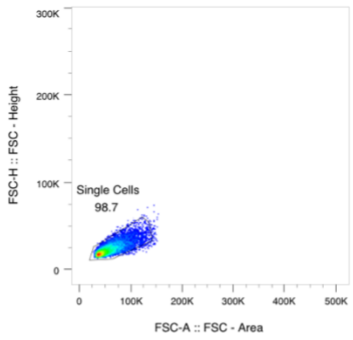

003 NTsi/TFAP2C_1 WLSM.fcs
fixed cells
14426

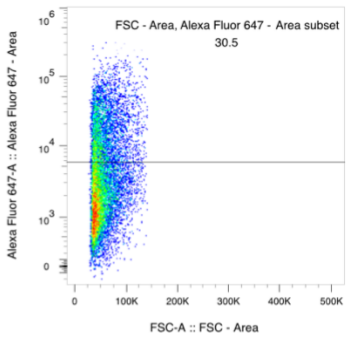

003 NTsi/TFAP2C_1 WLSM.fcs
Single Cells
14242

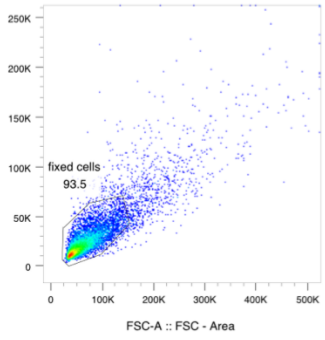

004 NTsi/TFAP2C_2 WLSM.fcs
Ungated
15282

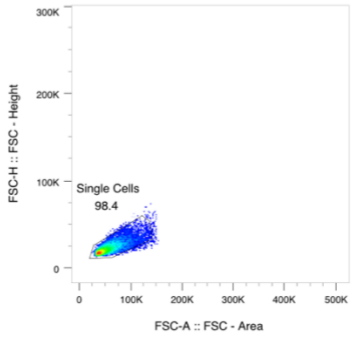

004 NTsi/TFAP2C_2 WLSM.fcs
fixed cells
14294

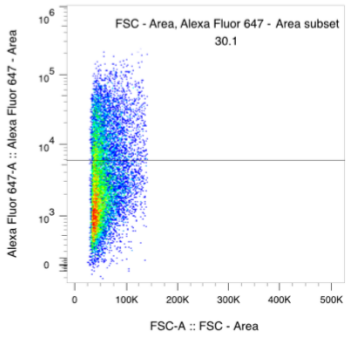

004 NTsi/TFAP2C_2 WLSM.fcs
Single Cells
14064

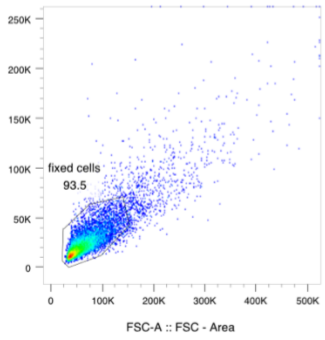

005 NTsi/TFAP2C_3 WLSM
Ungated
15255

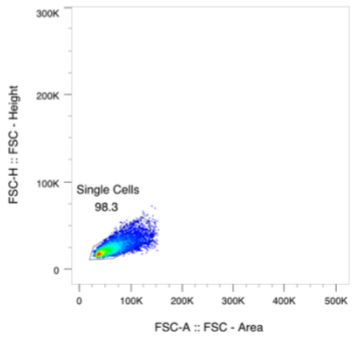

005 NT/TFAP2C_3 WLSM.f
fixed cells
14264

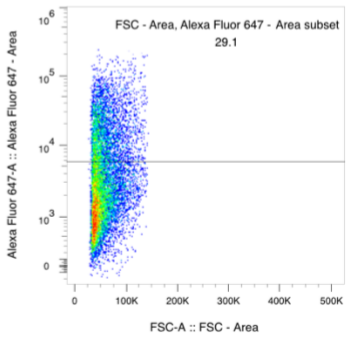

005 NT/TFAP2C_3 WLSM.f
Single Cells
14016

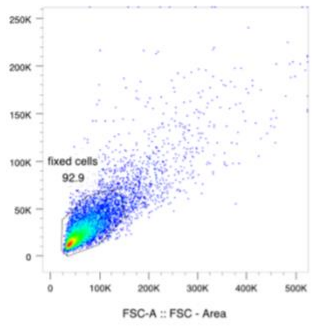

006 HNRNPKsi/TFAP2C_1 WLSM.fcs
Ungated
15286

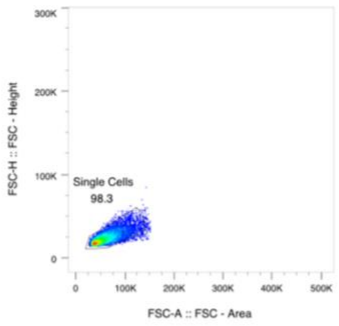

006 HNRNPKsi/TFAP2C_1 WLSM.fcs
fixed cells
14208

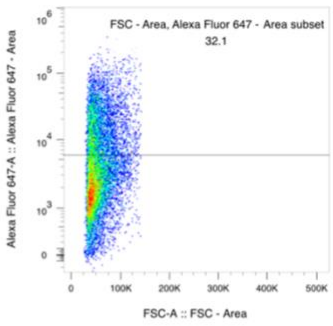

006 HNRNPKsi/TFAP2C_1 WLSM.fcs
Single Cells
13961

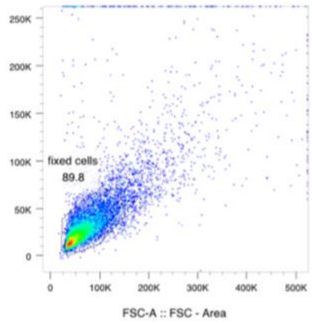

007 HNRNPKsi/TFAP2C_2 WLSM.fcs
Ungated
15633

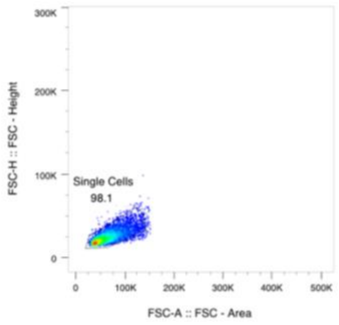

007 HNRNPKsi/TFAP2C_2 WLSM.fcs
fixed cells
14046

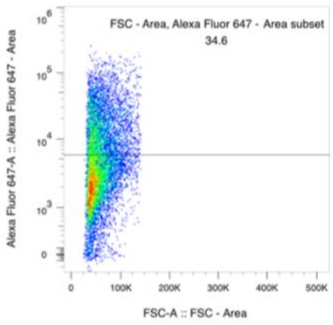

007 HNRNPKsi/TFAP2C_2 WLSM.fcs
Single Cells
13780

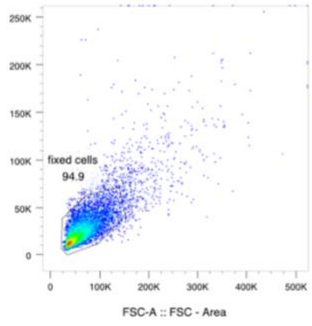

008 HNRNPKsi/TFAP2C_3 WLSM.fcs
Ungated
15192

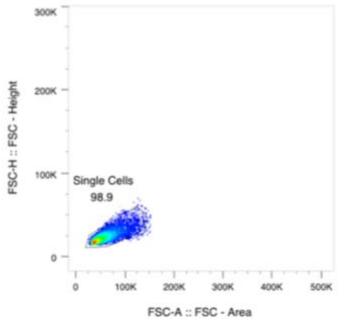

008 HNRNPKsi/TFAP2C_3 WLSM.fcs
fixed cells
14423

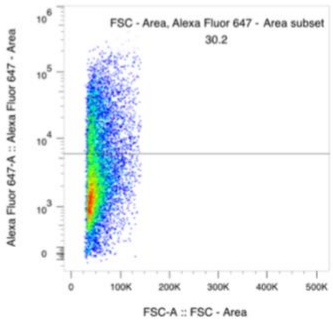

008 HNRNPKsi/TFAP2C_3 WLSM.fcs
Single Cells
14264

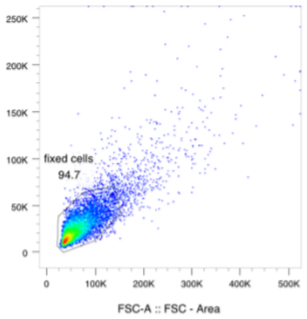

009 NTsi/mCherry_1 WLSM.fcs
Ungated
15198

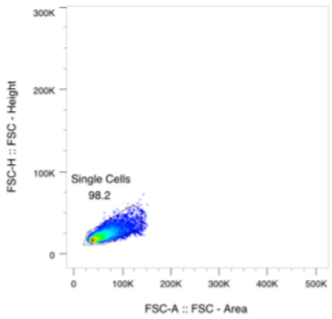

009 NTsi/mCherry_1 WLSM.fcs
fixed cells
14387

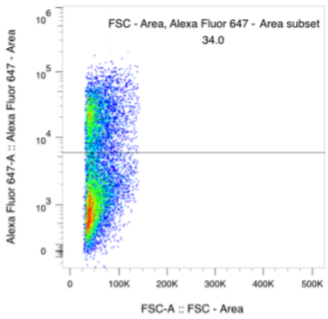

009 NTsi/mCherry_1 WLSM.fcs
Single Cells
14121

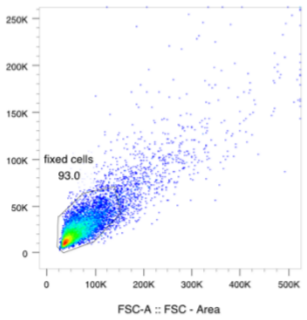

010 NTsi/mCherry_2 WLSM.fcs
Ungated
15309

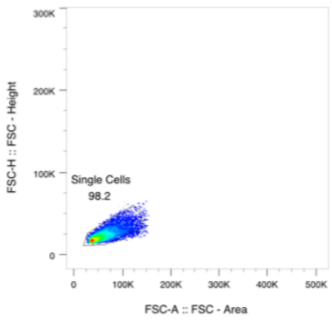

010 NTsi/mCherry_2 WLSM.fcs
fixed cells
14236

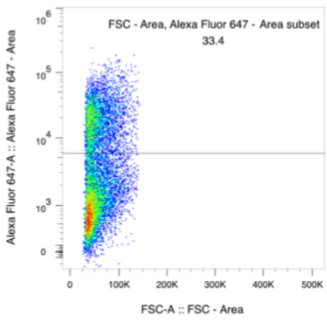

010 NTsi/mCherry_2 WLSM.fcs
Single Cells
13983

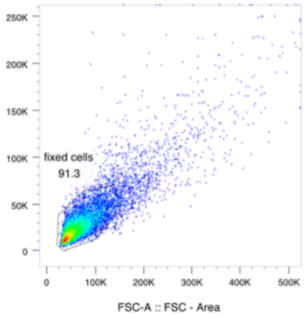

014 NTsi/mCherry_3 WLSM.fcs
Ungated
15379

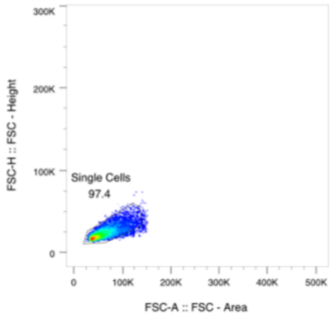

014 NTsi/mCherry_3 WLSM.fcs
fixed cells
14038

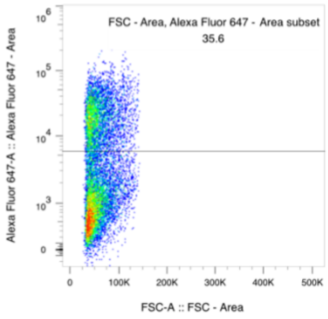

014 NTsi/mCherry_3 WLSM.fcs
Single Cells
13680

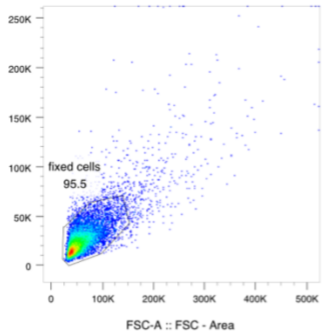

011 HNRNPKsi/mCherry_1 WLSM.fcs
Ungated
15178

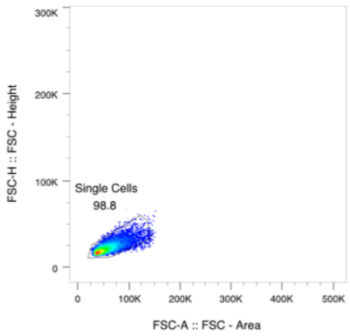

011 HNRNPKsi/mCherry_1 WLSM.fcs
fixed cells
14494

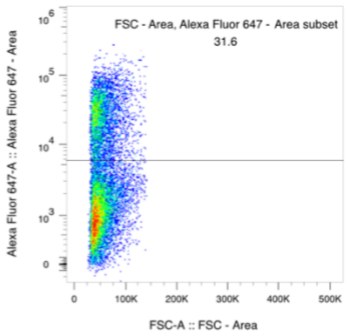

011 HNRNPKsi/mCherry_1 WLSM.fcs
Single Cells
14315

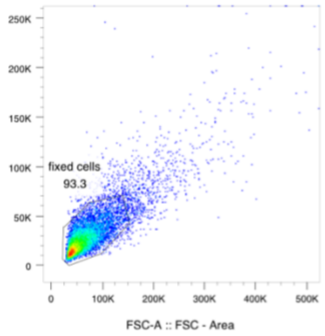

012 HNRNPKsi/mCherry_2 WLSM.fcs
Ungated
15226

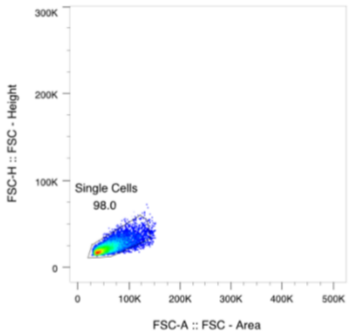

012 HNRNPKsi/mCherry_2 WLSM.fcs
fixed cells
14199

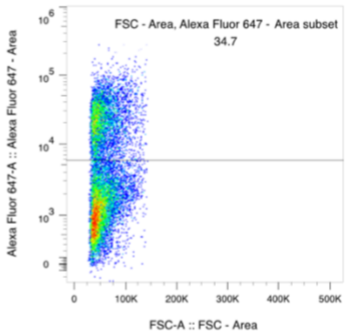

012 HNRNPKsi/mCherry_2 WLSM.fcs
Single Cells
13919

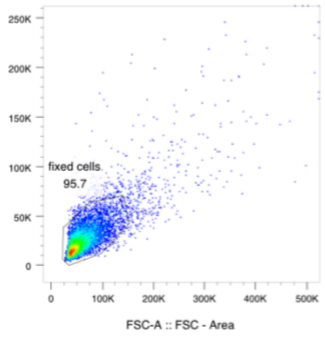

013 HNRNPKsi/mCherry_3 WLSM.fcs
Ungated
15150

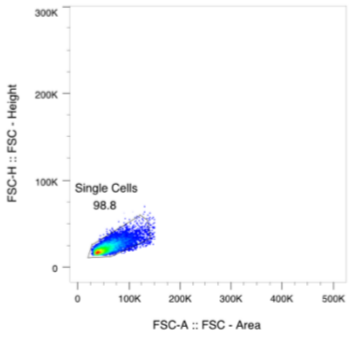

013 HNRNPKsi/mCherry_3 WLSM.fcs
fixed cells
14506

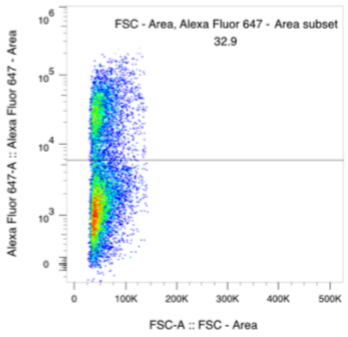

013 HNRNPKsi/mCherry_3 WLSM.fcs
Single Cells
14326

Supplementary Fig.1B

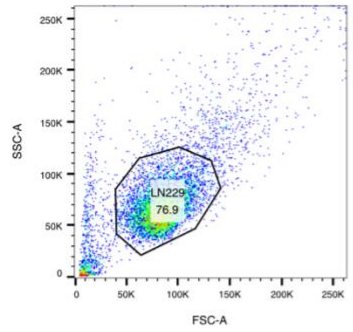

-_Negative CTRL_001.fcs
Ungated
10000

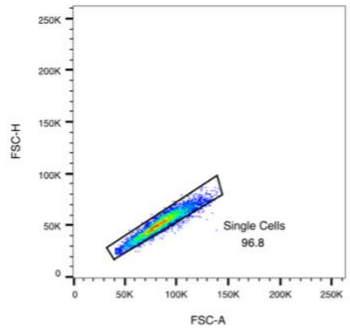

-_Negative CTRL_001.fcs
LN229
7691

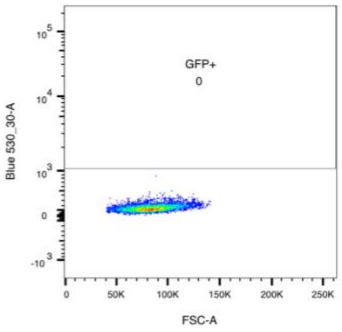

-_Negative CTRL_001.fcs
Single Cells
7444

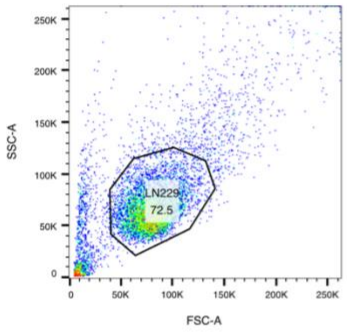

-_Positive_CTRL_2_005.fcs
Ungated
10000

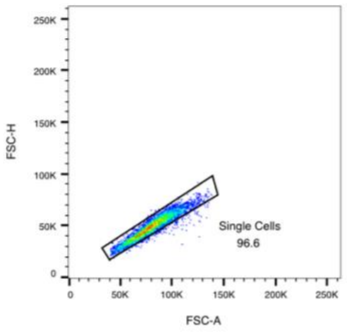

-_Positive_CTRL_2_005.fcs
LN229
7255

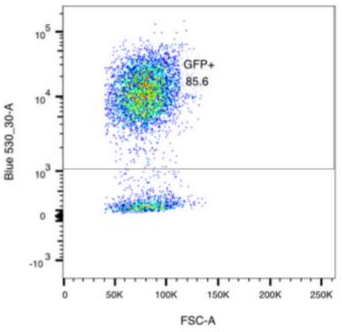

-_Positive_CTRL_2_005.fcs
Single Cells
7011

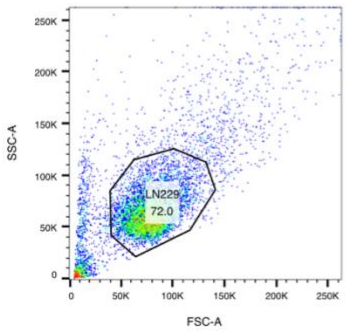

-_Positive_CTRL_002.fcs
Ungated
10000

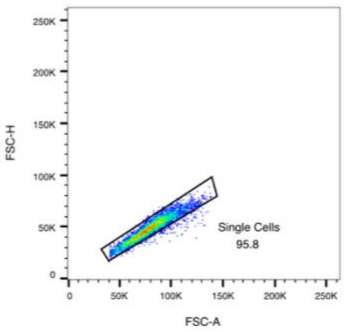

-_Positive_CTRL_002.fcs
LN229
7202

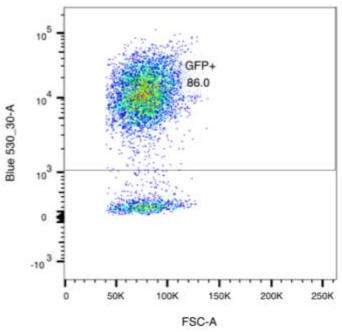

-_Positive_CTRL_002.fcs
Single Cells
6901

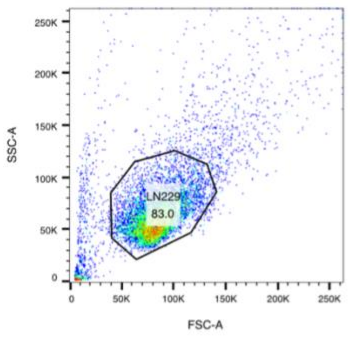

-_A9_2_017.fcs
Ungated
10000

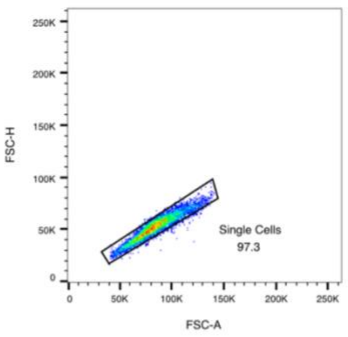

-_A9_2_017.fcs
LN229
8303

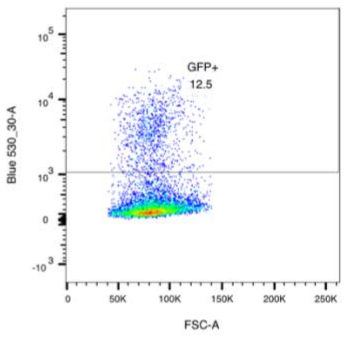

-_A9_2_017.fcs
Single Cells
8080

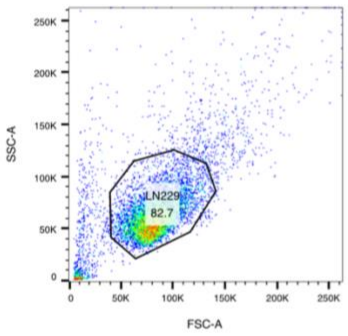

-_A9_016.fcs
Ungated
10000

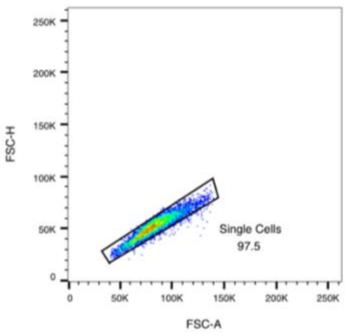

-_A9_016.fcs
LN229
8274

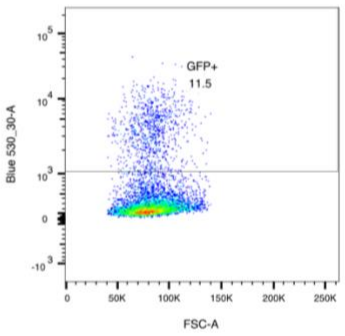

-_A9_016.fcs
Single Cells
8069

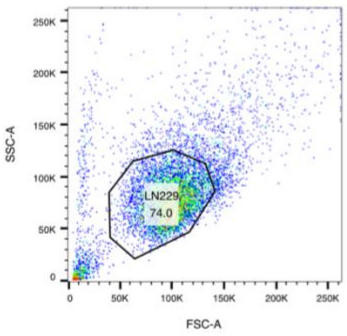

-_A10_2_007.fcs
Ungated
10000

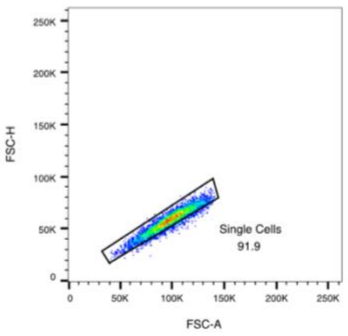

-_A10_2_007.fcs
LN229
7395

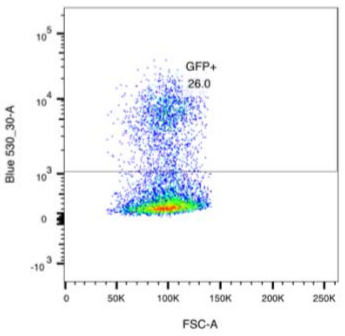

-_A10_2_007.fcs
Single Cells
6799

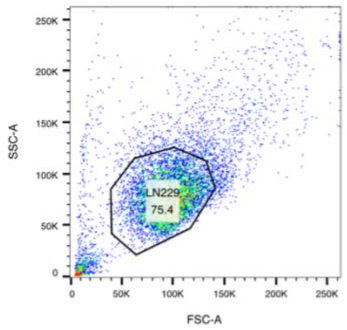

-_A10_006.fcs
Ungated
10000

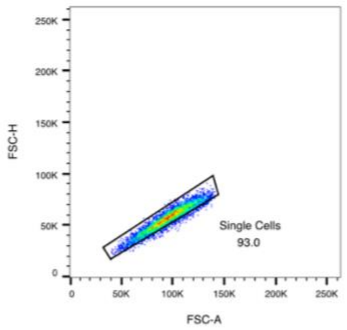

-_A10_006.fcs
LN229
7544

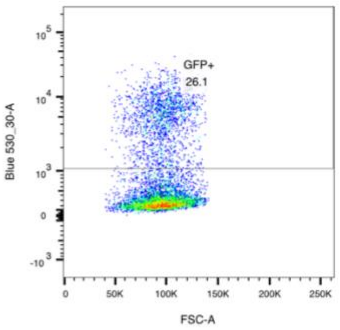

-_A10_006.fcs
Single Cells
7014

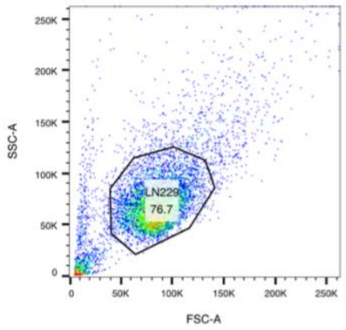

-_Polyclonal Cas9+_2_019.fcs
Ungated
10000

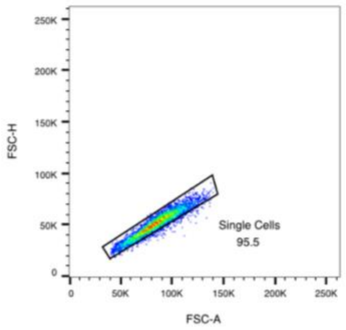

-_Polyclonal Cas9+_2_019.fcs
LN229
7674

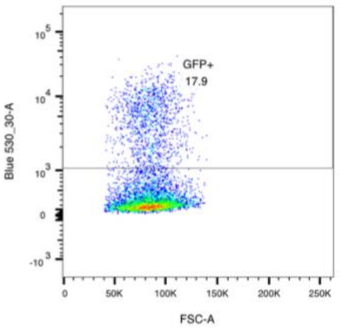

-_Polyclonal Cas9+_2_019.fcs
Single Cells
7329

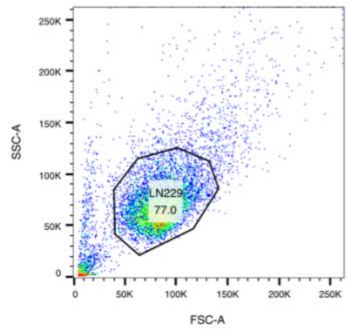

-_Polyclonal Cas9+_018.fcs
Ungated
10000

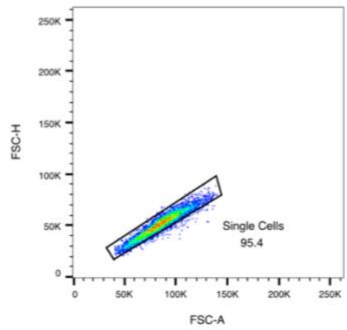

-_Polyclonal Cas9+_018.fcs
LN229
7696

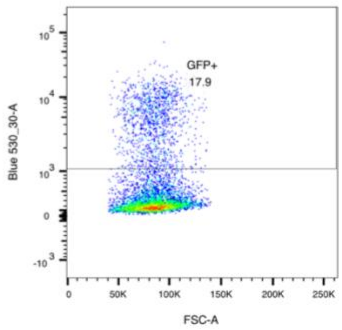

-_Polyclonal Cas9+_018.fcs
Single Cells
7342

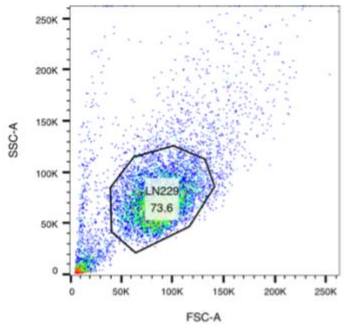

-_G11_2_013.fcs
Ungated
10000

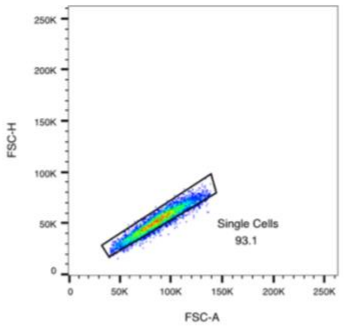

-_G11_2_013.fcs
LN229
7363

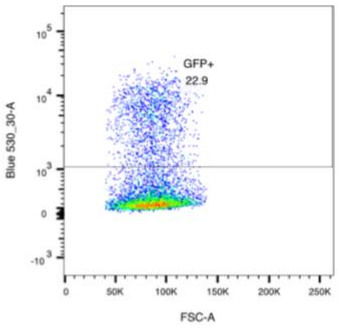

-_G11_2_013.fcs
Single Cells
6856

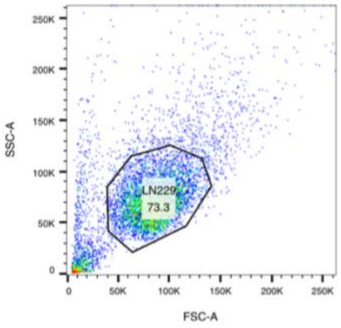

-_G11_012.fcs
Ungated
10000

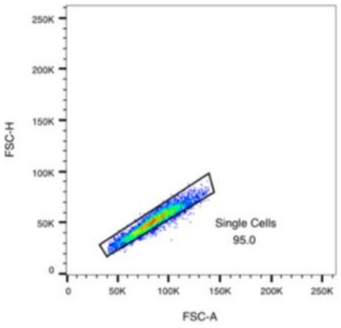

-_G11_012.fcs
LN229
7328

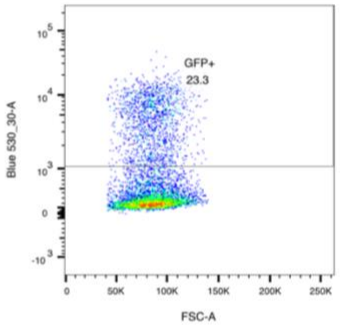

-_G11_012.fcs
Single Cells
6964

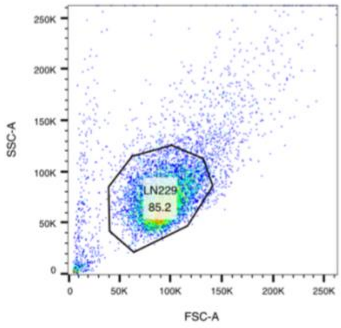

-_D7_2_004.fcs
Ungated
10000

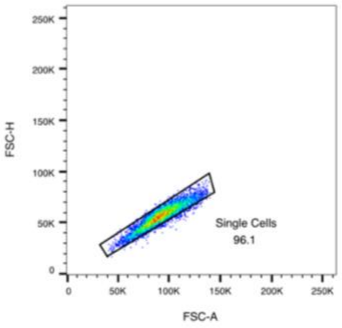

-_D7_2_004.fcs
LN229
8516

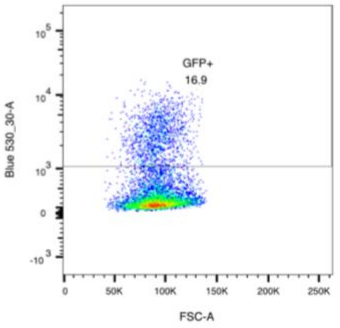

-_D7_2_004.fcs
Single Cells
8183

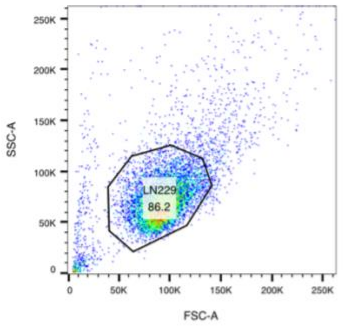

-_D7_003.fcs
Ungated
10000

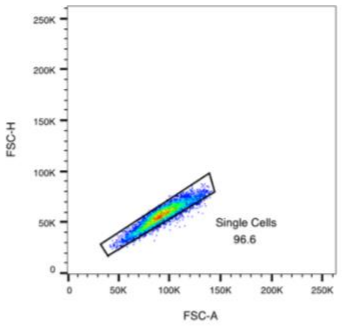

-_D7_003.fcs
LN229
8618

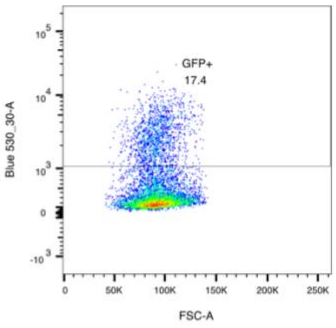

-_D7_003.fcs
Single Cells
8323

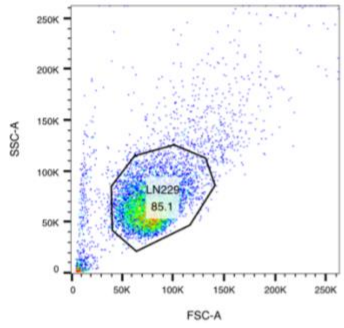

-_E2_2_009.fcs
Ungated
10000

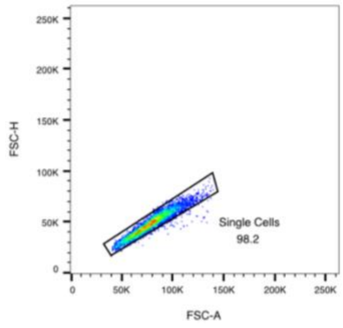

-_E2_2_009.fcs
LN229
8509

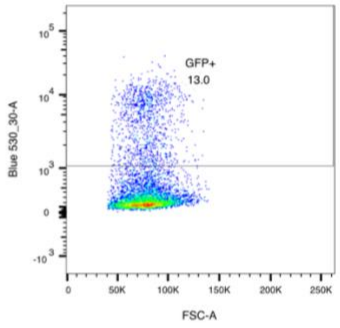

-_E2_2_009.fcs
Single Cells
8354

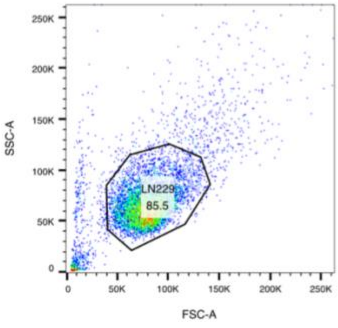

-_E2_008.fcs
Ungated
10000

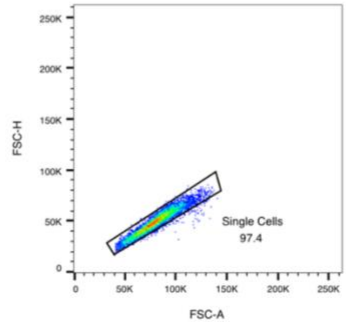

-_E2_008.fcs
LN229
8546

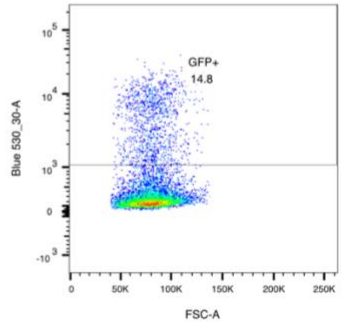

-_E2_008.fcs
Single Cells
8327

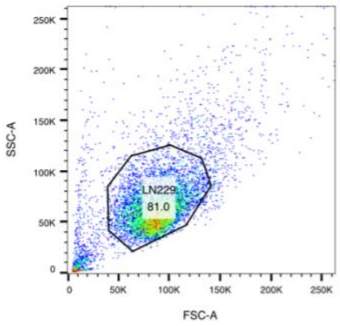

-_C3_2_015.fcs
Ungated
10000

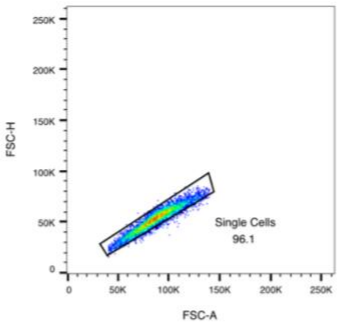

-_C3_2_015.fcs
LN229
8096

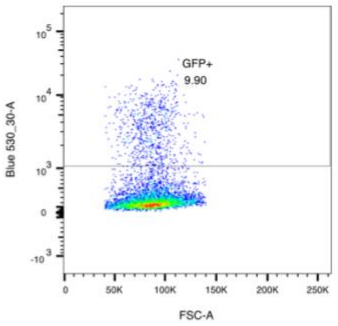

-_C3_2_015.fcs
Single Cells
7777

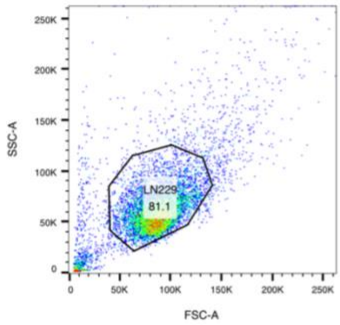

-_C3_014.fcs
Ungated
10000

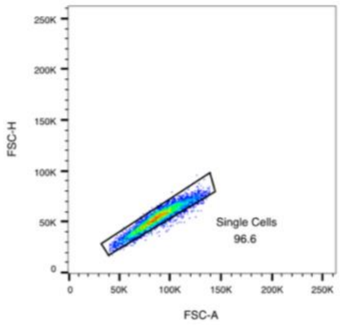

-_C3_014.fcs
LN229
8110

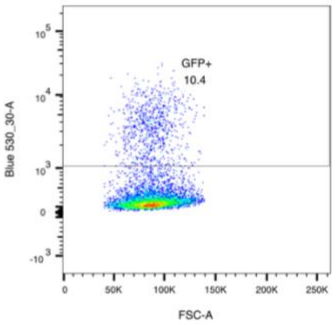

-_C3_014.fcs
Single Cells
7835

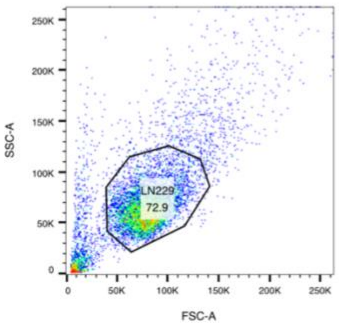

-_M3_2_011.fcs
Ungated
10000

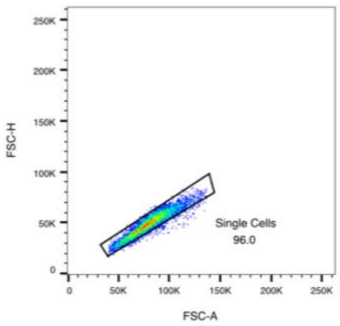

-_M3_2_011.fcs
LN229
7292

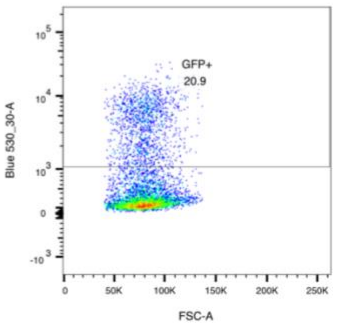

-_M3_2_011.fcs
Single Cells
6997

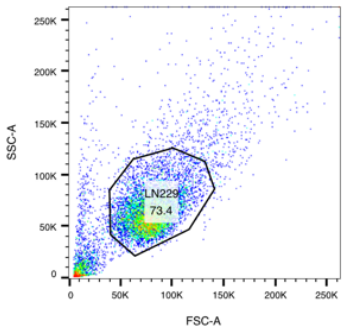

-_M3_010.fcs
Ungated
10000

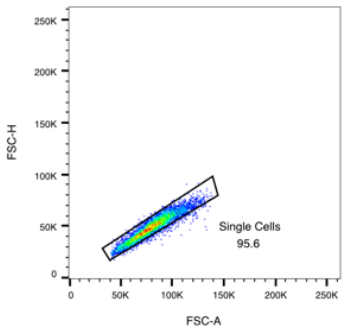

-_M3_010.fcs
LN229
7340

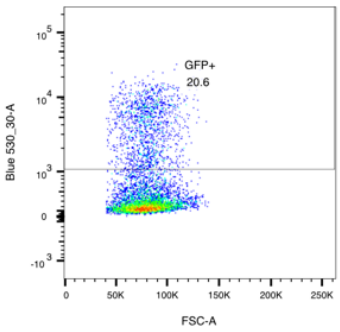

-_M3_010.fcs
Single Cells
7019

Supplementary Fig.4C

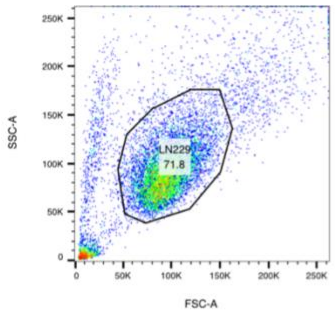

Specimen_001_NT3/NT 1_009.fcs
Ungated
13912

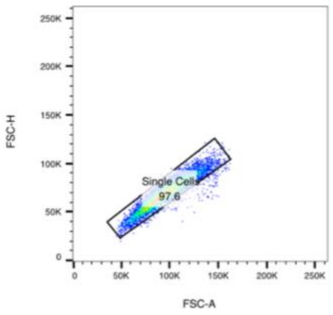

Specimen_001_NT3/NT 1_009.fcs
C3 cells
9982

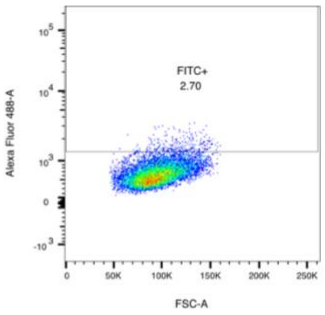

Specimen_001_NT3/NT 1_009.fcs
Single Cells
9740

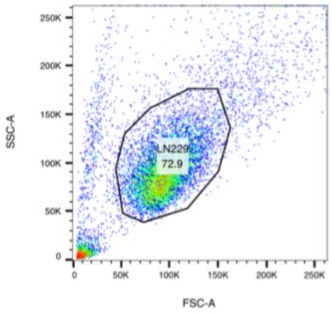

Specimen_001_NT3/NT 2_010.fcs
Ungated
13693

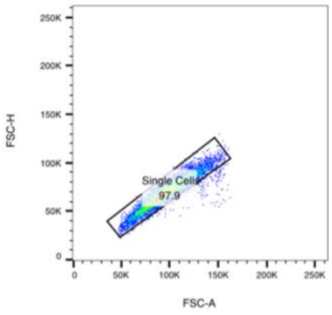

Specimen_001_NT3/NT 2_010.fcs
C3 cells
9982

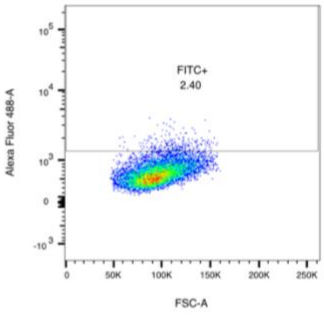

Specimen_001_NT3/NT 2_010.fcs
Single Cells
9770

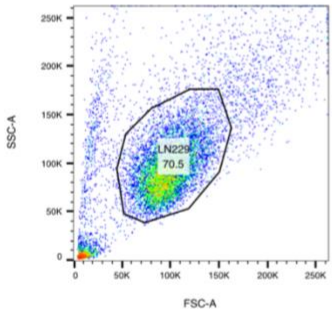

Specimen_001_NT3/NT 3_011.fcs
Ungated
14131

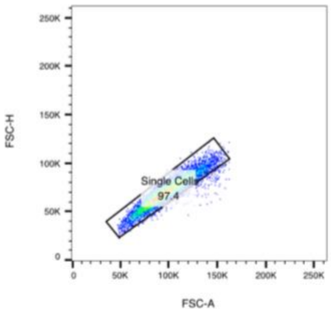

Specimen_001_NT3/NT 3_011.fcs
C3 cells
9958

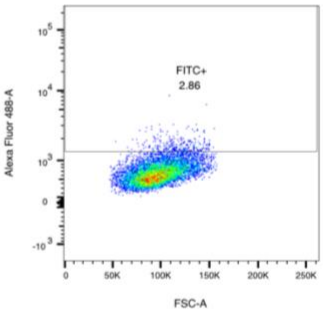

Specimen_001_NT3/NT 3_011.fcs
Single Cells
9696

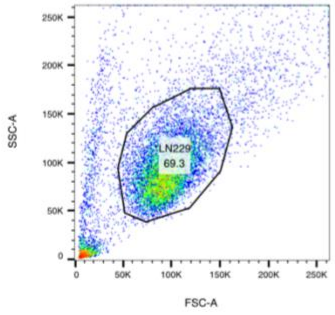

Specimen_001_NT3/NT 4_012.fcs
Ungated
14430

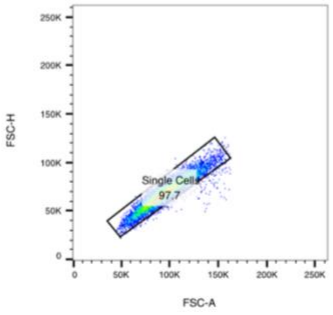

Specimen_001_NT3/NT 4_012.fcs
C3 cells
9999

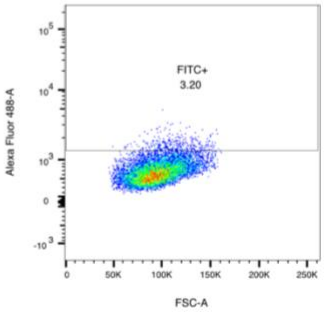

Specimen_001_NT3/NT 4_012.fcs
Single Cells
9771

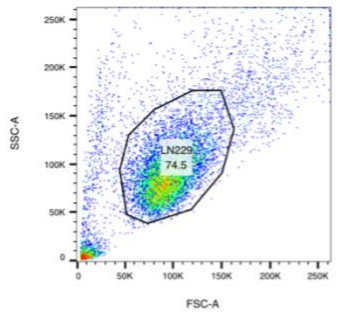

Specimen_001_NT NT 5_013.fcs
Ungated
13359

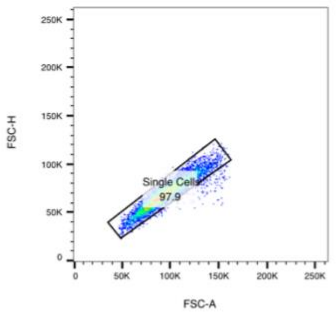

Specimen_001_NT NT 5_013.fcs
C3 cells
9950

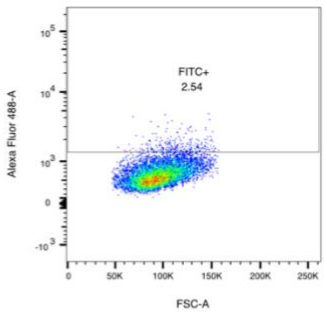

Specimen_001_NT NT 5_013.fcs
Single Cells
9746

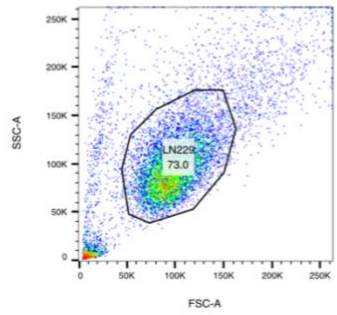

Specimen_001_NT3/NT 6_014.fcs
Ungated
13657

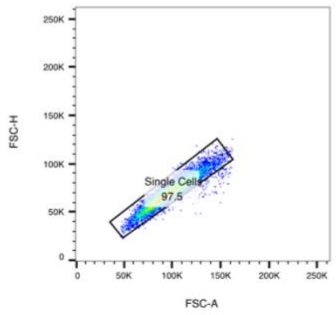

Specimen_001_NT3/NT 6_014.fcs
C3 cells
9971

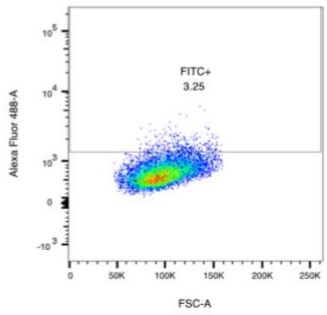

Specimen_001_NT3/NT 6_014.fcs
Single Cells
9726

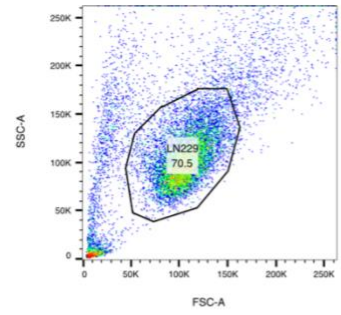

Specimen_001_NT3/HNRNPK 1_015.fcs
Ungated
14287

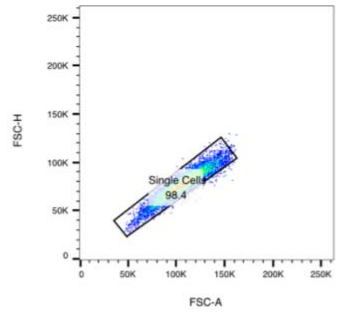

Specimen_001_NT3/HNRNPK 1_015.fcs
C3 cells
10075

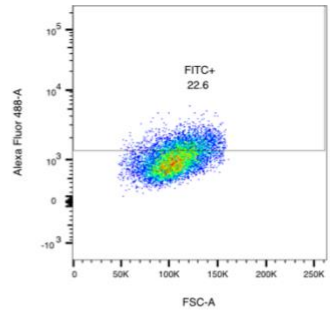

Specimen_001_NT3/HNRNPK 1_015.fcs
Single Cells
9918

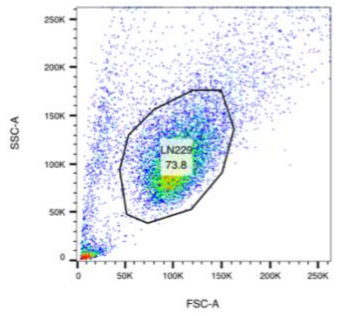

Specimen_001_NT3/HNRNPK 2_016.fcs
Ungated
13626

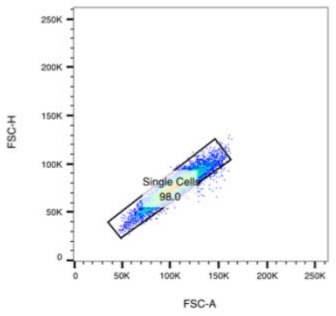

Specimen_001_NT3/HNRNPK 2_016.fcs
C3 cells
10051

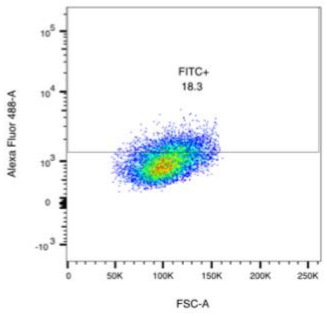

Specimen_001_NT3/HNRNPK 2_016.fcs
Single Cells
9848

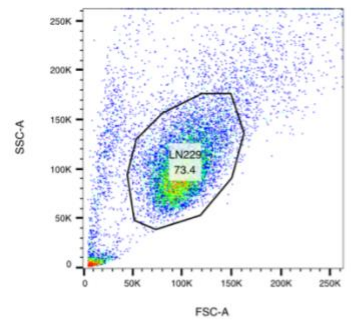

Specimen_001_NT3/HNRNPK 3_017.fcs
Ungated
13724

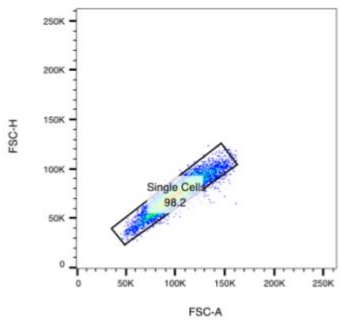

Specimen_001_NT3/HNRNPK 3_017.fcs
C3 cells
10080

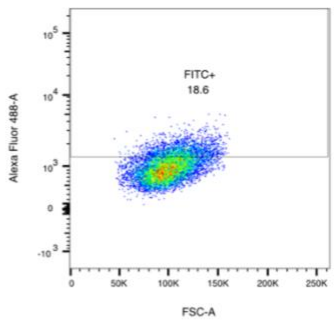

Specimen_001_NT3/HNRNPK 3_017.fcs
Single Cells
9899

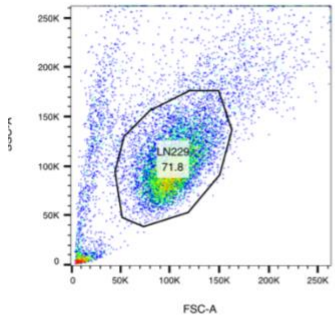

Specimen_001_NT3/HNRNPK 4_018.fcs
Ungated
13997

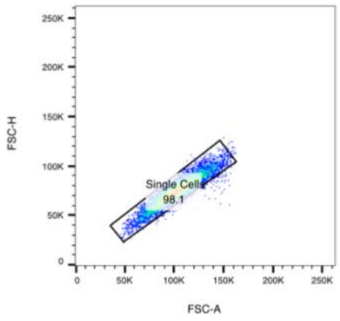

Specimen_001_NT3/HNRNPK 4_018.fcs
C3 cells
10054

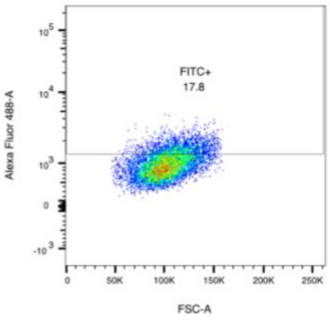

Specimen_001_NT3/HNRNPK 4_018.fcs
Single Cells
9862

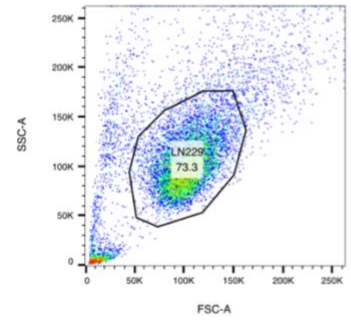

Specimen_001_NT3/HNRNPK 5_019.fcs
Ungated
13721

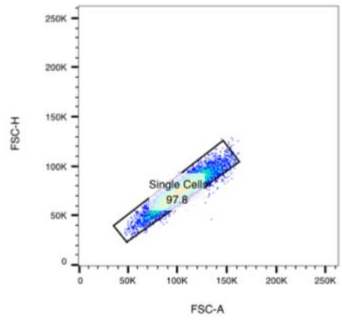

Specimen_001_NT3/HNRNPK 5_019.fcs
C3 cells
10058

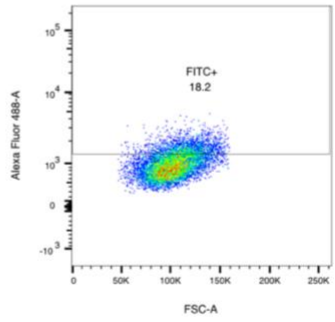

Specimen_001_NT3/HNRNPK 5_019.fcs
Single Cells
9838

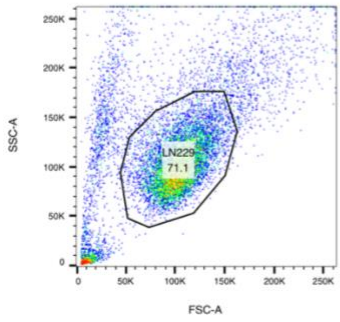

Specimen_001_NT3/HNRNPK 6_020.fcs
Ungated
14159

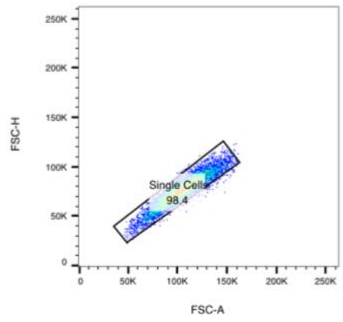

Specimen_001_NT3/HNRNPK 6_020.fcs
C3 cells
10060

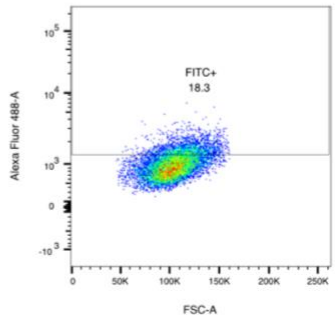

Specimen_001_NT3/HNRNPK 6_020.fcs
Single Cells
9901

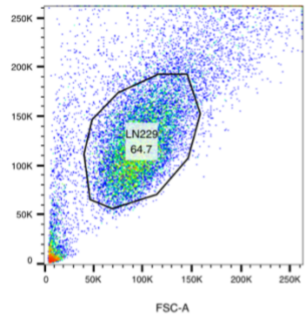

Specimen_001_TFAP2C/NT 1_021.fcs
Ungated
17078

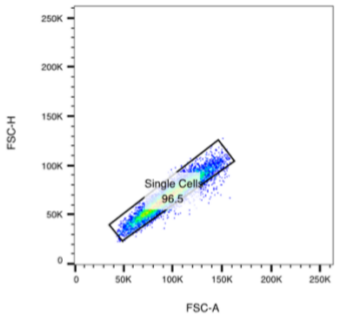

Specimen_001_TFAP2C/NT 1_021.fcs
C3 cells
11046

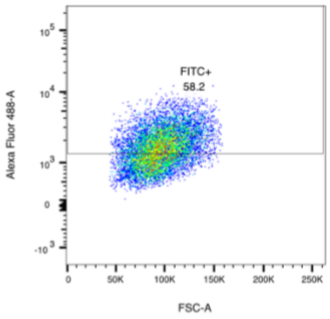

Specimen_001_TFAP2C/NT 1_021.fcs
Single Cells
10656

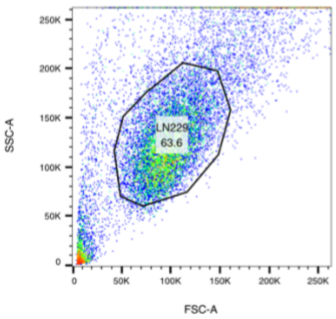

Specimen_001_TFAP2C/NT 2_022.fcs
Ungated
16297

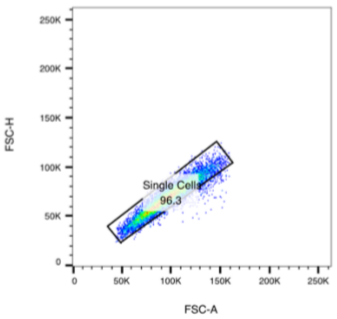

Specimen_001_TFAP2C/NT 2_022.fcs
C3 cells
10372

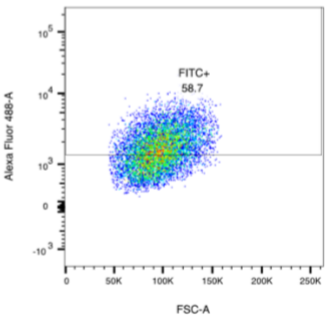

Specimen_001_TFAP2C/NT 2_022.fcs
Single Cells
9988

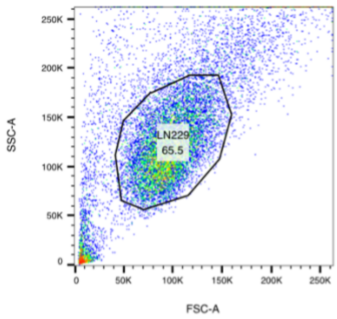

Specimen_001_TFAP2C/NT 3_023.fcs
Ungated
15523

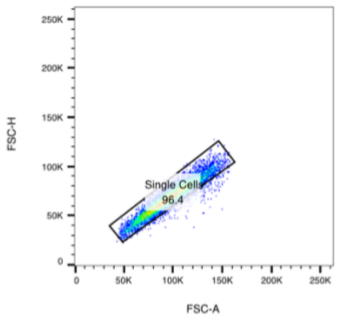

Specimen_001_TFAP2C/NT 3_023.fcs
C3 cells
10174

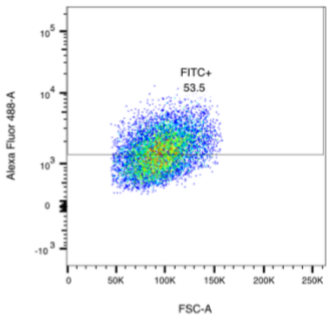

Specimen_001_TFAP2C/NT 3_023.fcs
Single Cells
9810

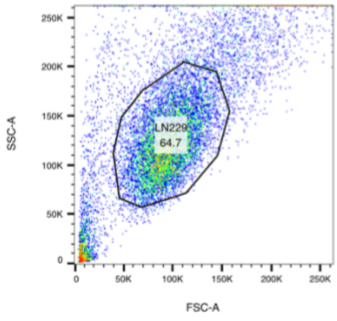

Specimen_001_TFAP2C/NT 4_024.fcs
Ungated
16071

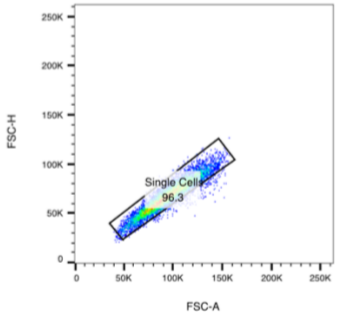

Specimen_001_TFAP2C/NT 4_024.fcs
C3 cells
10390

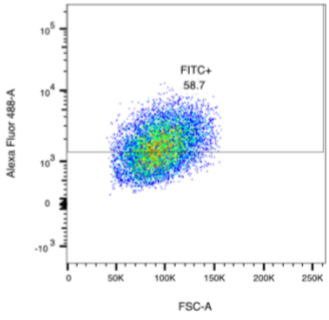

Specimen_001_TFAP2C/NT 4_024.fcs
Single Cells
10009

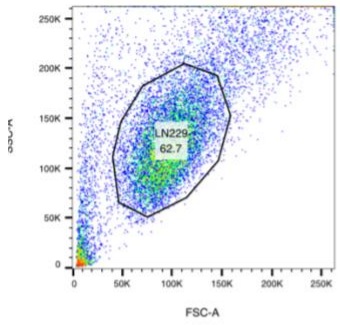

Specimen_001_TFAP2C/NT 5_025.fcs
Ungated
16670

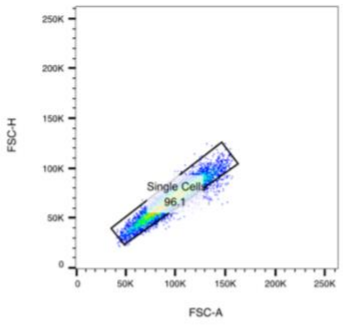

Specimen_001_TFAP2C/NT 5_025.fcs
C3 cells
10456

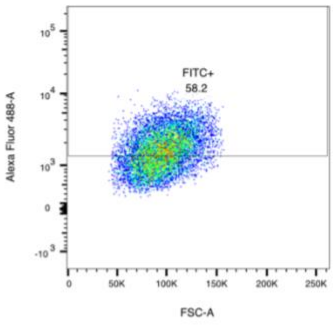

Specimen_001_TFAP2C/NT 5_025.fcs
Single Cells
10046

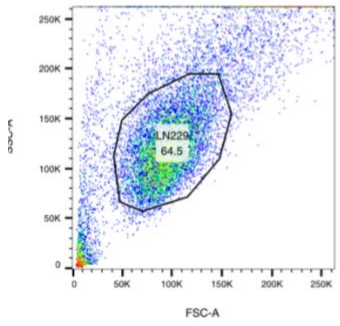

Specimen_001_TFAP2C/NT 6_026.fcs
Ungated
15792

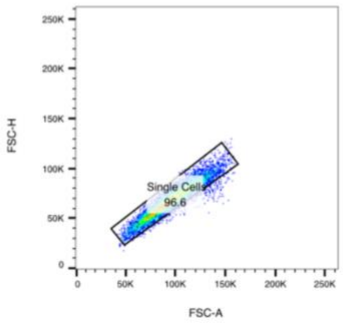

Specimen_001_TFAP2C/NT 6_026.fcs
C3 cells
10189

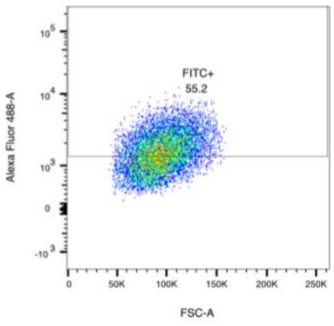

Specimen_001_TFAP2C/NT 6_026.fcs
Single Cells
9838

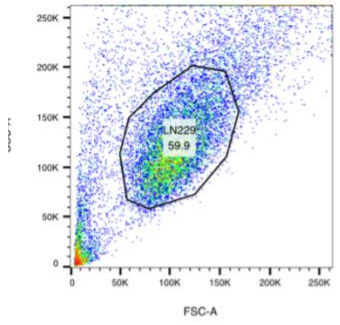

Specimen_001_TFAP2C/HNRNPK 1_027.fcs
Ungated
17072

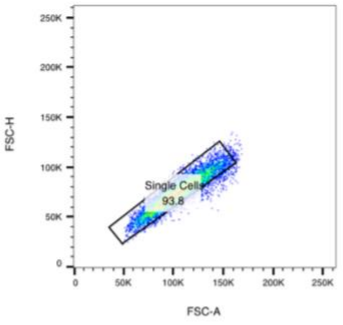

Specimen_001_TFAP2C/HNRNPK 1_027.fcs
C3 cells
10231

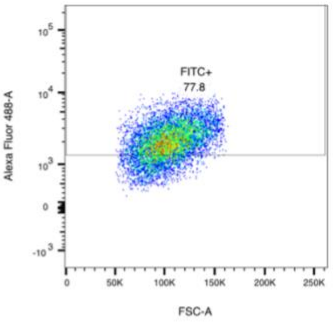

Specimen_001_TFAP2C/HNRNPK 1_027.fcs
Single Cells
9592

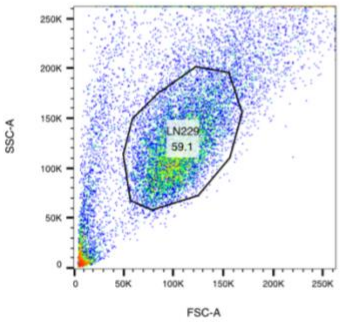

Specimen_001_TFAP2C/HNRNPK 2_028.fcs
Ungated
17346

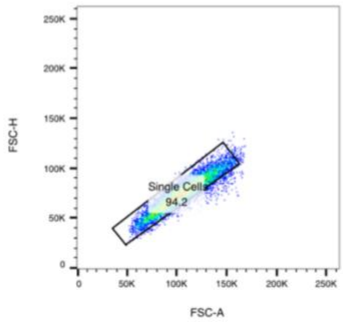

Specimen_001_TFAP2C/HNRNPK 2_028.fcs
C3 cells
10249

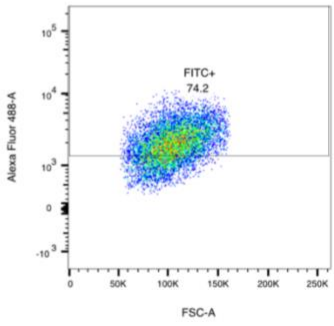

Specimen_001_TFAP2C/HNRNPK 2_028.fcs
Single Cells
9654

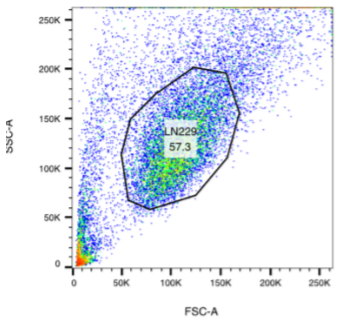

Specimen_001_TFAP2C/HNRNPK 3_029.fcs
Ungated
17883

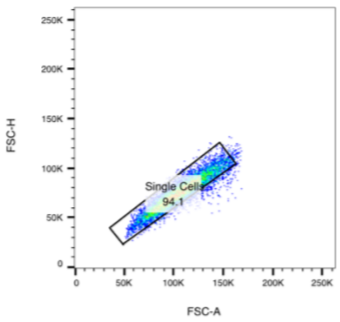

Specimen_001_TFAP2C/HNRNPK 3_029.fcs
C3 cells
10254

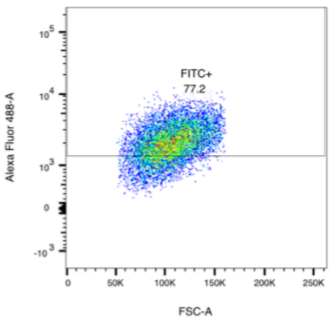

Specimen_001_TFAP2C/HNRNPK 3_029.fcs
Single Cells
9646

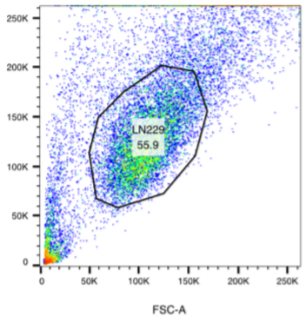

Specimen_001_TFAP2C/HNRNPK 4_030.fcs
Ungated
18474

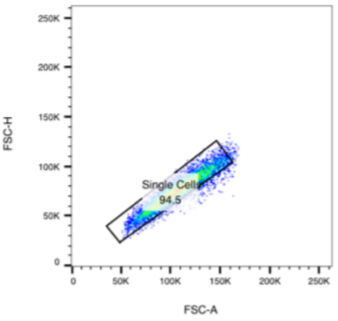

Specimen_001_TFAP2C/HNRNPK 4_030.fcs
C3 cells
10329

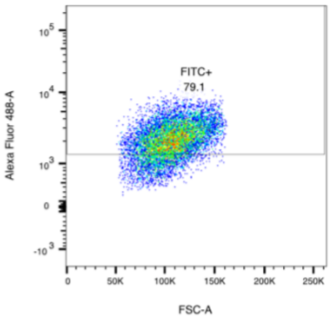

Specimen_001_TFAP2C/HNRNPK 4_030.fcs
Single Cells
9757

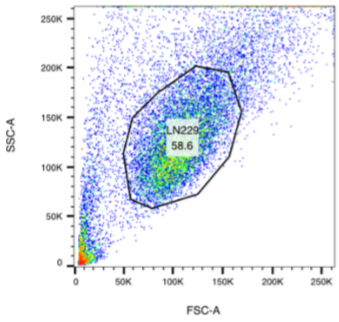

Specimen_001_TFAP2C/HNRNPK 5_031.fcs
Ungated
17627

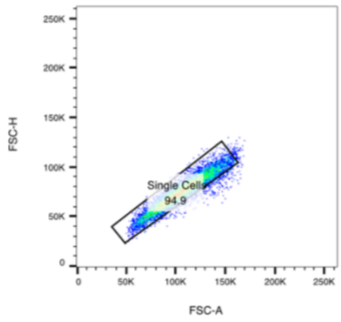

Specimen_001_TFAP2C/HNRNPK 5_031.fcs
C3 cells
10327

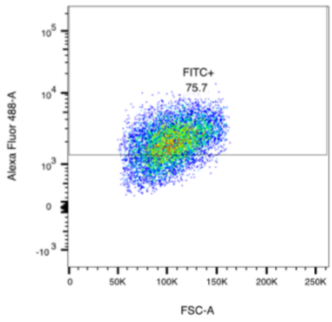

Specimen_001_TFAP2C/HNRNPK 5_031.fcs
Single Cells
9797

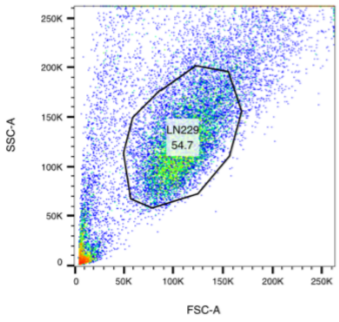

Specimen_001_TFAP2C/HNRNPK 6_032.fcs
Ungated
18928

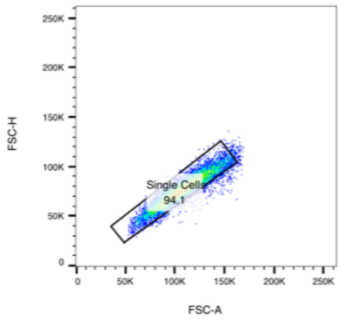

Specimen_001_TFAP2C/HNRNPK 6_032.fcs
C3 cells
10362

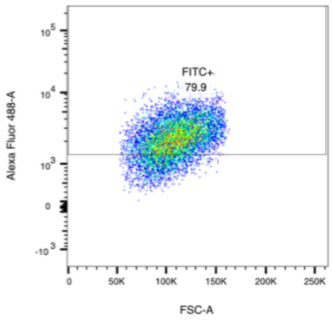

Specimen_001_TFAP2C/HNRNPK 6_032.fcs
Single Cells
9748

Supplementary Fig.6E

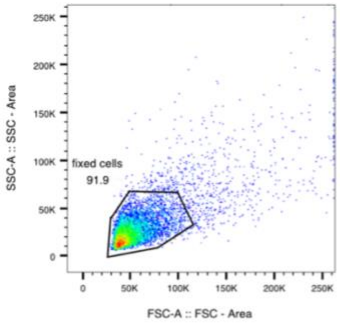

009 HovL unstained WLSM.fcs
Ungated
10000

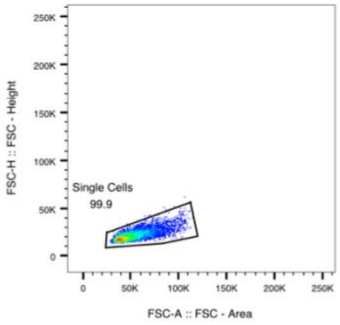

009 HovL unstained WLSM.fcs
fixed cells
9192

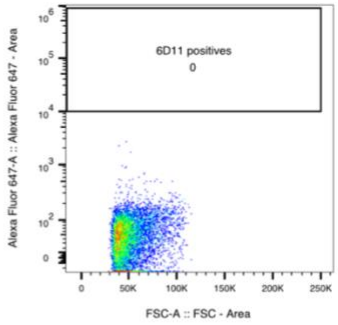

009 HovL unstained WLSM.fcs
Single Cells
9183

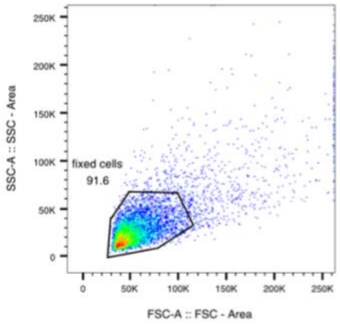

008 HovL NBH WLSM.fcs
Ungated
10000

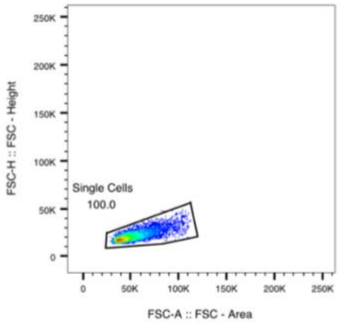

008 HovL NBH WLSM.fcs
fixed cells
9165

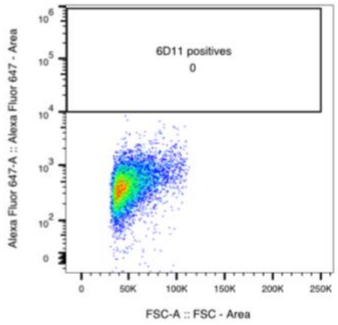

008 HovL NBH WLSM.fcs
Single Cells
9162

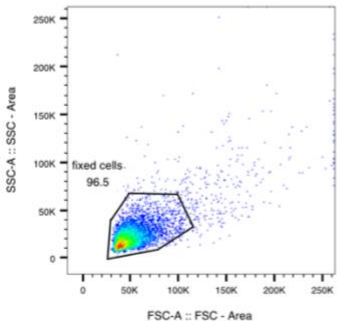

007 HovL PG127 WLSM.fcs
Ungated
10000

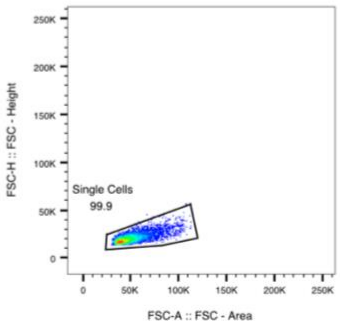

007 HovL PG127 WLSM.fcs
fixed cells
9648

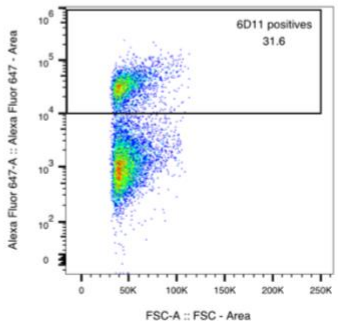

007 HovL PG127 WLSM.fcs
Single Cells
9643